Measurement of the Top Quark p_T Distribution

by

Andrew Robinson

A thesis submitted in conformity with the requirements
for the degree of Doctor of Philosophy
Graduate Department of Physics
University of Toronto

Copyright © 2000 by Andrew Robinson

Abstract

Measurement of the Top Quark p_T Distribution

Andrew Robinson

Doctor of Philosophy

Graduate Department of Physics

University of Toronto

2000

We have measured the p_T distribution of top quarks that are pair produced in $p\bar{p}$ collisions at $\sqrt{s} = 1.8$ TeV using a sample of $t\bar{t}$ decays in which we observe a single high-p_T charged lepton, a neutrino and four or more jets. We use a likelihood technique that corrects for the experimental bias introduced due to event reconstruction and detector resolution effects. The observed distribution is in agreement with the Standard Model prediction. We use these data to place limits on the production of high-p_T top quarks suggested in some models of anomalous top quark pair production.

Contents

1 The Top Quark **1**

1.1 The Standard Model 4

1.1.1 Limitations of the Standard Model 6

1.1.2 Possible Solutions 8

1.2 Top Quark Production 9

1.2.1 Hadroproduction of $t\bar{t}$ Pairs 9

1.2.2 Anomalous Top Quark Production 11

1.3 Overview of Dissertation 15

2 Experimental Apparatus **17**

2.1 The Fermilab Tevatron Collider 17

2.2 Overview of the CDF Detector 20

2.3 Calorimetry 22

2.3.1 Central Calorimeters 22

2.3.2 Plug and Forward Calorimeters 25

2.4 Tracking Systems 26

2.4.1 The Silicon Vertex Detector 27

2.4.2 The Vertex Time Projection Chamber 29

2.4.3 The Central Tracking Chamber 30

2.5 The Muon Chambers 32

2.6 The Beam Beam Counters 35

2.7 Trigger Systems 36

2.8 Offline Reconstruction 38

3 Event Selection **39**

3.1 Inclusive Electron Sample 40

3.1.1 Inclusive Muon Sample 42

3.1.2 W Sample 44

3.1.3 Kinematic Selection Criteria 46

3.2 Monte Carlo Simulation of Physics Processes 47

3.2.1 Simulation of Signal Events 47

3.2.2 Simulation of Background Events 48

3.3 B Hadron Identification 50

3.3.1 The SVX Algorithm 52

3.3.2 The SLT Algorithm 55

4 Reconstruction of $t\bar{t}$ candidates **57**

4.1 Jet Energy Corrections 58

4.1.1 Flavor Independent Jet Corrections 58

4.1.2 Flavor-Specific Corrections 61

4.2 The Kinematic Fit 63

4.3 Kinematic Resolution and Parton Assignments 68

4.4 Parameterizing the resolution 70

5 Measuring the Top Quark p_T Distribution **77**

5.1 Backgrounds to $t\bar{t}$ Production 78

5.2 Correlations 84

5.3 The Likelihood Fit 85

5.4 Checks of Methodology 89

5.5 Results 92

5.6 Combining The first Two Bins 93

5.7 Acceptance Corrections 95

5.8 Systematic Uncertainties 97
5.8.1 Variation of the Shape of the p_T Spectrum 98
5.8.2 Variation of the Top Quark Mass 99
5.8.3 Variation of the Background Shape 100
5.8.4 Jet Energy Scale 101
5.8.5 Initial State Radiation 104
5.8.6 Final State Radiation 107
5.9 Systematic Uncertainties due to the Relative Acceptance 109
5.10 Setting a 95% C.L. Upper Limit 111
5.11 High p_T Acceptance 113

6 Conclusions **117**

A The CDF Collaboration **119**

B The KS Test **125**

List of Figures

1.1 The lowest order Feynman diagrams for the hadroproduction of $t\bar{t}$ pairs. . . 10

1.2 The top quark p_T distribution for various new physics scales. We present the LO predictions for the p_T distributions for QCD hadroproduction of top quark pairs in addition to a four-fermion interaction representing potential new physics. The top plot shows the distributions expected for a color-singlet s channel operator, whereas the lower plot shows what is expected for the corresponding color-octet operator. A top quark mass of 160 GeV/c^2 is assumed. From [31] 13

1.3 The top quark p_T distribution for various new physics scales. We present the LO predictions for the p_T distributions for QCD hadroproduction of top quark pairs in addition to a color octet vector resonance representing potential new physics. The top plot shows the distributions expected for additive interference between QCD and the new interaction, whereas the lower plot shows what is expected for the case where destructive interference occurs. A top quark mass of 160 GeV/c^2 is assumed. From [31] 14

2.1 A schematic diagram of the Fermilab accelerator complex. 18

2.2 An isometric view of the CDF detector. 21

2.3 Diagram of the electromagnetic compartment in a central calorimeter wedge. The towers are numbered 0-9, starting from the lowest $|\eta|$ values. 23

2.4 A diagram of an SVX barrel. The SVX is composed of two such barrels, longitudinally aligned along the beamline. 28

2.5 A transverse view of a CTC endplate. The tilt of the wire planes relative to the radial direction is evident. 31

2.6 Coverage of the central muon subsystems in $|\eta|$ and ϕ. 33

2.7 The location of of a central muon (CMU) wedge in both the azimuthal (left picture) and polar (right picture) views. 34

2.8 Diagram of a central muon module. A muon track is depicted, with two measured drift times (t_2 and t_4) shown. These times can give a crude measurement of the muon momentum that can then be employed in a low level trigger. 35

3.1 A Feynman diagram for W + jets production. This is the principle background source in our data sample. 49

3.2 The p_T distributions for two different VECBOS samples compared with a distribution composed of 70% $Q^2 = \langle p_T \rangle^2$ VECBOS and 30% non-isolated $W + 3.5$ jet data. We choose this combination due to the fact that we expect approximately 30% of the background events in our data sample to contain no W-bosons. Events passing all of the selection requirements except the lepton isolation requirement are expected to originate predominantly from the "non-W" background contributions, and are referred to as non-isolated W data. 51

3.3 A schematic diagram of a displaced vertex. The primary vertex is the $p\bar{p}$ interaction point, whereas the secondary vertex arises from the subsequent decay of a heavy quark. The impact parameter, d, is the distance of closest approach to the fitted primary vertex in the $r - \phi$ plane. L_{xy} is defined to be the distance, in the transverse plane, between the primary and secondary vertices. Events with negative L_{xy} are those in which the secondary vertex lies in the opposite hemisphere to the associated jet (see text), as shown below. 53

3.4 Sample Feynman diagrams for Wc and $Wb\bar{b}$ production. These are both important sources of background to b-tagged $t\bar{t}$ candidate events. 55

4.1 Uncertainty in the different terms contributing to CDF's jet corrections. The cone size used is $R = 0.4$. 60

4.2 The HERWIG predictions for the shape of the p_T distributions for quarks arising from top quark decay. The dashed distribution corresponds to the b-quarks, the solid distribution to the light quarks. 62

4.3 The $t\bar{t}$-specific jet energy corrections that are applied to jets based on the available information from the kinematic fit and the b-taggers. The four separate curves apply to A) jets arising from decays of the W boson, B) jets assigned to b-quarks by the kinematic fit, but possessing no SLT tag, C) jets with a soft electron tag, and D) jets with a soft muon tag. 64

4.4 The number of additional jets (beyond the first four) in HERWIG Monte Carlo events that pass our selection criteria. In this plot, we define a 'jet' to have $|\eta| < 2.4$, $E_T > 8$ GeV/c. 66

4.5 The p_T resolution functions for Monte Carlo events passing the selection criteria of the mass analysis. The kinematic fit is constrained to return a top mass of 175 GeV. This plot includes both the semileptonically-decaying and hadronically-decaying top quarks in the standard HERWIG sample. To aid in making the comparison, the distributions are normalized to the number of events in the untagged sample. 69

4.6 A comparison of the smeared and true distributions for two different models of top quark production. The smeared distribution is plotted with error bars. Although the plots are made for a high statistics Monte Carlo sample, the sizes of the error bars on the smeared distribution are determined by what is expected for the 61 Event sample that passes our final selection criteria. The left plot is for the Standard Model and the right is distribution with enhanced hard top quark production. 70

4.7 Fits to the reconstructed p_T distribution in each of four true p_T bins. This plot includes only the hadronically-decaying top quarks, and assumes a Standard Model top quark p_T distribution within each bin. The Monte Carlo statistics of the standard HERWIG sample have been supplemented at high p_T by additional Monte Carlo production. 71

4.8 Comparison of the measured p_T distribution for the single tag and no tag case in the second true p_T bin (75 GeV/c< p_T <150 GeV/c). There are approximately 1000 events in each distribution. Similar effects exist for the other three bins of true p_T, but are most pronounced in this bin. Only the p_T reconstructed using the hadronically-decaying top quark candidate is used. 72

4.9 Comparison of the measured p_T distribution for the lepton-side and jet-side case in one true p_T bin. This bin is where effects due the top quark decay mode are most evident. 73

4.10 Comparison of the measured p_T distribution for the mass-constrained and unconstrained fits in the true p_T bin $150 < p_T < 225$ GeV. The standard mass selection criteria as well as the $\chi^2 < 10$ cut are applied in each case. . 75

5.1 A scatter plot of the reconstructed p_T for the semileptonic and hadronic decay of the top quark in each event for the data (stars) and HERWIG (dots) Monte Carlo samples. 85

5.2 The response functions for the case where we assume a flat true p_T distribution within each bin compared to the results obtained assuming a Standard Model distribution within each bin. The response functions for events having one or more b tags are plotted. 86

5.3 The linear approximation used in order to estimate the true p_T distribution from the data. The data points shown here are the raw values returned from the MINUIT mass fitter. 88

5.4 The resolution function for R_1 in the Monte Carlo experiments described in Section 5.4. Superimposed is a fit to a Gaussian distribution. 91

5.5 The resolution function for R_2 in the Monte Carlo experiments described in Section 5.4. Superimposed is a fit to a Gaussian distribution. 92

5.6 The resolution function for R_3 in the Monte Carlo experiments described in Section 5.4. Superimposed is a fit to a Gaussian distribution. 93

5.7 The resolution function for R_3 in the Monte Carlo Experiments described in section 5.4. Only those events satisfying the cut $R_3 > 10^{-8}$ are plotted here. Superimposed is a fit to a Gaussian distribution. 94

5.8 The distribution of outcomes for R_4 in the Monte Carlo Experiments described in section 5.4. 95

5.9 The p_T distribution for the hadronically-decaying top quarks in the constrained mass sample. The shaded distribution is the estimated background distribution, with the shape as predicted by VECBOS. 96

5.10 The true p_T distributions that enter into our calculation of the systematic uncertainties on the residual bias in the methodology. 99

5.11 Comparison of the background p_T distribution predicted by VECBOS for two different renormalization scales. 102

5.12 A comparison of the p_T error distributions for events with a Standard Model $p_T(t\bar{t})$ distribution and the subset of events having $p_T(t\bar{t}) > 30$ GeV. 106

5.13 A comparison of the N_{jet} distributions for events with a Standard Model $p_T(t\bar{t})$ distribution and the subset of events having $p_T(t\bar{t}) > 30$ GeV. VECBOS Monte Carlo, normalized to the expected background contribution, is added to take into account the W + jets background. We define a "jet" as having $E_T > 15$ GeV and $|\eta| < 2$. 107

5.14 Plots of the reconstructed p_T distribution in each of four true p_T bins. This plot includes only the hadronically-decaying top quarks. The Monte Carlo statistics of the standard HERWIG sample have been supplemented at high p_T by additional PYTHIA Monte Carlo production in the high p_T regime. . . 114

5.15 A study of the acceptance above 300 GeV/c. We present here the ration between the GENP p_T distribution of events passing our selection criteria to the GENP p_T distribution of all events. The relative acceptance between 300 and 330 GeV/c is approximately the same as in the region between 225 and 300 GeV/c. 116

Chapter 1

The Top Quark

The idea that all matter is composed of smaller, essentially indivisible constituents is an old one, a fact belied by the ancient Greek origins of the word "atom". Democritis, in the fourth century B.C. postulated that matter could be further and further subdivided until a basic, fundamental constituent was obtained. The idea remained only a speculation for over 2000 years, until in 1895, Röntgen's discovery of x-rays[1] lead to a flurry of activity in experimental atomic physics. This included J.J. Thompson's model of the atom as a large number of electrons surrounded by a cloud of balancing positive charge. In 1911, Rutherford's experimental measurement of atomic structure[2] challenged Thompson's view of the atom, and the study of the atomic nucleus became a primary focus of activity. Rutherford himself proposed the existence of the neutron as early as 1920, and it was noted in 1932 by Chadwick that the experimental data on the reaction

$$ {}^{4}_{2}He + {}^{9}_{4}Be \rightarrow {}^{12}_{6}C + {}^{1}_{0}n \tag{1.1} $$

was not consistent with the ${}^{12}_{6}C$ atom recoiling against a gamma ray[3], as had been originally supposed. He further proposed that the particle against which the carbon atom was recoiling against was the neutral nuclear partner of the proton.

As physicists began to delve more deeply into the subatomic world, an increasingly-disturbing number of ostensibly "fundamental" particles began to enter the picture. One of the first to be discovered was the muon[4], originally mistaken for a particle (known as the

pion) whose existence was proposed on theoretical grounds by Hideki Yukawa[5]. Yukawa's idea that the force responsible for holding nuclei together (the "strong interaction") could be understood in terms of pion exchange represented a fundamental shift in the way physicists looked at nuclear forces. Based on estimates of the range of the strong interaction, Yukawa was able to predict the mass of this pion, which was discovered in cosmic ray interactions 1947[6]. Although Yukawa's theory was only approximately correct, the idea of a force being mediated by particle exchange is central in modern particle physics. For example, the strong force is now thought to be mediated by the exchange of a massless particle known as a "gluon", the electromagnetic force is thought to be mediated by photon exchange, and another force, known as the weak interaction, is thought to be mediated by massive vector bosons known as the W and Z.

In the 30 years that followed the discovery of the neutron, a literal explosion of new hadronic[1] particles were discovered. The proliferation of the number of hadrons indicated that perhaps these particles were, as in the case of the "atom", not as fundamental as was first supposed. In an effort to find a pattern in the spectroscopy of the known hadrons, Gell-Mann and Zweig independently proposed in 1961[7] that the hadrons could be organized into representations of the group SU(3). The integral-spin "mesons" (such as the pion) occurred in singlets and octets whereas the half-integral spin "baryons" (such as the proton) occurred in singlets, octets and decuplets. Particles in a given representation shared a common spin and parity.

In the language of group theory, these observations can be explained as follows. For the mesons

$$\mathbf{3} \otimes \bar{\mathbf{3}} = \mathbf{1} \oplus \mathbf{8} \tag{1.2}$$

That is, the observed patterns of meson quantum numbers could be explained by hypothesizing that they are actually built up from a combination of two fundamental triplet representations of SU(3). For the Baryons, the observed patterns were consistent with a combination

[1] "Hadrons", as opposed to "leptons" are those particles that feel the strong interaction.

of three of these fundamental representations.

$$\mathbf{3} \otimes \mathbf{3} \otimes \mathbf{3} = \mathbf{1} \oplus \mathbf{8} \oplus \mathbf{8} \oplus \mathbf{10} \tag{1.3}$$

It became natural at this point to hypothesize the existence of three kinds of so-called "quarks". The three spin-1/2 particles presumed to be the constituents of the observed hadrons were called "up", "down", and "strange" quarks. In the quark model, mesons are thought to be composed of quark-antiquark pairs whereas baryons are thought to be composed of three quarks. A number of predictions were made possible by grouping the observed particles in this way, including the prediction of the existence of a particle known as the Ω^-, a particle composed of 3 strange quarks that was subsequently discovered in 1964[8]. Another particle, known as the Δ^{++}, was composed of three quarks with identical quantum numbers, in apparent violation of the Pauli exclusion principle. The solution was to add an additional quantum number to the quarks, known as "color", which also serves as the equivalent of electric charge in the modern theory of the strong interaction, namely Quantum Chromodynamics (OCD). Furthermore, beginning with the pioneering work of McAllister and Hofstadter[9], a series of high energy $e-p$ scattering studies using the linear accelerator at SLAC[10], resulted in data consistent with the proton being composed of several pointlike constituents.

At this point, studies of e^+e^- collisions at center-of-mass energies above 3 GeV began to yield fruit. A third charged lepton, heavier than the proton and referred to as the τ lepton was observed at SLAC[11] only a year after the co-discovery of a new meson, known as the J/ψ, occurred there[12]. The unexpectedly long lifetime and large mass of the J/ψ meson indicated that it was composed of a pair of quarks of a type or "flavor" never before observed. The observation of these so-called "charm" quarks simultaneously explained the troublesome non-observation of certain decays of strange mesons, through a theoretical proposal known as the GIM mechanism[13]. Any suspicion of alternative models for the strong interaction (aside from QCD) was quickly vanishing, particularly in light of experimental evidence for "jets" in e^+e^- collisions at center-of-mass energies approaching 7.4 GeV[14]. Jets, in this context, were defined as groups of particles with similar trajectories assumed to arise from

a common quark.

Leon Lederman pushed the search for new quarks to higher energy regimes, finally observing a new resonance, analogous to the J/ψ, in 400 GeV proton-nucleus collisions[15]. The decay properties of this resonance once again heralded the arrival of a new "flavor" of quark, the bottom quark. The study of the bottom quark, and the measurement of the properties of its associated mesons, is one of the most active fields in particle physics today.

Finally, in 1994 the CDF collaboration reported evidence for the existence of a sixth quark, known as the "top" quark[16]. This observation was subsequently confirmed by both the CDF and D$\emptyset$ collaborations[17]. The top quark, weighing approximately as much as a tungsten nucleus, was pair-produced in $p\bar{p}$ collisions at a center-of-mass energy of 1.8 TeV, and identified by its decays into energetic leptons and jets, some of which originate from the bottom quarks produced by top quark decay. The study of the properties of the top quark is in its infancy, and it is the purpose of this dissertation to document the first measurement of the top quark transverse momentum distribution.

1.1 The Standard Model

At this point, the known quarks and leptons can be grouped as follows.

$$\begin{pmatrix} e \\ \nu_e \end{pmatrix} \begin{pmatrix} \mu \\ \nu_\mu \end{pmatrix} \begin{pmatrix} \tau \\ \nu_\tau \end{pmatrix} \tag{1.4}$$

$$\begin{pmatrix} u \\ d \end{pmatrix} \begin{pmatrix} c \\ s \end{pmatrix} \begin{pmatrix} t \\ b \end{pmatrix} \tag{1.5}$$

The doublet grouping depicted above, where nature's fundamental fermions are grouped into three "generations" of quarks and leptons is a product of the "Standard Model" of particle physics[18]. In this model, the electromagnetic, weak, and strong forces are described by mathematical entities known as "gauge theories", in which interactions are described in terms of boson exchange. For example, the electromagnetic interaction described in terms of an unbroken U(1) symmetry. This means that the form of the interaction can be derived

simply by demanding that it be invariant under the following local gauge transformation.

$$\psi(x) \rightarrow e^{iq\lambda(x)}\psi(x) \tag{1.6}$$

$$A_\mu(x) \rightarrow A_\mu(x) + \partial\lambda(x)/\partial x_\mu \tag{1.7}$$

In this equation, $\psi(x)$ and $A_\mu(x)$ are the fermion and photon fields, respectively. The symbol q represents the fermion-photon coupling, and $\lambda(x)$ is an arbitrary function of space-time. The theory of the electromagnetic interaction is based on a simple phase-factor (U(1)) transformation. However, by finding the appropriate symmetry group, the strong and weak interactions can also be described by gauge symmetries.

The weak interaction, in particular, is described by a broken $\mathrm{SU(2)_L}$ symmetry. The symmetry is said to be "broken" due to the fact that the corresponding gauge bosons are massive, and the "L" appears due to the fact that the gauge transformations operate only on particles with left-handed spins relative to their motions. The left-handed nature of the weak interaction is very important, in particular due to the fact that, for theories in which the left-handed and right-handed couplings are different, so-called "chiral" or "triangle" anomalies can occur. Due to these anomalies, the amplitudes corresponding to interactions containing certain closed fermion loops can become infinite in an awkward way. The only way for such anomalies to cancel is if the contribution from each of the fermions in a given generation cancel. This requires the symmetric four-particle generations shown above, along with exactly three color states for quarks in QCD. Hence, after the discovery of the bottom quark, the existence of the top quark was seen almost as a fait accompli.

Interestingly enough, both the weak and electromagnetic interactions are thought to originate from a common $\mathrm{SU(2)}\otimes\mathrm{U(1)}$ "electroweak" gauge theory. This common symmetry is broken by a mechanism known as the "Higgs" mechanism[19], resulting in the individual $U(1)$ and $\mathrm{SU(2)_L}$ gauge theories that have been previously mentioned. Explaining all of nature's interactions in terms of a common symmetry is an idea known as "unification", and is one of the primary goals of modern particle physics.

1.1.1 Limitations of the Standard Model

In the Standard Model, particle masses are accommodated by a mechanism known as the Higgs mechanism. In this calculation, a doublet of scalar fields is introduced in order to break electroweak symmetry and to allow the fermion masses to enter into the Standard Model Lagrangian. This results in the prediction of a neutral scalar particle known as the "Higgs Boson". The exact form of the Higgs sector is somewhat arbitrary, and this mechanism alone is unsatisfactory for a variety of reasons.

Following the exposition in [20], we can show that the Standard Model cannot be consistent to arbitrarily high energy scales. We parameterize the strength of the Higgs boson's coupling by $\lambda(\mu)$[2]. The function that describes the variation of an interaction's coupling as a function of energy is known as a β-function. For the Higgs self-coupling at an energy scale μ, this function can be written

$$\beta_{\mathrm{H}}(\lambda) = \frac{3\lambda(\mu)^2}{2\pi^2}. \tag{1.8}$$

Hence, the coupling at the scale μ is related to the coupling at a higher scale Λ by

$$\frac{1}{\lambda(\mu)} = \frac{1}{\lambda(\Lambda)} + \frac{3}{2\pi^2}\ln\frac{\Lambda}{\mu}. \tag{1.9}$$

We must have $\lambda(\Lambda) > 0$ for the Higgs potential to be bounded below, and we can thus write

$$\lambda(\mu) \leq \frac{2\pi^2}{3\ln\frac{\Lambda}{\mu}}. \tag{1.10}$$

We see that by taking the limit $\Lambda \to \infty$, $\lambda(\mu) \to 0$ for all μ. In this limit, we are left with the theory of a free scalar field, which makes no interesting predictions. Thus, the Standard Model must be regarded as a sort of effective theory: one that is valid only beneath some energy scale that we choose to denote by Λ_∞. When we try to apply the Standard Model to scales as high as Λ_∞ it ceases to make predictions. Now, if we ignore the first term in (1.9) then we obtain the following expression for the mass of the Higgs boson

$$M_H = \sqrt{2\lambda(M_H)}v = \frac{2\pi v}{\sqrt{3\ln(\Lambda_\infty/M_H)}}. \tag{1.11}$$

[2]The potential for the Higgs field, ϕ, is normally written $V(\phi) = -v^2\lambda|\phi|^2 + \lambda\phi^4$.

Trying different sets of numbers in (1.11), we see that for small Higgs masses, the cutoff can become larger than the unification scale. A theory with a light Higgs boson can be self-consistent to a very high energy scale. Currently, Standard Model Higgs bosons with mass less than 91 GeV/c^2 are excluded at the 95% confidence level[21].

The triviality of the Standard Model can be seen to be representative of its inability to provide satisfactory answers to a number of important theoretical questions. For example, there is no explanation for the origin of the energy scale of electroweak symmetry breaking. One simply assigns the correct vacuum expectation value $v \simeq 246$ GeV to the ground state of the Higgs field. Thus, the scale at which electroweak symmetry is broken is established by fiat, rather than as the result of a dynamical calculation. Furthermore, the Yukawa couplings of the fermions, which dictate their masses through the relation

$$m_f = \lambda_f v, \tag{1.12}$$

seem to follow a rather peculiar distribution. In particular, for most of the elementary fermions, the Yukawa couplings are very tiny:

$$\lambda_e, \lambda_d, \lambda_u \sim 10^{-5} \tag{1.13}$$

whereas for the top quark, $\lambda_t \sim 1$. According to the Standard Model, the mass spectrum of the fermions is pure happenstance. There is no physics reason for it's peculiar nature.

The origin of the mass spectrum of the fermions is one of the current mysteries of particle physics. It is known as the problem of flavor physics. Like the problem of electroweak symmetry breaking, it has to do with the breaking of a fundamental symmetry: flavor symmetry.

We can formulate one final criticism of the Standard Model. A problem appears when the Standard Model is embedded in some larger, unified, theoretical structure, such as the SU(5) unification model[22]. In order to account for the masses of the weak vector bosons, which are known as the W and Z bosons, the Higgs scalar that breaks electroweak symmetry must have a mass of the same order of magnitude as v. Similarly, the Higgs boson responsible for breaking SU(5) must have a mass of order 10^{15} GeV. However, the

two Higgs bosons will mix and in the absence of cancellations, the electroweak-breaking Higgs boson will also have a mass of order 10^{15} GeV. Keeping the two mass scales separate requires fine-tuning of the theory's parameters to one part in 10^{34}[23]. This fine-tuning is the result of a dramatic dependence of the electroweak Higgs boson mass on the unification scale. This is perceived to be unnatural, so that this problem is varyingly called the "gauge hierarchy" or "naturalness" problem.

1.1.2 Possible Solutions

The three deficiencies of the Standard Model outlined in the previous section have prompted a number of proposals for new physics. The most popular of these is certainly to introduce supersymmetry[26]. The introduction of a new broken symmetry is suggested by the fact that relative to the unification scale, the Standard Model Higgs boson mass is very close to zero. One might suppose that if a symmetry existed that ensured a massless Higgs boson, the breaking of this symmetry at a low energy scale might lead to a light Higgs boson without fine tuning. It turns out that supersymmetry does indeed solve the naturalness problem.

Another solution is to construct a theory without elementary scalars: this is the approach taken by most theories of dynamical electroweak symmetry breaking. In such a scheme, the Higgs sector turns out to be composite, and we generate the fermion masses by adding new gauge interactions. The most-studied implementation of dynamical electroweak symmetry breaking is called Technicolor[23, 24, 25]. In the simplest versions of Technicolor, the existence of a new QCD-like gauge interaction is postulated. This interaction binds fermion-antifermion pairs into composite systems whose behavior resembles that of the Higgs field.

Dynamical mechanisms for the breaking of electroweak and flavor symmetry can produce dramatic signals in the kinematic distributions associated with top quark pair production. Due to the magnitude of these potential signals, it is these mechanisms on which we shall focus in the discussion of top quark production from sources other than the strong interaction.

1.2 Top Quark Production

The Standard Model predicts that top quark pair production in $p\bar{p}$ collisions will be dominated by gluon exchange, a physical process described by the theory of the strong interaction, namely QCD. The aim of this dissertation is to compare the predictions for the kinematic distributions associated with top quark production with a measurement of the top quark p_T distribution, assuming that the top quark decays as predicted by the Standard Model. In this section, we give a brief overview of the theory behind top quark pair production. This will include the hadroproduction of top quark pairs, as described by QCD calculations, as well as a brief survey of the literature describing alternative $t\bar{t}$ production mechanisms.

1.2.1 Hadroproduction of $t\bar{t}$ Pairs

In this section, we describe the process

$$p\bar{p} \to t\bar{t}X \ , \tag{1.14}$$

where X is taken to represent the particles produced in association with the $t\bar{t}$ pair. Additional particles could result from initial or final state gluon radiation, or arise from interactions that occur in addition to the primary scattering process.

The tree level partonic sub-processes for the production of $t\bar{t}$ pairs in $p\bar{p}$ collisions are given by

$$q(p_1) + \bar{q}(p_2) \quad \to \quad t(p_3) + \bar{t}(p_4) \text{ and} \tag{1.15}$$

$$g(p_1) + g(p_2) \quad \to \quad t(p_3) + \bar{t}(p_4) \ , \tag{1.16}$$

where q and g denote the constituents of the proton that undergo the interaction that produces the top quark pair, and the p_i denote the four-momenta of the parton in question. The lowest-order Feynman diagrams for these processes are shown in Fig. 1.1. Applying the Feynman rules of QCD to these diagrams, it is possible to derive the matrix elements for these processes.

Figure 1.1: The lowest order Feynman diagrams for the hadroproduction of $t\bar{t}$ pairs.

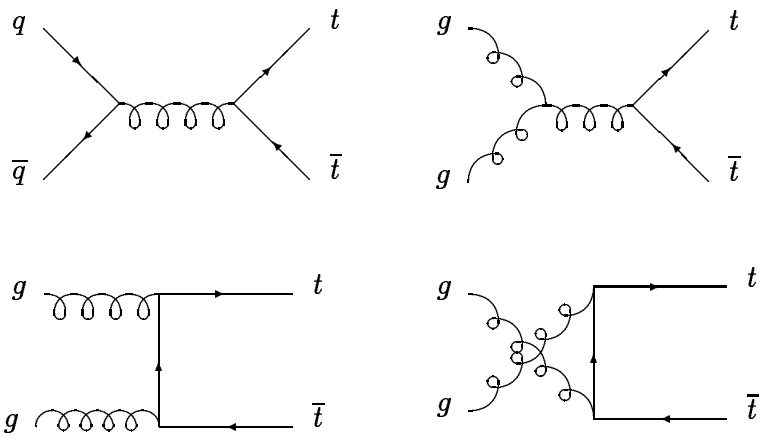

A conventional choice of kinematic variables used to describe the differential cross section is the rapidities (y_3, y_4) and transverse momentum (p_T) of the outgoing partons. In terms of these variables, it is possible to write the differential cross sections for the $q\bar{q}$ and gg subprocesses as follows[27].

$$\frac{d\sigma}{dy_3 dy_4 d^2p_T} = \frac{1}{64\pi^2 m_T^4 (1+\cosh(\Delta y))^2} \sum_{ij} x_1 f_i(x_1, Q^2) x_2 f_j(x_2, Q^2) \overline{\sum} |\mathcal{M}_{ij}|^2 \qquad (1.17)$$

In this equation, x_i is the momentum fraction of initial-state parton i, f_i is the parton distribution function appropriate for this parton, $\overline{\sum}|\mathcal{M}_{ij}|^2$ is the spin-averaged sum of the squared QCD matrix element for the interaction of partons of types i and j, $\Delta y = y_3 - y_4$ is the rapidity difference between the outgoing top quarks, and $m_T = \sqrt{p_T^2 + m_t^2}$ is referred to as the "transverse mass".

The $\overline{\sum}|\mathcal{M}_{ij}|^2$ take on the following form as the rapidity separation between outgoing partons becomes large:

$$\overline{\sum}|\mathcal{M}_{q\bar{q}}|^2 \sim \text{constant , and} \qquad (1.18)$$

$$\overline{\sum}|\mathcal{M}_{gg}|^2 \sim e^{\Delta y} \ . \qquad (1.19)$$

Combining this result with equation 1.17 allows the observation that the dominant contribution to the total cross section will arise from the region of small Δy. Interestingly

enough, we see that top quarks produced by $q\bar{q}$ annihilation will tend to be more strongly correlated in rapidity than those produced by gg fusion.

Furthermore, by examining the propagators for the diagrams shown in Fig. 1.1, we can show that the kinematics of top quark production should be reasonably well described by a leading-order calculation. The denominators of the appropriate propagators can be written as

$$(p_1 + p_2)^2 = 2m_T^2(1 + \cosh \Delta y), \tag{1.20}$$

$$(p_1 - p_3)^2 - m_t^2 = -m_T^2(1 + e^{-\Delta y}), \tag{1.21}$$

$$(p_2 - p_3)^2 - m_t^2 = -m_T^2(1 + e^{\Delta y}). \tag{1.22}$$

One important result from this calculation is the observation that the propagators are off shell by at least m_t. Since m_t is known to be much larger than the QCD scale, we can make an important distinction between light quark production and the production of top quarks. In the case of light quark production, the propagators making the dominant contributions will be those very close to being on shell, thus representing a momentum transfer less than the QCD scale. At this point, a perturbative analysis breaks down. For top quark production, however, we are well separated from this regime, and can thus employ perturbative predictions with relative confidence. This simple argument is further supported by the more sophisticated analyses discussed in [28].

We can also note at this point that, since the differential cross section falls as $1/m_T^4$, we can expect the contributions arising from top quarks produced with p_T greater than m_t to be suppressed in the Standard Model. It is thus this high-p_T regime that we expect to be most sensitive to top quark production from sources other than the strong interaction.

1.2.2 Anomalous Top Quark Production

Several models[29, 30, 32] of dynamical electroweak and flavor symmetry breaking predict modifications of the top quark kinematic distributions. A particularly interesting example is the Topcolor model that were first discussed in [31]. A feature that the Topcolor model shares with almost all Technicolor[33] models is that the new physics couples preferentially

to the third generation.

Examining kinematic distributions is in some ways a more sensitive test of the Standard Model than a measurement of the absolute cross section. This is because the momentum transfers involved are very large, meaning that the calculation of the kinematic distributions is entirely perturbative. Hill and Parke have examined the sensitivity of various kinematic distributions in $t\bar{t}$ events to nonstandard top quark production mechanisms. The effects of both s-channel color-singlet and color-octet four-fermion operators were considered. At first glance, the effect of such terms is simply an increased production cross section. Certainly, the $M_{t\bar{t}}$ distribution has virtually no sensitivity to such operators. However, a potentially significant shift in the top quark transverse momentum (p_T) distribution towards higher p_T allows some sensitivity to physics at the 0.5 TeV scale. This is illustrated in Fig. 1.2.2, where the top quark p_T distribution for these two scenarios is depicted for a several new physics scales.

Severe distortions in both the $M_{t\bar{t}}$ and p_T distributions can, however, occur for new resonances in $t\bar{t}$ production. For example, one can model a new color-octet vector resonance, similar to the resonances predicted by Topcolor, of mass M and width Γ by replacing the gluon propagator by[31]

$$\frac{g^2}{s} \rightarrow \frac{g^2}{s} + \frac{\kappa g^2}{s - M^2 + iM\Gamma}, \tag{1.23}$$

where κ is a scale factor for the strength of the resonance's coupling relative to QCD. This, and similar analyses reveal that for couplings of approximately QCD strength, $t\bar{t}$ production can be sensitive to the production of new resonances at the TeV scale[34]. We present the outcome of the appropriate calculations in Fig. 1.2.2.

Finally, there exist other possibilities. One such possibility is proposed in [35], where it is shown that for some choices of parameters, a color octet Technicolor particle known as the ρ_T^8 could decay via

$$\rho_T^8 \rightarrow g\Pi_T \rightarrow gt\bar{t} \tag{1.24}$$

with an appreciable branching ratio. The experimental signature of this process would be a hard gluon recoiling against a $t\bar{t}$ pair. In section 5.13, we shall consider scenarios such as this one.

Figure 1.2: The top quark p_T distribution for various new physics scales. We present the LO predictions for the p_T distributions for QCD hadroproduction of top quark pairs in addition to a four-fermion interaction representing potential new physics. The top plot shows the distributions expected for a color-singlet s channel operator, whereas the lower plot shows what is expected for the corresponding color-octet operator. A top quark mass of 160 GeV/c^2 is assumed. From [31]

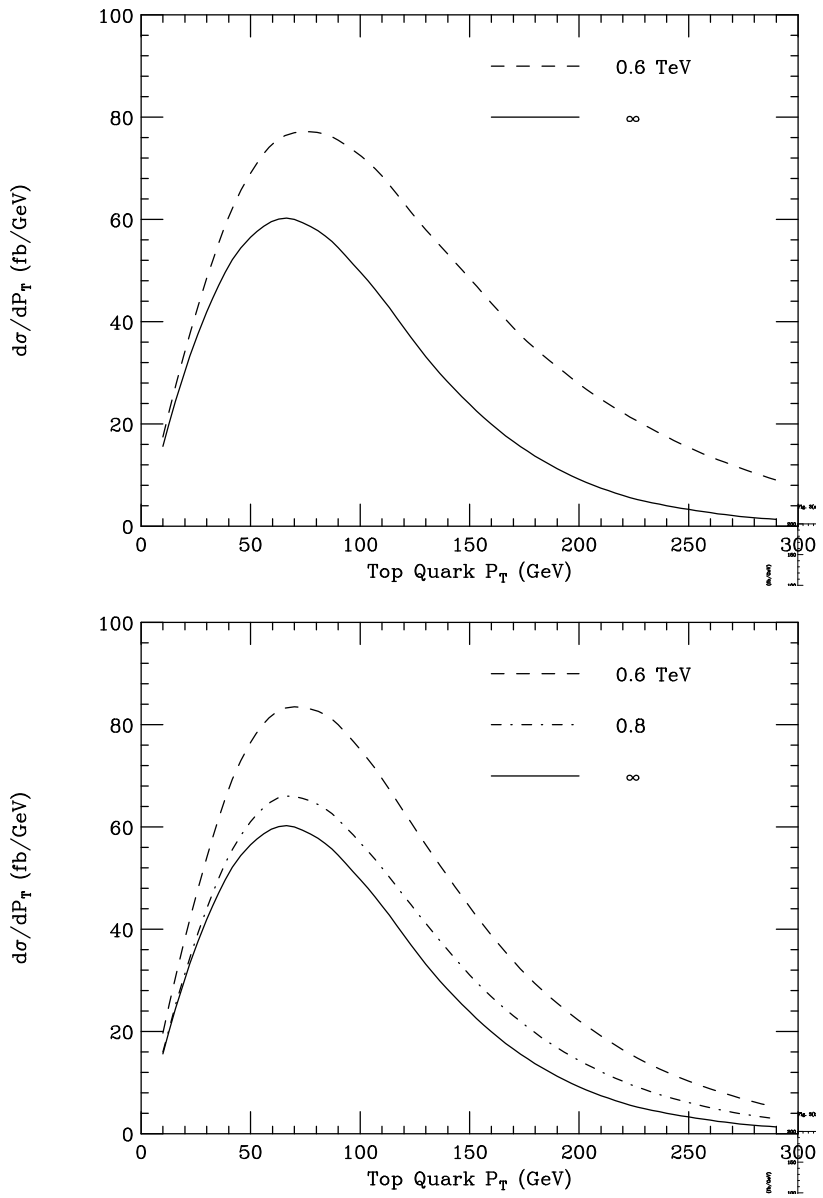

Figure 1.3: The top quark p_T distribution for various new physics scales. We present the LO predictions for the p_T distributions for QCD hadroproduction of top quark pairs in addition to a color octet vector resonance representing potential new physics. The top plot shows the distributions expected for additive interference between QCD and the new interaction, whereas the lower plot shows what is expected for the case where destructive interference occurs. A top quark mass of 160 GeV/c^2 is assumed. From [31]

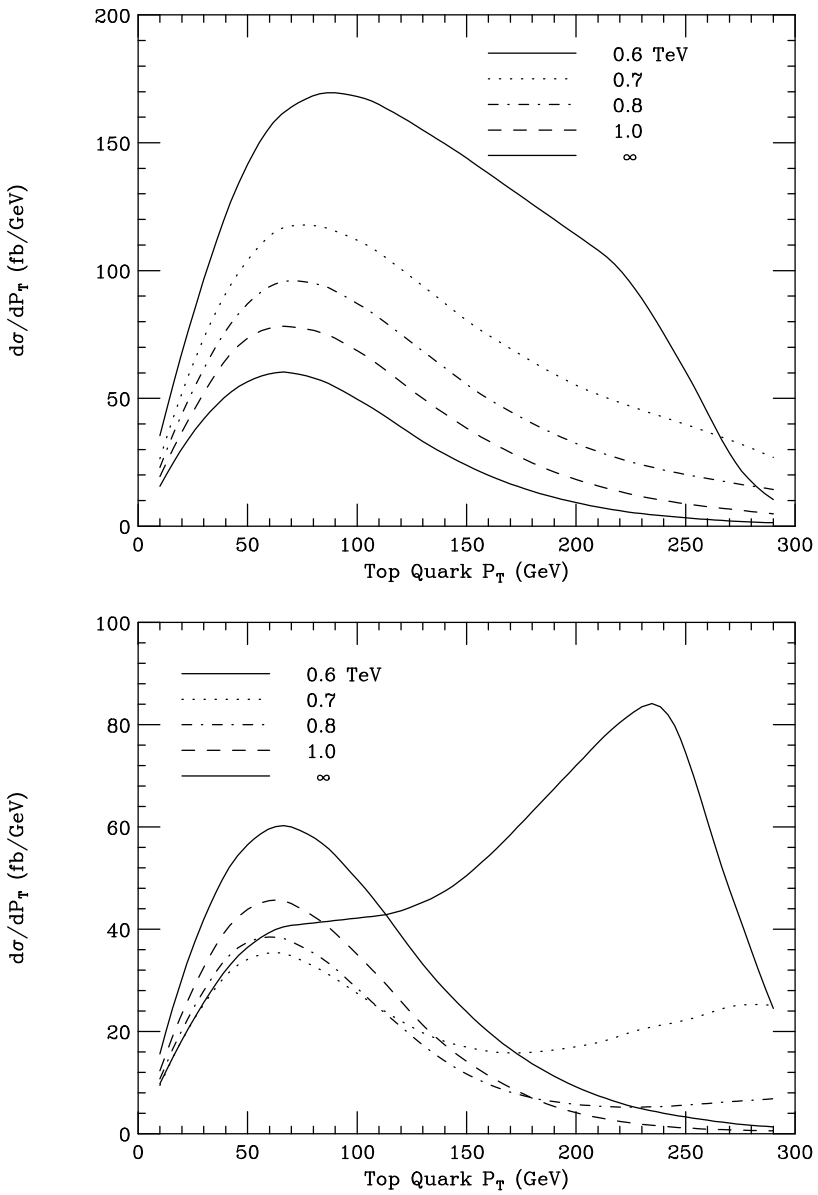

1.3 Overview of Dissertation

This dissertation describes the selection and subsequent reconstruction of $t\bar{t}$ pairs produced in $p\bar{p}$ collisions at $\sqrt{s} = 1.8$ TeV. The principle goal of the analysis is to measure the top quark p_T distribution. In particular, previous analyses of $t\bar{t}$ kinematics (see [36] for example) have not taken into account biases introduced during $t\bar{t}$ event reconstruction. In contrast, the goal of the analysis described in this dissertation is to extract a set of confidence intervals on the fraction of top quarks produced in four different regions of p_T. In principle, these confidence intervals can be compared directly to theoretical predictions for $t\bar{t}$ kinematic distributions.

We select $t\bar{t}$ events in which one top quark decays semi-leptonically, while the remaining top quark decays hadronically. This is known as the "lepton + jets" final state, and it provides the most statistically-significant measurement of top quark kinematics. The requirement of a high-p_T lepton in the final state greatly improves the signal-to-noise ratio, and the requirement that one W-boson decays hadronically assists in reconstructing the final state kinematics.

The analysis proceeds by reconstructing these events in a kinematic fit, similar to the one used in the measurement of the top quark mass[37]. This fit provides a methodology for assigning the observed "physics objects" in the final state to the partons from which they evolved, thus reconstructing the $t\bar{t}$ production kinematics on an event-by event basis.

Due to ambiguities in assigning the observed final state particles to daughters of the two top quark decays in the event and imperfect measurements of the momenta of these particles, the kinematic fit introduces biases into the measured kinematic variables. A likelihood methodology is used to correct for these biases, and to measure the fraction of top quarks that are produced in each of four bins of p_T. Furthermore, an upper limit on the fraction of top quarks produced with $p_T > 225$ GeV/c is calculated. These measurements provide constraints on possible top quark production by mechanisms other than the Standard Model.

Chapter 2

Experimental Apparatus

The Fermilab Tevatron Collider is, at the time of this writing, the world's highest energy synchrotron, achieving a beam energy of 0.9 TeV. This accelerator, located in Batavia, Illinois (USA), has a radius of 1.0 km and is equipped with superconducting dipole magnets that can achieve a maximum magnetic field of 4.4 T. The Collider Detector at Fermilab (CDF hereafter) is one of two detectors that operated during the period of Tevatron operation during which the data used in this analysis was obtained. This operating period was known as 'Run I', and occurred between 1992 and 1995. This chapter describes both the Tevatron and CDF as they were configured during this period.

2.1 The Fermilab Tevatron Collider

The Fermilab Tevatron, when operated in collider mode, collides protons and anti-protons at a center of mass energy of 1.8 TeV. The production, and subsequent acceleration, of these particles is accomplished by a sequence of six accelerators, depicted in Fig. 2.1. Here, we briefly describe these six accelerators and their function.

The first step in the sequence is a Crockcroft-Walton pulsed ion source, which converts gaseous H_2 molecules into H^- ions. At the point at which the ions leave the Crockcroft-Walton accelerator, they have been accelerated to 750 keV. At this point, the ions enter a 150 m linear accelerator (known simply as the "Linac"), which in turn accelerates these

Figure 2.1: A schematic diagram of the Fermilab accelerator complex.

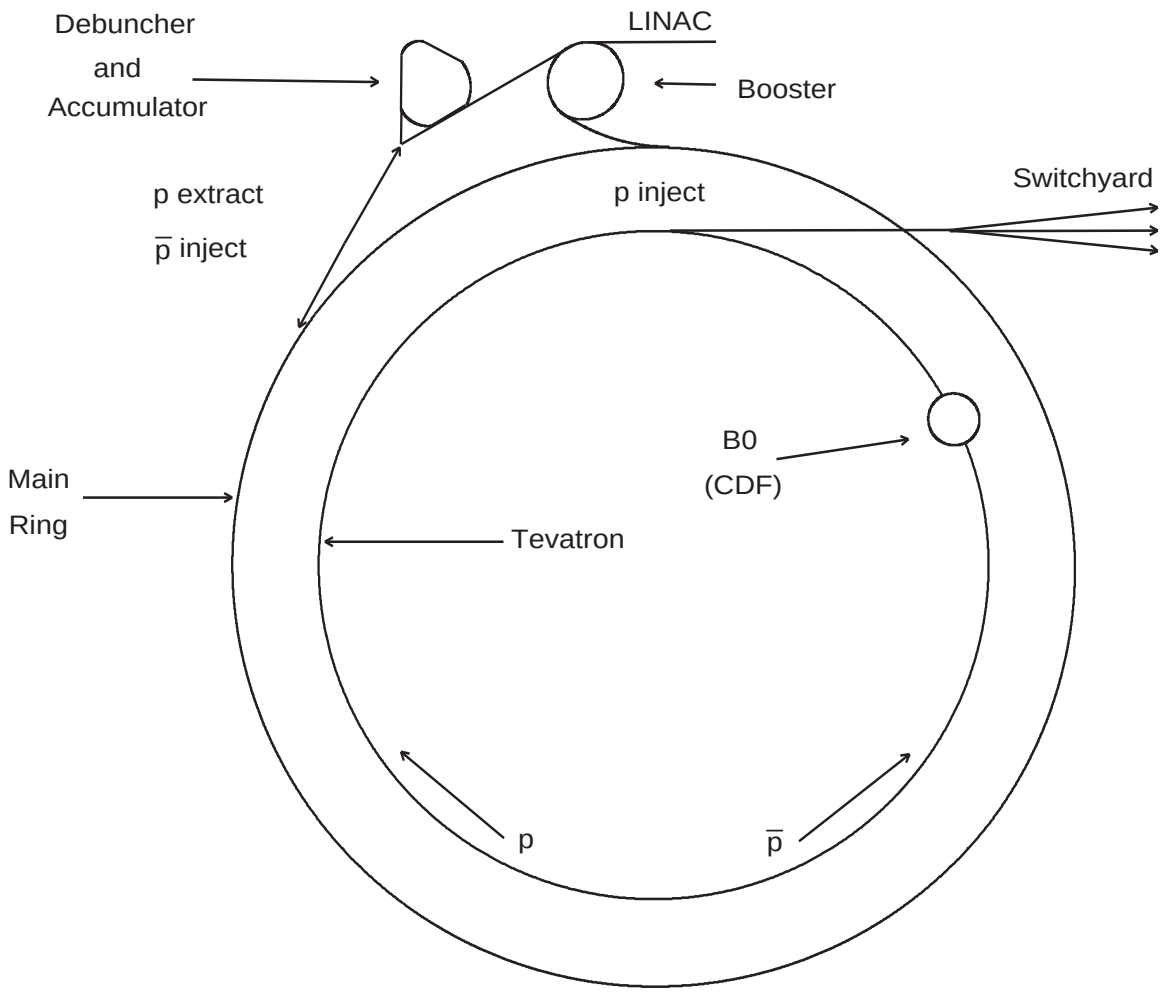

ions to 400 MeV. After the linac, the ions are passed through a copper foil that strips each ion of both electrons.

The 400 MeV proton beam is then injected into a 475 m circumference synchrotron accelerator (the Booster) which, during approximately 16 000 revolutions, accelerates the beam to 8 GeV. These 8 GeV protons are now prepared for injection into the Main Ring, a synchrotron that lies in the same tunnel as the Tevatron. The Main Ring is equipped with conventional (as opposed to superconducting) dipole magnets that can achieve a bending

field of 0.7 T. This accelerator is capable of increasing the proton beam energy to 150 GeV.

At this point the proton beam is suitable for the final stage of acceleration. This occurs in the Tevatron, whose niobium-titanium magnets lie directly below the Main Ring. The bending dipoles of the Tevatron are capable of generating magnetic fields between 0.66 and 4.4 T, a range that extends high enough to allow the beam to reach its nominal energy of 0.9 TeV. The process outlined above takes approximately one minute.

In order to obtain symmetric $p\bar{p}$ collisions, an equally-energetic antiproton beam must be produced. This process is significantly more complex, and begins with a beam of 120 GeV protons that are extracted from the Main Ring and focussed onto a 7 cm-thick metal target. The resulting proton-nucleus interactions result in the production of antiprotons, along with other particles. At this point, a liquid Lithium lens focuses the antiprotons before they are passed into the debuncher, a ring 520 m in circumference, where the phase space of the beam is reduced by means of stochastic cooling[38] and debunching[39]. Subsequently, the antiprotons enter a ring known as the "accumulator", which is concentric with the debuncher, and which stores the resulting antiprotons while others are being produced. This stage of antiproton production is known as "stacking" and it continues at a rate of about 7×10^{10} $\bar{p}$/hour [40] until approximately 100×10^{10} antiprotons have been accumulated.

During normal collider-mode operation, the Tevatron operates with six bunches of both protons and antiprotons. Due to the fact that the anti-proton production rate is a limiting factor in Tevatron luminosity, protons bunches normally consist of about 2.5×10^{11} particles while antiproton bunches contain only 7.5×10^{10} particles[1]. The protons and antiprotons propagate within the same beampipe, but in opposite directions.

There are two interaction regions at the Tevatron, known as B$\emptyset$ and D$\emptyset$. At these points the beams are strongly focussed by inner quadrupole triplets in order to collide near the center of a particle detector placed at this point. The distribution of collision points follows a Gaussian distribution with a transverse standard deviation of 35 μm and a longitudinal standard deviation of 30 cm. The bunch crossing time at the Tevatron is 3.5 μs. The beams are stored in the accelerator for a period of time that typically lasts about 10 hours, until

[1]The loss of anti-protons is due to the transfer inefficiency between the Accumulator and the Tevatron.

the luminosity has fallen off and new antiproton bunches are ready.

The data used during this analysis were procured during two operating periods of the Tevatron, known as "Run IA" and "Run IB". During "Run IA", which occurred between August 1992 and May 1993, the best instantaneous luminosity obtained was 0.92×10^{31} cm^{-2}s^{-1}, and a more typical operating value was 0.54×10^{31} cm^{-2}s^{-1}. For "Run IB", which transpired between January 1994 and July 1995, the best and typical values were 2.8×10^{31} cm^{-2}s^{-1} and 1.6×10^{31} cm^{-2}s^{-1} respectively.

2.2 Overview of the CDF Detector

The CDF detector is a magnetic spectrometer located at the B$\emptyset$ interaction region at the Fermilab Tevatron. The essential goal of the CDF detector was to identify electrons, jets and muons, and to measure the momenta of particles produced in $p\bar{p}$ collisions at approximately 2 TeV over as large a fraction of the solid angle as possible. Since the phase space for hadronic collisions is conventionally described in terms of rapidity, it is natural for the subsystems of the CDF detector to have uniform segmentation in pseudorapidity (defined as $\eta = -\ln\tan\theta/2$) and azimuthal angle (ϕ). The positive z-direction in our coordinate system is chosen to lie in the proton direction, and the origin of our coordinate system is chosen to lie at the center of the detector. This chapter, which presents an overview of the CDF detector, is based largely on [41], where a more complete overview of the detector and it's relevant subsystems can be found.

The basic design, depicted in Fig. 2.2, is similar to many other magnetic spectrometers. Inside the detector lies an evacuated beryllium beampipe, 3.5 cm in radius and 0.5 mm thick. Outside this lie the tracking subsystems, designed to measure the trajectories (or "tracks") of charged particles as they propagate outwards from the collision point. These tracking detectors are immersed in a 1.4 T magnetic field, generated by a superconducting solenoid that surrounds them. The solenoid, which is 3 m in diameter and 5 m in length, is 0.85 radiation lengths in thickness.

The detector is divided into three regions, the "central" region ($|\eta| < 1.1$), the "plug"

Figure 2.2: An isometric view of the CDF detector.

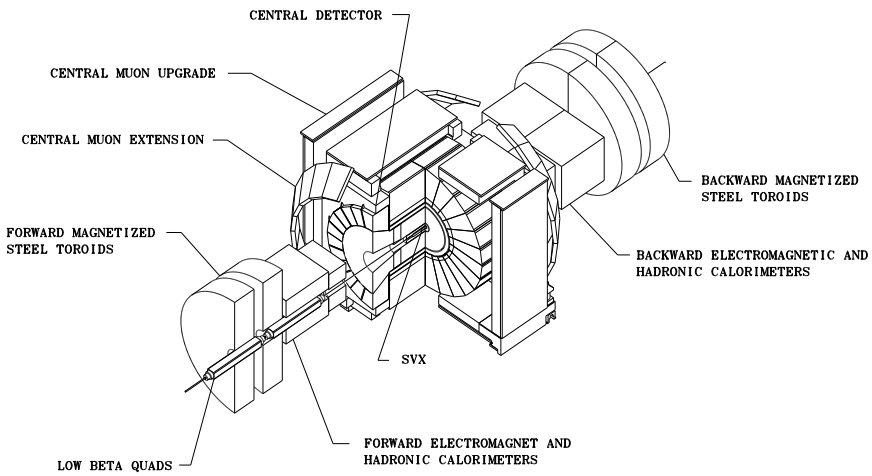

region ($1.1 < |\eta| < 2.4$), and the "forward" region ($2.4 < |\eta| < 4.2$). Each of these angular intervals is occupied by a corresponding calorimeter subsystem. These calorimeter subsystems are segmented into projective $\eta - \phi$ "towers", each of which is composed of sampling electromagnetic and hadronic shower counters. This projective tower geometry, evenly segmented in $\eta - \phi$ space, speaks of the importance of reconstructing "jets", loosely defined as collections of particles whose trajectories are grouped closely together and who are assumed to arise from a single high-energy quark or gluon.

Finally, outside the calorimetry subsystems, muon chambers allow for muon identification by measuring the trajectories of charged particles that pass through the calorimetry. In the sections that follow, we discuss these subsystems in more detail.

The calorimeters can be used to measure a quantity referred to as "missing transverse energy". The missing transverse energy, $\vec{\not\!\!E}_T$, is defined to be $-\sum_i E_T^i \hat{n}_i$, where $\hat{n}_i$ is a unit vector in the azimuthal plane pointing from the beam line to calorimeter tower i. This quantity is useful for the measurement of the transverse energy of energetic neutrinos.

2.3 Calorimetry

Sufficiently long-lived particles having transverse momentum greater than 350 MeV/c are able to traverse the tracking detectors and to create energy depositions in the calorimeters that surround the solenoid. These are sampling calorimeters, so that layers of active material alternate with layers of a metal absorber. The basic principle is that particles interact and begin to shower in the absorber, whereas the active material measures the energy flow as a function of depth. Since the characteristic length of electromagnetic showers is smaller than that of equally-energetic hadronic showers, the electromagnetic calorimeters are much smaller than, and placed inside of, their hadronic counterparts. In the analysis of top quark kinematics, calorimeters play several essential roles, such as measuring the direction and energy of jets, playing a part in electron and muon identification, and measuring any imbalance in the total transverse energy of the event.

The three principle regions of the CDF detector (central, plug and forward) are each occupied by a corresponding electromagnetic calorimeter. These are referred to as the central (CEM), plug (PEM) and forward (FEM) electromagnetic calorimeters. Behind the CEM, there are two hadronic calorimeters, the central (CHA) and wall (WHA) hadronic calorimeters. The plug and forward regions are also equipped with corresponding hadronic calorimeters, referred to as the PHA and FHA respectively.

2.3.1 Central Calorimeters

The central electromagnetic and hadronic calorimeters are divided into towers covering 15° in azimuth and 0.1 units of pseudorapidity. These towers are organized into 48 "wedges", each of which is composed of 10 towers. Figure 2.3 depicts a single central calorimeter wedge. Both the electromagnetic and hadronic calorimeters are sampling calorimeters, and alternate layers of absorber with layers of active material. The electromagnetic calorimeter alternates layers of lead with layers of polystyrene scintillator, whereas the hadronic calorimeter alternates layers of iron with layers of acrylic scintillator. Particles traveling through the scintillating medium produce light that is redirected by wavelength shifter bars

Figure 2.3: Diagram of the electromagnetic compartment in a central calorimeter wedge. The towers are numbered 0-9, starting from the lowest $|\eta|$ values.

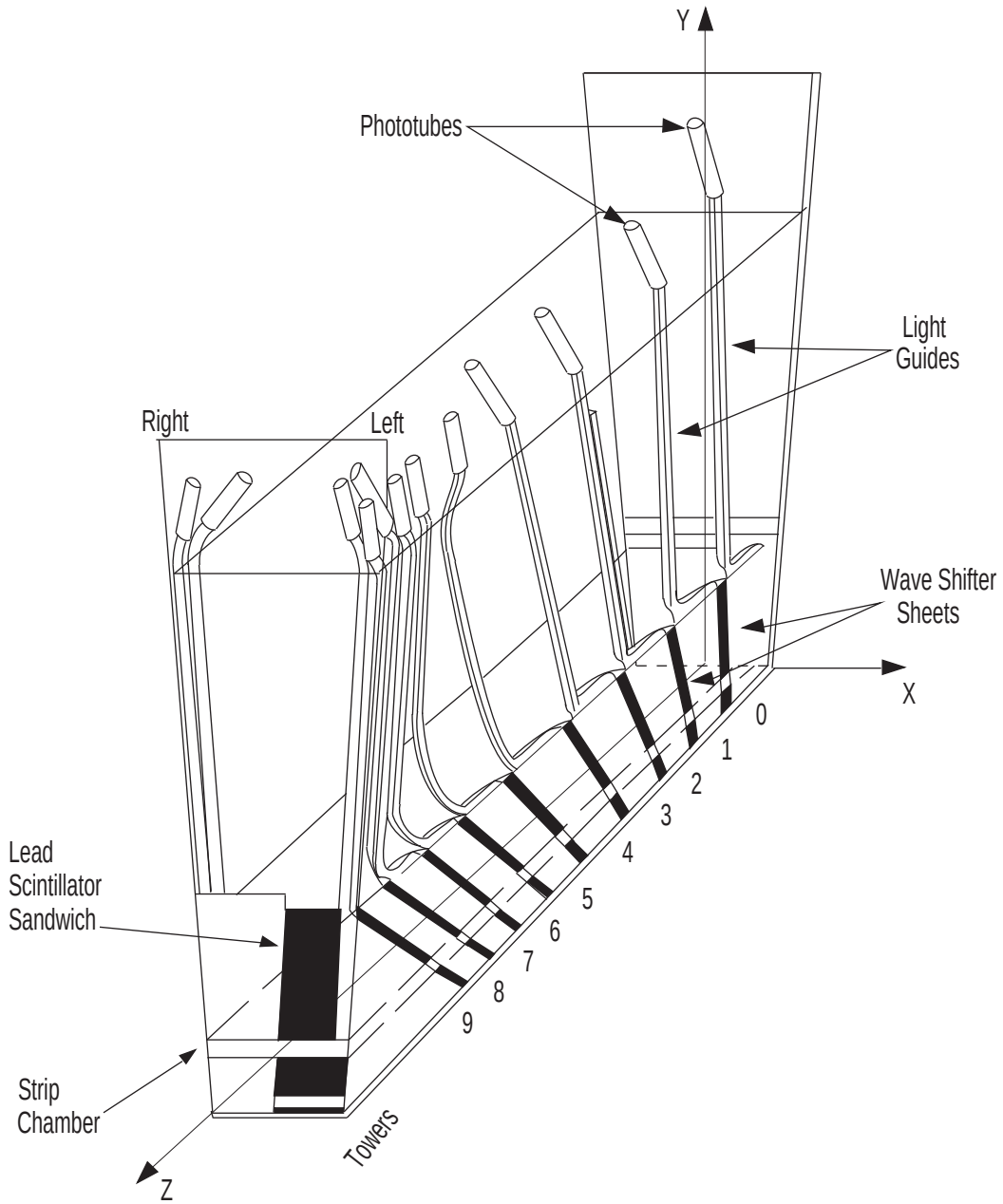

and transmitted by acrylic lightguides to photomultiplier tubes located at the back of each wedge.

The CEM has 18 radiation lengths worth of material, an inner radius of 173 cm, and a depth of 35 cm. In order to maintain a constant thickness in radiation lengths as the polar

Table 2.1: Summary of the properties of the central calorimeter. Calorimeter thicknesses are given in nuclear interaction lengths for the hadronic subsystems and radiation lengths for the electromagnetic calorimeters.

	Central EM	Central Hadron	Endwall Hadron
Coverage ($\|\eta\|$)	0-1.1	0-0.9	0.7-1.3
Tower size ($\delta\eta \times \delta\phi$)	$0.1 \times 15^\circ$	$0.1 \times 15^\circ$	$0.1 \times 15^\circ$
Module Length	250 cm	250 cm	100 cm
Module Width	15°	15°	80 cm
Number of Modules	48	48	48
Number of Layers	31	32	15
Scintillator	Polystyrene	Acrylic	Acrylic
Scintillator Thickness	0.5 cm	1.0 cm	1.0 cm
Absorber	Pb	Fe	Fe
Thickness	18 X_0	4.7 λ_I	4.5 λ_I

angle of the incident particle increases, inert plastic is substituted for lead as the polar angle increases. It was originally calibrated using testbeam electrons and is periodically checked using ^{137}Cs sources. The energy resolution, σ, for electromagnetic showers is measured to be

$$(\sigma/E)^2 = (0.137/\sqrt{E_T})^2 + (0.02)^2 \ , \tag{2.1}$$

where E is the energy of the shower and E_T is it's transverse energy. A more complete summary of the properties of the CEM is included in table 2.1.

In order to allow for a more precise determination of the position and lateral energy distribution of electromagnetic showers, a proportional strip and wire chamber known as the CES was embedded close to the depth of maximum electromagnetic energy deposition (approximately 6 radiation lengths). Cathode strips running in the azimuthal direction provide z information whereas anode wires running in the z direction provide measurements in the $r - \phi$ plane. In addition to providing valuable information for electron identification

through a measurement of the lateral shower profile, the CES improves the spatial resolution of the central electromagnetic calorimeter. The position resolution for 50 GeV electrons is approximately 2 mm. Another tool for electron/hadron separation, known as the central preradiator or CPR, was placed between the solenoid and the CEM. The CPR is a set of proportional tubes. Since electrons are more likely to begin to generate a shower in the solenoid than hadrons, they will often result in several energy depositions in the CPR, whereas hadrons tend to leave little or no energy in this preradiating system.

The CHA has a thickness of 4.7 absorption lengths. Financial and installation constraints dictated that the amount of absorbing material in the calorimeter be limited to 80 cm of steel at normal incidence. This absorption length limits the energy resolution of the calorimeter and makes muon identification in the outer chambers more challenging, due to the fact that shower containment is sometimes incomplete. For example, the calorimeter manages only 95% average energy containment for 50 GeV pions. This necessitated the central muon upgrade (CMP), that is discussed in section 2.5.

Also, particles produced in the η regime between 0.6 and 1.1 do not pass through all the layers of the CHA. This motivates the placement of the Endwall Hadron calorimeter (WHA) in this high $|\eta|$ regime to provide fuller containment of hadronic showers. Properties of the central and endwall hadronic calorimeter are given in table 2.1.

The energy resolution for the CHA has been measured with isolated pions to be

$$(\sigma/E)^2 = (0.50/\sqrt{E_T})^2 + (0.03)^2 \ , \tag{2.2}$$

whereas for the WHA, we measure

$$(\sigma/E)^2 = (0.75/\sqrt{E_T})^2 + (0.04)^2 \ . \tag{2.3}$$

2.3.2 Plug and Forward Calorimeters

The importance of jet energy measurements in reconstructing top quark kinematics makes CDF's calorimetry essential in this analysis. In particular, we rely heavily on the measurements of the vector sum of the transverse energy in the event (known as missing E_T or

$\not\!\!E_T$), a quantity whose measurement relies on all three subsystems of the hadronic calorimeter. Also, due to the large number of energetic jets expected in $t\bar{t}$ candidate events, jet reconstruction out to η values of 2.0 or above is essential in order to a maintain a reasonable selection efficiency. These facts speak of the importance of the forward and plug calorimeters in this analysis.

The plug and forward calorimeters are divided into electromagnetic and hadronic subsystems. They are, like their central counterparts, sampling calorimeters. However, they use gas, as opposed to scintillator as their active medium. The active medium consists of layers of proportional tubes, using a 50%-50% mixture of argon and ethane gas. Each tube consists of a wire and the anode inside a resistive plastic tube. The copper pads which make up the anode define the tower segmentation of the calorimeter. The energy resolution of the PEM, as determined by testbeam electrons, is

$$(\sigma/E)^2 = (0.22/\sqrt{E_T})^2 + (0.02)^2 \ , \tag{2.4}$$

whereas the energy resolution for the PHA is

$$(\sigma/E)^2 = (0.90/\sqrt{E_T})^2 + (0.04)^2 \ . \tag{2.5}$$

In the forward region, the FEM's energy resolution can be parameterized by

$$(\sigma/E)^2 = (0.26/\sqrt{E_T})^2 + (0.02)^2 \ , \tag{2.6}$$

whereas the energy resolution for the FHA is

$$(\sigma/E)^2 = (1.37/\sqrt{E_T})^2 + (0.04)^2 \ . \tag{2.7}$$

Other properties of the plug and forward calorimeters are given in table 2.2.

2.4 Tracking Systems

Three complimentary subsystems, immersed in a 1.4 T magnetic field, comprise the charge particle tracking system at CDF. The Silicon Vertex detector (SVX) lies closest to the beampipe and is designed to give precise position information in the $r - \phi$ plane. This

Table 2.2: Summary of the properties of the plug and forward calorimeter subsystems. The thicknesses are given in terms of radiation lengths for the electromagnetic subsystems and nuclear interaction lengths for the hadronic subsystems.

	Plug EM	Plug Hadron	Forward EM	Forward Hadron
Coverage ($\|\eta\|$)	1.1-2.4	1.3-2.4	2.2-2.4	2.3-2.4
Tower size ($\delta\eta \times \delta\phi$)	$0.09 \times 5^\circ$	$0.09 \times 5^\circ$	$0.1 \times 5^\circ$	$0.1 \times 5^\circ$
Number of Layers	34	20	30	27
Tube Size	$0.7 \times 0.7\text{cm}^2$	$1.4 \times 0.8\text{cm}^2$	$1.0 \times 0.7\text{cm}^2$	$1.5 \times 1.0\text{cm}^2$
Absorber	Pb	Fe	94% PB, 4% Sb	Fe
Thickness	19 X_0	5.7 λ_I	25 X_0	7.7 λ_I

can be used, for example, to identify the secondary vertices arising from the decay of a B hadron. The VTX, comprised of 8 time projection chambers, lies directly outside the SVX. The VTX's primary role is to measure the z- coordinate of the primary vertex in the event. The Central Tracking Chamber, or CTC, is a large drift chamber that surrounds the VTX.

2.4.1 The Silicon Vertex Detector

Installed in CDF in 1992, the SVX was the first detector of it's kind to be successfully operated in a hadron collider environment. In 1993, a version of the SVX with improved radiation resistance and lower improved signal to noise characteristics, known as the SVX$'$ was installed. The SVX consists of two barrels that are aligned along the beampipe. In the $z = 0$, plane, there exists a 2.15 cm gap between the two subdetectors. Each of the barrels is in turn composed of 12 azimuthal wedges and four concentric layers of silicon microstrip detectors. The four layers of the SVX are positioned at radii of 3.0 ,4.3, 5.7 and 7.9 cm. The innermost layer of the SVX$'$ is positioned at 2.9 cm, whereas the outer three layers occupy the same radii as the SVX. Approximately, 40% of the primary interaction vertices

Figure 2.4: A diagram of an SVX barrel. The SVX is composed of two such barrels, longitudinally aligned along the beamline.

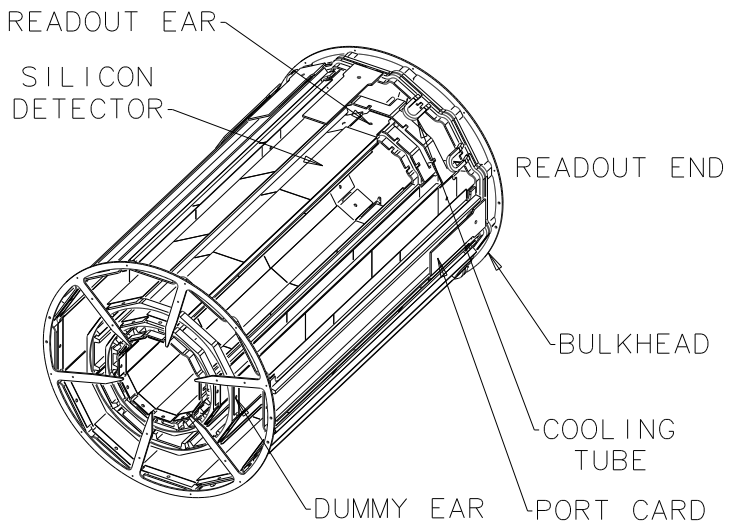

lie outside the fiducial acceptance of the SVX[2], which has an active length in z of 51.1 cm.

The azimuthal wedges of the SVX are known as "ladders". Each ladder is composed of 3 silicon strip detectors aligned along the beamline. The strip separation, or "pitch", of the innermost three layers is 60 μm, whereas the outermost layer has a 55 μm pitch. This results in an approximate single-hit resolution of 13 μm, and the hit efficiency per layer is 96%. In order to ensure complete azimuthal coverage, adjacent ladders overlap slightly. This is ensured by rotating each of the ladders by 3° from their nominal positions.

The SVX possesses a total of 96 ladders. Each of these ladders is read out by a series of readout chips, with each chip being responsible for 128 strips. The readout of the 46080 channels of the SVX is performed in parallel and in sparse mode. In other words, only the channels that register a hit are read out in a given event. Even so, reading out the SVX takes 2 ms, an enormous amount of time in a hadron collider environment. In Table 2.3,

[2]At this point, we abandon the distinction between the SVX and SVX′, referring to both detectors as "SVX" and only making the distinction where relevant.

Table 2.3: Summary of some selected properties of CDF tracking subsystems. The p_T resolution is quoted for CTC only and then for combined CTC-SVX charged particle reconstruction.

	CTC	VTX	SVX
Coverage ($\|\eta\|$)	0-1.5	0-3.25	0-1.2
Inner Radii (cm)	30.9	8	2.7
Outer Radii (cm)	132.0	22.0	7.9
Length(cm)	320	280	26
Pitch	10 mm	6.3 mm	60 or 55 μm
Layers	60 axial, 24 stereo	24	4
Spatial Resolution (μm)	200($r-\phi$), 4000 ($r-z$)	$200-500r-z$	15 ($r-\phi$)
$\delta p_T/p_T$	$0.002 \times p_T$ (CTC Only)	NA	$0.001 \times p_T$ (CTC + SVX)
Thickness	$0.015X_0$	$0.0045X_0$	$0.035X_0$

we summarize the properties of the SVX.

2.4.2 The Vertex Time Projection Chamber

A vertex time projection drift chamber, the VTX, lies outside the SVX. The VTX allows for relatively precise reconstruction of the z vertex of an event, doing so with an approximate resolution of 2 mm. This resolution is a function of how many charged particle tracks there are originating from a given primary interaction point. The VTX is designed to reconstruct all of the collision vertices in events possessing multiple interactions. A design goal for the VTX was to make it as thin as possible in radiation lengths, in order to not degrade CTC momentum reconstruction.

The VTX consists of 8 octagonal VTPC modules, each of which is equipped with a central high voltage grid that divides it into two 15.25 cm long drift regions. This drift length is chosen such that the drift time, when employing a 50/50 mixture of argon and

ethane is less than the 3.5 μs bunch crossing time. The free electrons created by charged particle ionization in the gas drift away from the central grid towards one of two proportional chamber endcaps. Each endcap is divided into octants, with 24 sense wires and 24 cathode sense pads. The z coordinate of a given track is determined by the drift time and the r information based on the radial location of the sense wire. The drift field is 256 V/cm and the gas pressure is one atmosphere. Selected characteristics of the VTX are given in table 2.3.

2.4.3 The Central Tracking Chamber

The central tracking chamber, or CTC, is the only tracking device at CDF that can perform three dimensional momentum and position measurements. Measuring 1.3 m in outer radius and 3.2 m in length, the CTC is composed of 84 layers of wires grouped into 9 so-called "superlayers". Five of these syperlayers consist of 12 layers of axial sense wires and the remaining four are stereo superlayers tilted at 3° relative to the beam direction. In Fig. 2.5, we depict the CTC endplate, where the 45° tilt of the superlayers with respect to the radial direction is evident. This tilt compensates for the 45° Lorentz angle which defines the direction of electron drift in the superposition of crossed electric and magnetic fields. The field wires of the CTC generate a 1350 V/cm electric field. The maximum drift time in the argon(49.6%)-ethane(49.6%)-alcohol(0.8%) gas, is approximately 800 ns, significantly less than the 3.5μs bunch crossing time at the Tevatron.

The stereo superlayers provide tracking information in the $r-z$ plane, with a resolution of approximately 4 mm. However, the majority of the information used to reconstruct charged particle trajectories comes from the axial superlayers, resulting in a transverse momentum resolution that can be parameterized by $\delta p_T/p_T = 0.002 \times p_T$. In addition to this, if information is available from the SVX and is used to assist in fitting a helix to the measured track parameters, the transverse momentum resolution improves to

$$\delta p_T/p_T = 0.001 \times p_T \ . \tag{2.8}$$

Figure 2.5: A transverse view of a CTC endplate. The tilt of the wire planes relative to the radial direction is evident.

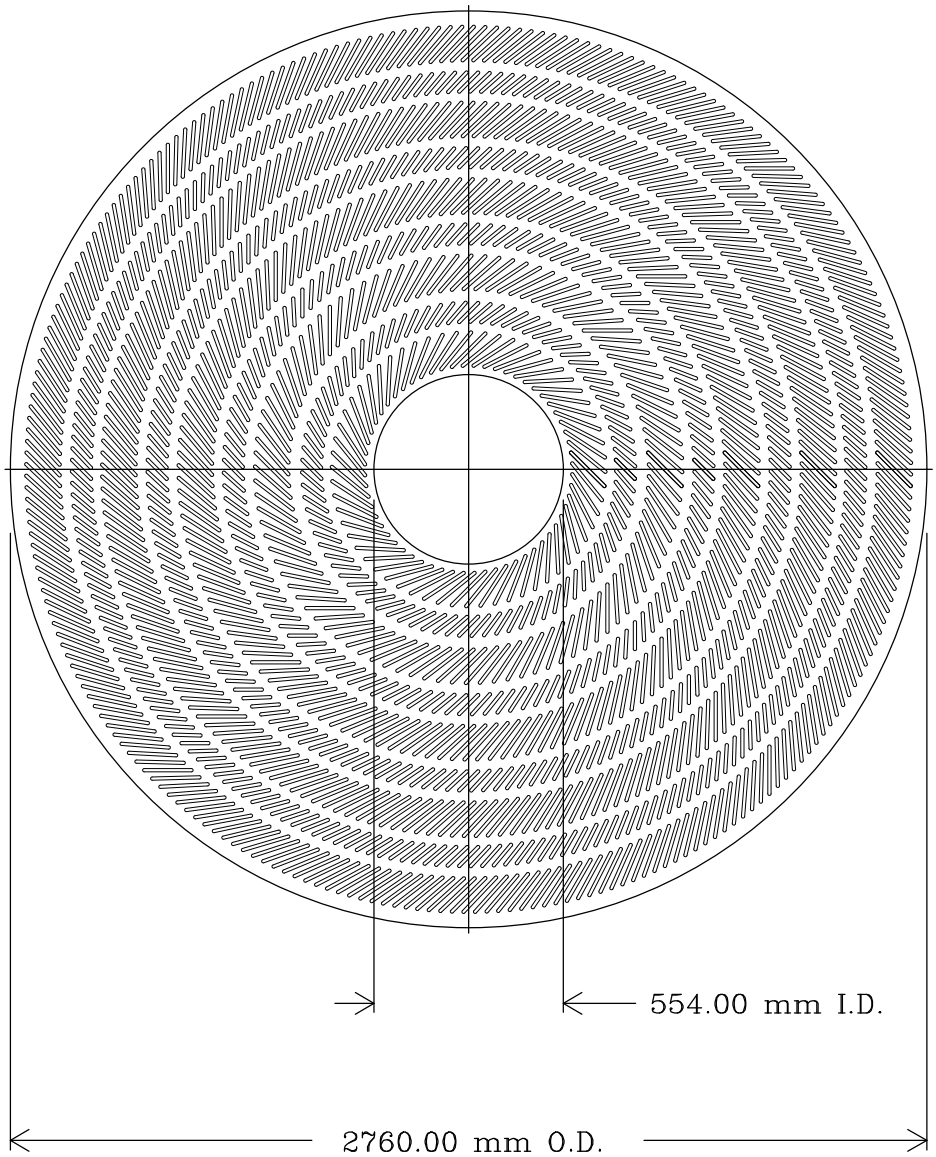

2.5 The Muon Chambers

Lepton identification is an important component of hadron collider physics, as it allows access to key physics processes. Thus, CDF is equipped with drift tube arrays outside it's calorimeters that allow for muon identification and momentum measurement. These detector subsystems exploit the radiative properties of muons in matter that allow muons to penetrate through much more absorbing material than most other ionizing particles. Thus, the CDF calorimeters serve to filter out the electrons and hadrons. Three separate muon detectors were used for this analysis: The first is known as the central muon detector, or CMU, and provides muon coverage in the polar angle regime $|\eta| < 0.6$, outside this detector lies the central muon upgrade, or CMP, which provides muon coverage in a similar angular regime. Finally the central muon extension, or CMX, provides muon coverage in the region $0.6 < |\eta| < 1.0$. The angular coverage of these detectors is depicted in Fig. 2.6.

The principle of operation of all three muon subsystems is similar. They consist of several layers of single-wire drift cells. The CMX and CMP also include scintillator planes that allow for precise timing information, particularly useful in the trigger system.

The location of the CMU system is depicted in Fig. 2.7. It resides just outside the CHA, at a distance of 3.5 m from the beamline. The CMU is subdivided into 15° "wedges", each of which contains three modules. As shown in Fig. 2.6, the azimuthal coverage of the CMU is not complete. This is in part due to the fact that each module, consisting of a 4 by 4 array of drift cells, subtends only 4.2° in azimuth. A CMU module is depicted in Fig. 2.8. At the center of each cell is a 50μm sense wire held at a potential of 3150 V relative to the drift tube. The drift gas is argon/ethane bubbled through alcohol. This results in a maximum drift time of approximately 700 ns. The outer two layers of tubes are displaced by approximately 2 mm relative to the first two, in order to resolve the left-right ambiguity arising from the fact that a priori one doesn't know which side of the sense wire the particle passed by.

Since only 5.4 interaction lengths of material lie between the interaction point and the CMU, approximately 1 in 220 high-energy hadrons pass through unchecked, creating an

Figure 2.6: Coverage of the central muon subsystems in $|\eta|$ and ϕ.

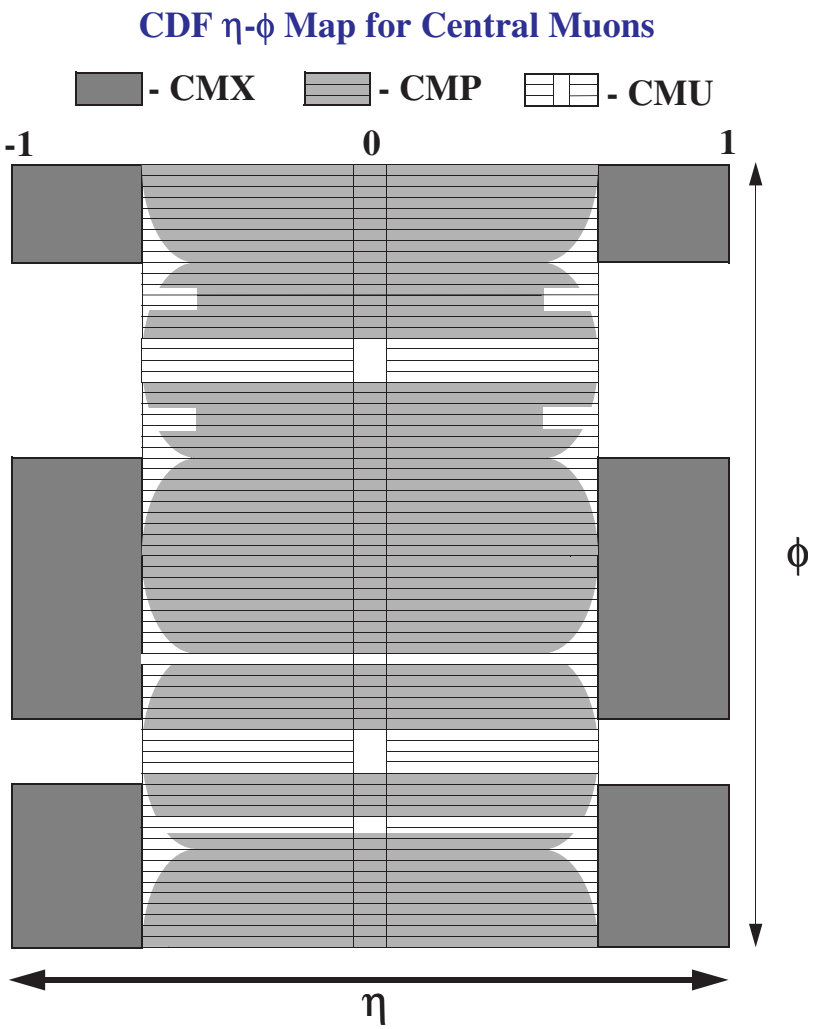

irreducible background in a candidate muon sample. This is a severe complication for muon identification. With this in mind, an additional 0.6 m of steel was added behind the CMU in order to provide another level of hadron filtration before the next muon detector, the CMP. The flux return yoke of the solenoid provides the additional material on the top and bottom of the detector whereas retractable slabs of steel are used on the sides of the detector. The CMP subdetector consists of four layers of single wire drift tubes. However, unlike the tubes in the CMU these tubes are staggered in order to avoid the gaps in coverage that would otherwise occur. The drift cells are rectangular aluminum tubes 25.4 mm high and

Figure 2.7: The location of of a central muon (CMU) wedge in both the azimuthal (left picture) and polar (right picture) views.

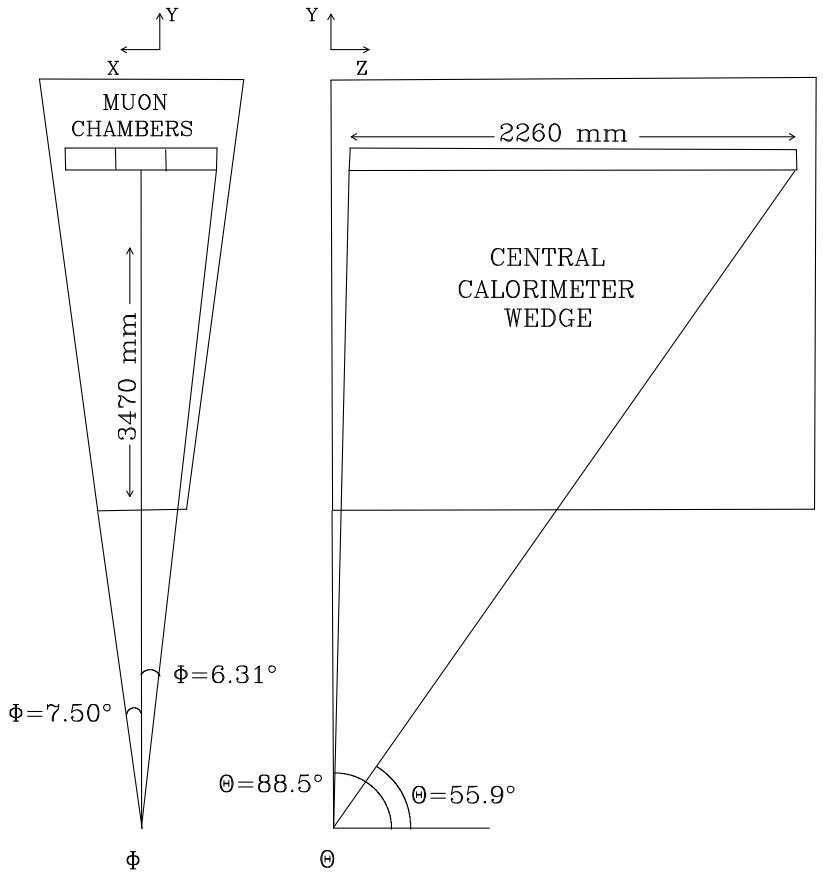

152.4 mm wide. The maximum drift time in the CMP tubes is 1.4 μs.

In order to extend the coverage of the muon systems beyond $|\eta| = 0.6$, CDF includes an extended muon system, the central muon extension, or CMX. The CMX provides muon detection for the polar angle regime defined by the range $0.65 < |\eta| < 1.0$. The azimuthal coverage of the CMX is, however, far from complete. Due to interferences with the main ring bypass beampipe and the floor of the collision hall the gaps in CMX coverage depicted in Fig. 2.6 occur. The drift tubes, aside from being shorter in length, are identical to those used in the CMP. The CMX is organized into four stacks, each of which are composed of 8 modules. A module is in turn comprised of 8 half-cell staggered layers of 6 tubes each.

Figure 2.8: Diagram of a central muon module. A muon track is depicted, with two measured drift times (t_2 and t_4) shown. These times can give a crude measurement of the muon momentum that can then be employed in a low level trigger.

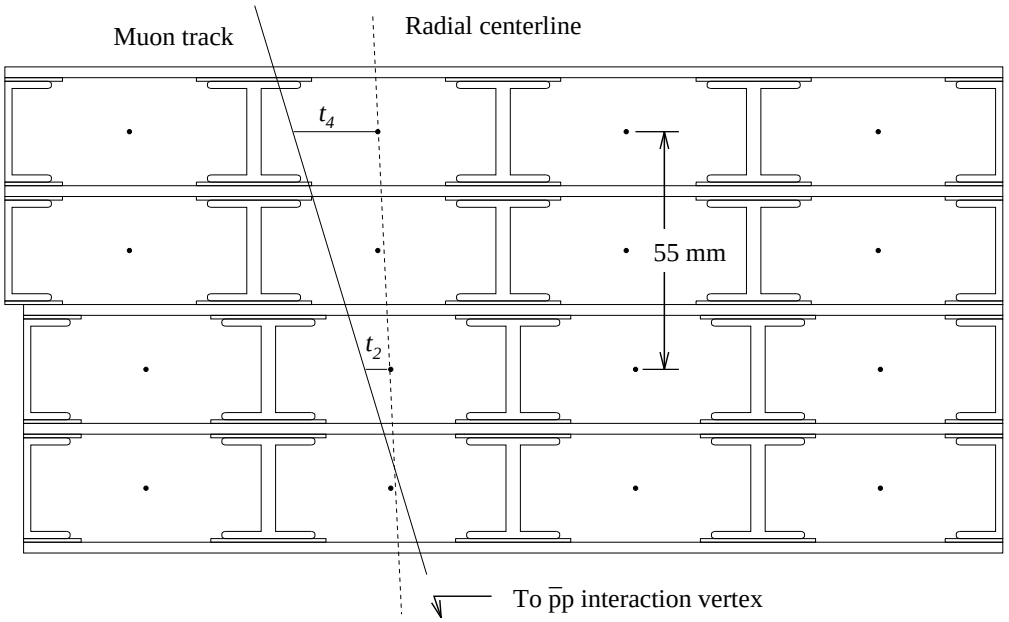

Furthermore, the CMX is equipped with an array of scintillation counters on both the inner and outer sides of each module. The requirement that the inner and outer scintillation counters produce signals that are consistent with the $p\bar{p}$ crossing time to within a few nanoseconds can be used by the trigger system to reject background hits in the CMX arising from particles not associated with the primary interaction.

2.6 The Beam Beam Counters

The total integrated luminosity delivered to CDF is calculated using the soft interactions between two partons, events which constitute the vast majority of the $p\bar{p}$ interactions at the Tevatron. These events, known as minimum bias data, are characterized by a spray of low transverse momentum particles that are produced at the interaction point with trajectories almost coincident with the beamline. CDF counts these minimum bias events with a system of scintillators known as the Beam Beam Counters (BBC). The BBC cover the region

$3.2 < |\eta| < 5.9$ and have a timing resolution of better than 200 ps. In order to calculate the integrated luminosity, CDF first counts coincident hits in the forward and backward BBC, and uses this to calculate the instantaneous luminosity. This is then integrated over time in order to calculate the integrated luminosity. The total integrated luminosity of our data sample was measured to be 106 pb^{-1}.

2.7 Trigger Systems

At CDF, the amount of data recorded in each interaction is roughly 165 kB. Such an event size could only be written out for storage on magnetic tape at a rate of approximately 10 Hz, whereas collisions occur at a rate $>$ 300 kHz. In order to accommodate the necessary rejection rate (approximately 30000:1), a trigger system is clearly necessary. The CDF trigger consists of 3 levels, each of which imposed a logical 'OR' of programmable selection criteria that is designed to reduce the data rate to which the next-highest level of the trigger is exposed. The first two levels of the trigger are composed exclusively of dedicated processors, whereas level 3 is implemented in by a general software algorithm running on a cluster of commercial processors.

Since the objective of this analysis is the measurement of the top quark p_T distribution in the lepton + jets final state, triggers identifying high-p_T leptons are the most obvious way to obtain our data sample. Indeed, these were the principle triggers used to acquire the data used in this analysis. In addition to this, in Run IB, a missing-E_T trigger was employed. Such a trigger allows for identification of events for which the high-p_T lepton triggers were not efficient.

The level one trigger system operates without deadtime, that is, it takes less than 3.5 μs to make it's trigger decision. The level one trigger reduces the event rate by a factor of approximately 300. The high-p_T lepton trigger was based on localized energy depositions in the calorimeters or hits in the muon chambers. The calorimeter level one trigger used in our analysis required a pair of adjacent towers (also known as a "trigger tower") in the electromagnetic calorimeter to have energy over a given threshold. In order to select events

with high-p_T muons, a second trigger requiring a pair of hits in two radially-coincident muon drift tubes was also employed.

At level 2, where the input event rate is approximately 1 kHz, more sophisticated calorimetry information along with tracking information becomes available. If the level one trigger fires, then the next five beam crossings are ignored and the level two trigger is given 20 μs to make its decision. This results in a deadtime of several percent. The rate of selected events by the level 2 trigger varies between 20 and 35 Hz.

At level 2, the calorimetry triggers are expanded to include "seed" and "shoulder" thresholds. In effect, if a given trigger tower measures an energy deposition that exceeds the "seed" threshold, adjacent trigger towers that exceed a "shoulder" threshold can be iteratively added to form a "cluster". In addition to this, a fast hardware track processor, known as the central fast tracker, or CFT, uses CTC hits to reconstruct high-momentum tracks in the $r-\phi$ plane. The CFT operates by looking at the axial superlayers of the CTC for "roads", or hit patterns, that match templates that are included in a look-up table. The resulting transverse momentum resolution is $\delta p_T/p_T \sim 0.035 \times p_T$. Since track segment information is also available from the central muon chambers, tracks found by the CFT can be matched to reconstructed tracks in the muon chambers (also known as "stubs") or clusters in the CEM. Thus, at level two, one begins to organize the data into categories that include various "physics objects", such as electron or muon candidates.

The level 3 trigger is a flexible software-based system that can reconstruct up to 64 events in parallel. The level 3 trigger system underwent significant changes between Run IA and IB. In what follows, we describe its IB configuration.

The level three trigger runs on a "farm" of 64 Silicon Graphics processors. The software used is a simplified version of the offline software. For example, since three dimensional track reconstruction constitutes the largest contribution to the level 3 processing time, only the simpler of CDF's two track-reconstruction algorithms is used. The output rate of CDF's level 3 trigger is between 3 and 5 Hz for Run IA and about 8 Hz for Run IB.

2.8 Offline Reconstruction

Events that pass all three levels of the trigger system are subsequently processed with the full CDF offline software package. The goal of this code is to identify all candidate jets, electrons and muons, and to measure the transverse energy of energetic neutrinos.

Jets are reconstructed using an E_T-weighted cone algorithm using a cone radius of $\Delta R = \sqrt{\Delta\eta^2 + \Delta\phi^2} = 0.4$. The transverse energy of a jet is defined as the sum of the energy deposited in the calorimeter towers within the cone, multiplied by $\sin\theta$ where θ is the polar angle of the E_T weighted centroid of the cluster. The cluster begins with a "seed tower" having transverse energy greater than 3 GeV. In order to be added to the cluster, neighboring towers must have a minimum energy deposition of 1 GeV. The jet transverse energy, calculated in this way, is referred to as the "raw" jet energy, due to the fact that there are several detector effects that remain to be accounted for. The corrections designed to correct for these effects are described in section 4.1.

In order to identify electrons, electromagnetic clusters are formed in the CEM using an algorithm similar to the one described above. An electron cluster also begins with a seed tower possessing at least 3 GeV. However neighboring towers with energy greater than only 0.1 GeV are added. Muon candidates are formed by matching CTC tracks to tracks in the muon detectors. Electron and muon candidate selection will be described in detail in the next chapter.

Chapter 3

Event Selection

The data sample used in this analysis is based upon the identification of the $t\bar{t} \to \ell\nu q\bar{q}b\bar{b}X$ channel, referred to as the "lepton + jets" final state. Our selection criteria will thus be designed to identify events possessing a high-p_T electron or muon in the final state, significant $\not\!\!E_T$, and four or more jets. We shall use identical selection criteria on both data events and "Monte Carlo" events. Monte Carlo events are simulated data samples that are used to measured the acceptance and resolution of the detector, including the effect of selection criteria.

With a production cross section close to 5 pb, $t\bar{t}$ production is the rarest process ever observed in a hadron-collider environment. We begin our search for top quark events by requiring the presence of a high-p_T electron or muon candidate in the event. We subsequently impose a set of selection criteria designed to select the subset of these events where the aforementioned high-p_T lepton originates from the leptonic decay of a W-boson. This sample is known as the "inclusive W sample". Finally, we impose an even more stringent set of selection criteria to select the events that are used to reconstruct the corrected p_T distribution of $t\bar{t}$ events at the Tevatron.

Table 3.1: Selection requirements applied to electron candidates.

$E_T > 20\ GeV$
$E/P < 1.8$
$E_{had}/E_{em} < 0.05$
$L_{shr} < 0.2$
Track/Strip Matching
$\lvert z_{electron} - z_{vertex} \rvert < 5$ cm
$\lvert z_{vertex} \rvert < 60$ cm
Fiducial Requirements

3.1 Inclusive Electron Sample

As noted in Section 2.8, electron candidates are formed by matching CEM clusters to charged tracks. The process begins with the level 1 trigger, where the trigger accepts all events possessing $E_T > 8$ GeV. At level 2, where tracking information becomes available, the trigger requires that a CEM cluster with $E_T > 16$ GeV must match a CFT track with $p_T > 12$ GeV. Due to the fact that this level 2 trigger is only about 90% efficient for fiducial high-p_T electrons[16], an additional level 2 trigger based on $\not\!\!E_T$ was added. This trigger requires a CEM cluster with $E_T > 16$ GeV along with 20 GeV of raw $\not\!\!E_T$.

In all cases, since the cuts applied at level 3 are subsets of the cuts that are applied offline, we choose only to describe the latter. We describe these selection in some detail below.

First, the E_T requirement is raised to 20 GeV. Secondly, we require a rough correspondence between the CTC-measured momentum of a particle (P) and its CEM-measured energy (E) by imposing the requirement that $E/P < 1.8$. Since electromagnetic showers should deposit almost all of their energy in the CEM, we then demand that the ratio of electromagnetic to hadronic energy in the event satisfy the criteria $E_{had}/E_{em} < 0.05$. The strip chambers embedded near the shower maximum of the CEM also prove useful here by

allowing a more precise reconstruction of the shower location by fitting the lateral energy profile of the electromagnetic cluster. Correspondence between this measurement and the location predicted by the charged track associated with the electron candidate is demanded in both the $r-\phi$ direction ($\Delta x < 1.5$ cm) and in the direction of the beamline($\Delta z < 3.0$ cm). Furthermore, a χ^2 test between the measured shower profile and the expected shape (as determined by testbeam electrons) is performed. Furthermore, an additional compatibility test between the energy deposition in the calorimeter towers that comprise the electromagnetic cluster and the expected shape is performed. This is quantified by using the variable L_{shr}, defined as

$$L_{shr} \equiv 0.14 \sum_i \frac{E_i^{tower} - E_i^{testbeam}}{(\sqrt{0.14\sqrt{E}})^2 + \sigma^2_{testbeam}} , \tag{3.1}$$

where E_i^{tower} is the observed energy in tower i, $E_i^{testbeam}$ is the predicted energy in tower i, based on studies of testbeam electrons, and $\sigma_{testbeam}$ is the uncertainty on the expected value. The sum over i runs over all adjacent towers associated with the electron candidate. The distance between the interaction vertex and the reconstructed track in the z direction must be less than 5 cm. In addition to this, this vertex must lie within 60 cm of the center of the detector. Finally, fiducial criteria remove those electrons candidates whose corresponding electromagnetic clusters lie close to the boundaries between detector components in order to ensure that electron energies are well-measured in the CDF detector. In table 3.1, we summarize the selection criteria that are applied to electron candidates.

Employing studies of Z-boson decay, the efficiency of these selection criteria has been measured to be $81.9 \pm 0.7\%$. This is done by using a set of tight selection criteria in order to find one electron originating from this decay, while the selection criteria listed above are applied to the secondary lepton. The invariant mass of the two electron candidates is required to be between 75 and 105 GeV.

At this point in the event selection, many of the electron candidates in our data sample do not originate from W decay. An important source of background that can be easily dealt with is the so-called "conversion" electrons, electron candidates that originate from photon conversions in matter or Dalitz decays. Before the application of selection criteria designed

to remove them, these electrons compose approximately 35% of the inclusive electron sample. These electrons can be characterized by having an oppositely charged track whose trajectory extrapolates backwards to an intersection point with the electron track. These tracks, when paired together, are required to have an invariant mass less than 0.5 GeV/c^2. Furthermore, another characteristic of photon conversions is that they are more likely to occur within regions of the detector where there is large mass density. For this reason, conversion candidates are required to have less than 20% of the hits in the VTX than what would be expected for an electron.

3.1.1 Inclusive Muon Sample

We begin our definition of a muon candidate event by requiring that a charged track found by CDF's online track processor, the CFT, possesses $p_T > 12$ GeV/c and point to within 5° of an associated muon "stub", or collection of coincident hits in the outer muon chambers. We then further subdivide this sample based on the muon subsystem(s) in which the muon candidate is detected. Muon candidates with associated hits in both the CMU and CMP chambers are known as CMUP muons, whereas muon candidates with associated hits in only one of the detectors are known as either CMU,CMP or CMX-only muons, as appropriate.

Backgrounds for muon candidates arise predominantly from hadrons that have penetrated, or "punched through" the hadronic calorimetry and cosmic rays. Due to high background rates, and the fact that some of the muon triggers generate rates that are unacceptably large, the trigger system for muon candidates is more complicated than the one for electron candidates. One difference is that for some muon triggers, we employ a procedure known as "prescaling". Prescaling involves selecting only a subset of the events passing a given trigger. If a trigger is prescaled by a factor N, then only one out of every N events passing the trigger in question will be added to the data sample. Furthermore, for the triggers in which we are interested here, the number N changes as a function of the instantaneous luminosity. This even more convoluted procedure is known as "dynamic prescaling". The level 2 muon triggers are listed in table 3.2. Each line in this table corresponds to a different trigger.

Table 3.2: The level 2 triggers for muon candidates. Each line in this table corresponds to a separate trigger. Prescaled triggers are indicated with asterixes.

CMU-only muon candidates
$\not\!\!E_T > 35$ GeV and two jets having $E_T > 3$ GeV
CFT track with $p_T > 12$ GeV/c ,matched to CMU stub*
As above, but with an additional jet having $E_T > 15$ GeV
CMUP Muons
$\not\!\!E_T > 35$ GeV and two jets with $E_T > 3$ GeV
CFT track with $p_T > 12$ GeV/c ,matched to CMU and CMP stubs
As above, but with an additional jet having $E_T > 15$ GeV
CMP-only Muons
$\not\!\!E_T > 35$ GeV and two jets having $E_T > 3$ GeV
CMX Muons
$\not\!\!E_T > 35$ GeV and two jets having $E_T > 3$ GeV
CFT track with $p_T > 12$ GeV/c ,matched to CMU stub*
As above, but with an additional jet having $E_T > 15$ GeV*

At Level 3, full offline reconstruction of muon stubs and CTC tracking is available. The distance between the extrapolation of the CTC track associated with the muon candidate and the muon stub ($\Delta x = r\Delta\phi$) is required to be less than 10 cm for CMU-only or CMUP muons, 25 cm for CMX muons, and 40 cm for CMP-only muons.

The muon candidates selected by the trigger system are then subjected to a suite of offline selection criteria, which are listed in Table 3.3. We begin by demanding that the muon candidate have p_T greater than 20 GeV/c. A set of criteria designed to ensure that the muon stub should be associated with the same charged track observed in the CTC, is then implemented. This is done by comparing the position of the extrapolated CTC track with the location of the reconstructed track in the muon chambers. The less stringent matching requirements for CMP-only and CMX-only muon candidates are due to the fact that muons

Table 3.3: Selection requirements applied to muon candidates.

$p_T > 20$ GeV/c
Track-Stub Matching:
$\lvert\Delta x\rvert_{CMU} < 2.0$ cm or $\lvert\Delta x\rvert_{CMP} < 5.0$ cm or $\lvert\Delta x\rvert_{CMU} < 5.0$ cm
$E_{em} < 2.0$ GeV
$E_{had} < 6.0$ GeV
Impact Parameter < 3 mm
$\lvert z_{muon} - z_{vertex}\rvert < 5$ cm
$\lvert z_{vertex}\rvert < 60$ cm

reaching the CMP or CMX traverse more material, and are thus more prone to deflection due to multiple scattering, than those muons detected in the CMU. In order to reject punch-through hadrons, the energy deposition in the calorimeters is required to be consistent with what would be expected from a minimum-ionizing particle. Thus, we demand that the energy deposition in the electromagnetic(hadronic) calorimeter tower associated with the muon be less that 2(6) GeV. Furthermore, tracks originating from cosmic rays are then rejected by requiring that the muon candidate reconstructed trajectory extrapolated backward to within 3 mm (in $r - \phi$) of the beamline, and by requiring that at $r = 0$ it is within 5 cm (in z) of the measured VTX event vertex.

The efficiencies of these selection criteria are once again measured using Z-boson decays. The combined efficiency of these selection criteria is measured to be $94.1 \pm 1\%$ for CMX muons, $90 \pm 2\%$ for CMU-only muons, $88 \pm 2\%$ for CMP-only muons and $93.6 \pm 0.7\%$ for CMUP muons[43].

3.1.2 W Sample

We now select the "inclusive W sample", a sample of event containing central high-p_T leptons, significant $\not\!\!E_T$. We describe in this section a set of selection criteria that are designed to separate events arising from W-boson decay from those candidate events arising

from other sources. Other sources of high-p_T leptons include semileptonic decays of heavy flavor and Z-boson decays.

Compared to leptons originating from, for example, semileptonic B hadron decays, we expect leptons originating from W decays to be relatively well separated from energy depositions in the calorimeter that arise from other particles in the event. In order to quantify this separation, we define a quantity known as "isolation". For electrons, isolation is defined by the relation

$$I^e \equiv \frac{E_T^{cone} - E_T^e}{E_T^e} \ , \tag{3.2}$$

where E_T^{cone} is the calorimeter energy contained in a cone of radius $\Delta R = 0.4$ centered on the electron cluster centroid, and E_T^e is the calorimeter energy of the electron. For muons, we define a similar quantity. This quantity is defined by

$$I^\mu \equiv \frac{E_T^{cone} - E_T^{tower}}{p_T^\mu} \ , \tag{3.3}$$

where E_T^{tower} is the amount of energy found in the tower intersected by the muon candidate, p_T^μ is the transverse momentum of the muon track, as reconstructed by the CDF tracking system. Events included in the inclusive W sample are required to have a primary lepton with isolation less than 0.1.

Another signature of a leptonic W decay is the $\not\!\!E_T$ associated with the undetected production of an energetic neutrino. An estimate of the $\not\!\!E_T$ in an event can be obtained by computing the inverse vector sum of the transverse energy measured in all calorimeter towers. If the primary lepton in the event is a muon, a more precise estimate of this quantity is obtained by including the muon p_T in the sum and subtracting the energy deposited in calorimeter towers associated with the muon. Corrections are also made for other minimum-ionizing tracks in the event, if they posses transverse momentum in excess of 10 GeV/c and pass matching requirements with a muon stub. Only events with $\not\!\!E_T > 20$ GeV, as determined by this calculation, are considered as possible W candidates. The efficiency of this selection has been estimated to be 83% for $t\bar{t}$ events.

Events consistent with originating from the decay of a Z-boson are also removed. A Z-boson candidate is defined by requiring two oppositely-charged, electrons or muons in

Table 3.4: The number of events remaining after each stage of the inclusive W selection. The lepton selection criteria are presented in Tables 3.1 and 3.3 for electrons and muons respectively.

Selection Criteria	Muons	Electrons
Lepton Selection Criteria	87892	121123
Bad Run Removal	84251	115699
Isolation < 0.1	51102	76791
$\not\!\!E_T > 20$ GeV	38602	57675

the event, each having $p_T > 20$ GeV/c, and the pair having an invariant mass in the region between 75 and 105 GeV/c^2. In order to remove radiative Z decays, the invariant mass of the lepton pair with any high-p_T photon candidate in the event must also lie outside this mass window. Furthermore, some periods of operation of the CDF detector are known to have been plagued by detector problems, such as excessive noise in the muon chambers. Events collected during these periods, which are known as "bad runs", are are removed from the sample. The number of event removed from the sample for this reason is small, and is shown in Table 3.4. Events passing CDF's dilepton selection criteria[42] are also removed. The dilepton analysis also begins with the inclusive lepton samples described above, but then searches for an additional lepton candidate of opposite charge having $E_T(p_T)$ greater than 20 GeV. Additional selection criteria include $\not\!\!E_T > 25$ GeV and the requirement of two jets with $E_T > 20$ GeV.

The number of events remaining after each step of the selection criteria described above is listed in Table 3.4.

3.1.3 Kinematic Selection Criteria

We now apply a set of selection criteria designed to increase the signal to noise ratio in our event sample. We first apply a set of jet cuts, to obtain the "W + 3 jet" sample. This involves requiring the presence of at least three jets in the event having $E_T > 15$ GeV and

$|\eta| < 2.0$. After this selection criteria is applied, only 324 events remain in our dataset. This data sample was used to measure the $t\bar{t}$ production cross section[44]. We then form the "W + 3.5 jet" sample by requiring the presence of a fourth jet in the event satisfying the selection requirements $E_T > 8$ GeV and $|\eta| < 2.4$. This reduces the sample size to 163 events. Due to the fact that we now have four jets with which to constrain the kinematics of the $t\bar{t}$ decay, we can now employ the kinematic fitter described in section 4.2 on this sample of events.

3.2 Monte Carlo Simulation of Physics Processes

This section describes the Monte Carlo calculations used to simulate the physics processes of interest. Complete simulation of the processes allows for an understanding of various systematic effects, a complete study of the kinematic biases introduced by our reconstruction algorithm, and a methodology for estimating the background contribution to our dataset. This analysis uses a Monte Carlo event generator and a simulation of the CDF detector in order to estimate these effects. The simulation of an event consists of two stages. This first is finding an appropriate simulation of the physics process of interest (known as "event generation"), and the second is a simulation of the interaction of the resulting particles with the detector (a procedure known as "detector simulation").

3.2.1 Simulation of Signal Events

The principle of event generation is much simpler than its implementation. All of the event generators considered here begin with a tree-level calculation of the matrix element of the QCD or electroweak process of interest, and then fold the resulting matrix element with an appropriate parton distribution function. At the time at which the Run I top analyses began, the MRSD0′ partition functions[45] were chosen on the basis of their ability to reproduce CDF's W asymmetry data[46]. The generators then employ QCD cascade approximations to simulate higher-order effects.

The vast majority of the Monte Carlo samples used in this analysis were generated

with version 5.6 of the HERWIG Monte Carlo program[47]. HERWIG was originally chosen over another event generator, PYTHIA[48] due to the fact that it was shown to reproduce the observed properties of multijet events in the CDF data[49]. Calculations with PYTHIA are used as a cross check and the ability to generate PYTHIA events without initial state radiation is a valuable tool in the computation of several systematic uncertainties.

The simulation of $t\bar{t}$ production by both HERWIG and PYTHIA is based on the leading order QCD matrix element. HERWIG then continues with coherent parton shower evolution, cluster hadronization, and an underlying event model based on data collected by CDF. PYTHIA, on the other hand, fragments parton using the Lund string model and models the underlying event with a simulation of multiple parton scattering. Thus, both of the aforementioned generators take into account color correlation between the initial and final state partons.

The output of the event generators consists of a set of four vectors for a number of stable particles. These four-vectors can then be input into the CDF detector simulation. Although CDF has a complete detector simulation available, analyses involving top quark production use a simulation based on parameterized detector response. The parameterizations of detector response in this simulation are based predominantly on testbeam data. Not surprisingly, they have been found to better model the hadronic response of the CDF calorimeter systems than the low level simulation. The decays of B hadrons are modeled by a simulation based on data collected by the CLEO experiment[50]. Since this simulation produces data structures that are in most cases identical to the output of the CDF data acquisition system running on collider data, the same selection and analysis algorithms can be used to analyze both data and Monte Carlo events. Thus, any biases introduced by our selection or reconstruction algorithms should be the same in both our data and our simulated datasets.

3.2.2 Simulation of Background Events

One of the primary backgrounds to $t\bar{t}$ production at the Tevatron is the production of W + jets from processes similar to the one depicted in Fig. 3.1. Gluon splitting of final or

Figure 3.1: A Feynman diagram for W + jets production. This is the principle background source in our data sample.

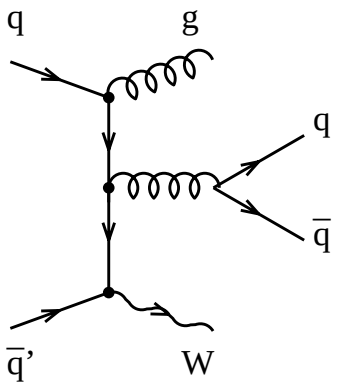

initial state radiation can produce pairs of final state heavy quarks, but the majority of these events are produced without any heavy quarks in the final state. The Monte Carlo program used to simulate the background events in this analysis is known as the VECBOS Monte Carlo program[51]. The VECBOS program is a parton level calculation based on the lowest order diagrams for QCD production of W + jets events.

The events generated for this analysis use the W + 3 jet matrix elements, with the additional jet required to pass our selection criteria (refer to section 3.1.3) being produced during the parton showers. Parton evolution and hadronization are performed using a calculation based on the parton shower model contained in the HERWIG Monte Carlo program. The detector simulation used is the same as the simulation used for signal events. The default renormalization scale used in this generation was set to the mean square p_T of the outgoing partons. Calculations using another Q^2 scale (M_W^2) were made in order to estimate our sensitivity to variations in our Monte Carlo model of the background shape.

Using this technique, a wide variety of distributions in large samples of W + jets events have been reproduced[52]. In addition to this, we have tested the ability of VECBOS to reproduce the background p_T distribution[1] in modified $W + 3.5$ jet samples expected to be

[1]This distribution amounts to the "reconstructed top p_T" in background events. That is, it is the

depleted in both $t\bar{t}$ and $W+$ jet events. These events were selected by requiring that they pass all of our $W + 3.5$ jet selection criteria except for the isolation requirement.

That is, we define our "non-isolated $W + 3.5$ jet sample" to be those events passing all of our $W + 3.5$ jet selection criteria, except for the lepton isolation requirement. For these events, we demand that

$$I^{e(\mu)} > 0.1 \ . \tag{3.4}$$

This data sample is interesting due to the fact that we expect events passing this selection to originate predominantly from background events containing no W-bosons. These "non-W" backgrounds are not included in the VECBOS calculation, and there is thus no a priori reason to expect their kinematics to be well predicted by our background simulation.

A comparison between the VECBOS prediction for two different renormalization scales and a sum of VECBOS plus 70% non-isolated data is given in Fig. 3.2. The magnitude of the non-isolated data contribution is chosen to be approximately equal to the expected contribution to our background estimate for sources other than QCD production of $W +$ jets. The agreement between these two predictions is satisfactory.

3.3 B Hadron Identification

Although further kinematic selection, beyond what was employed in section 3.1.3, is possible[53], at this point we begin to employ a more efficient technique to separate our signal events from background. We avoid applying further selection criteria on event shape variables and other event properties due to the small size of our data sample. However, the fact that $t\bar{t}$ events are expected to result in two b-hadrons in the final state provides a powerful for background rejection. Due to the fact that the vast majority of the background sources to the $W + 3.5$ jet final state do not have heavy flavor in the final state, the efficient identification of B-hadrons is a powerful selection mechanism. In this chapter we describe two methodologies for doing exactly this. One of these methodologies (SVX tagging) exploits

fitted (please refer to section 4.2) transverse momentum distribution of the three jets in the event that our reconstruction algorithm associates with the hadron-side top quark decay.

Figure 3.2: The p_T distributions for two different VECBOS samples compared with a distribution composed of 70% $Q^2 = \langle p_T \rangle^2$ VECBOS and 30% non-isolated $W + 3.5$ jet data. We choose this combination due to the fact that we expect approximately 30% of the background events in our data sample to contain no W-bosons. Events passing all of the selection requirements except the lepton isolation requirement are expected to originate predominantly from the "non-W" background contributions, and are referred to as non-isolated W data.

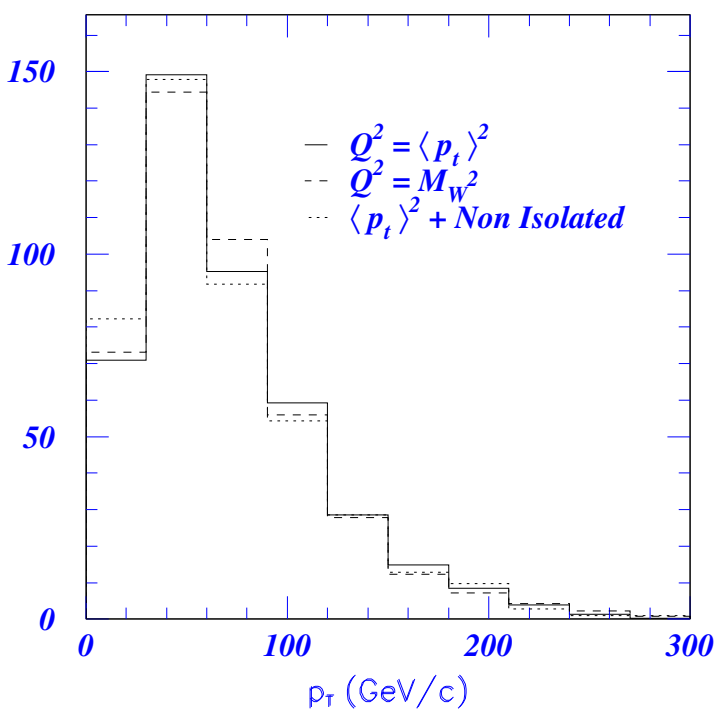

the measurable lifetime of the B-hadrons, and the other exploits their semi-leptonic decay modes (soft lepton or SLT tagging).

Due to the fact that the number of b-tags per event is different in signal and background, this technique also provides a methodology to estimate the total background in our data sample. By separating our sample of $t\bar{t}$ candidate events into so-called "tagging subsamples", each of which is defined by the number and type of b tags that it possesses, we can fit to the fraction of $t\bar{t}$ events in our data sample. These tagging subsamples will also prove invaluable when understanding the kinematic resolution of $t\bar{t}$ events, due to the fact that the p_T resolution achieved by our reconstruction algorithm is better in events that possess b-tags. This brings to the fore yet another benefit of having b-tagging information: due to the fact that jets possessing b-tags have a high probability of arising from the b-quarks produced in Standard Model top quark decay, the correct assignment of jets to partons in $t\bar{t}$ events possessing one or two b-tags is simplified.

Clearly, the identification of B-hadrons will be a very important capability in our study of top quark production kinematics.

3.3.1 The SVX Algorithm

Since B-hadrons have a lifetime of approximately 1.5 ps, and are produced with a most probable p_T of approximately 60 GeV/c in decays of the top quark, they travel an average of 3.4 mm in the radial direction before decaying. Such "secondary vertices" are detected using the silicon vertex detector described in section 2.4.1.

In order to determine the location of the primary vertex in the event, a weighted fit of the trajectories of the charged tracks in the event is performed using SVX information along with the VTX z information. The impact parameter, d (the distance of closest approach to the fitted primary vertex in the $r-\phi$ plane), is used in this calculation. The fit proceeds by iteratively removing tracks with large impact parameters from the primary vertex fit until the most likely vertex is found. The resulting uncertainty in the transverse fitted primary vertex coordinates is between 6 and 26 μm. This resolution is a function of the number of tracks in the vertex and the event topology.

Figure 3.3: A schematic diagram of a displaced vertex. The primary vertex is the $p\bar{p}$ interaction point, whereas the secondary vertex arises from the subsequent decay of a heavy quark. The impact parameter, d, is the distance of closest approach to the fitted primary vertex in the $r-\phi$ plane. L_{xy} is defined to be the distance, in the transverse plane, between the primary and secondary vertices. Events with negative L_{xy} are those in which the secondary vertex lies in the opposite hemisphere to the associated jet (see text), as shown below.

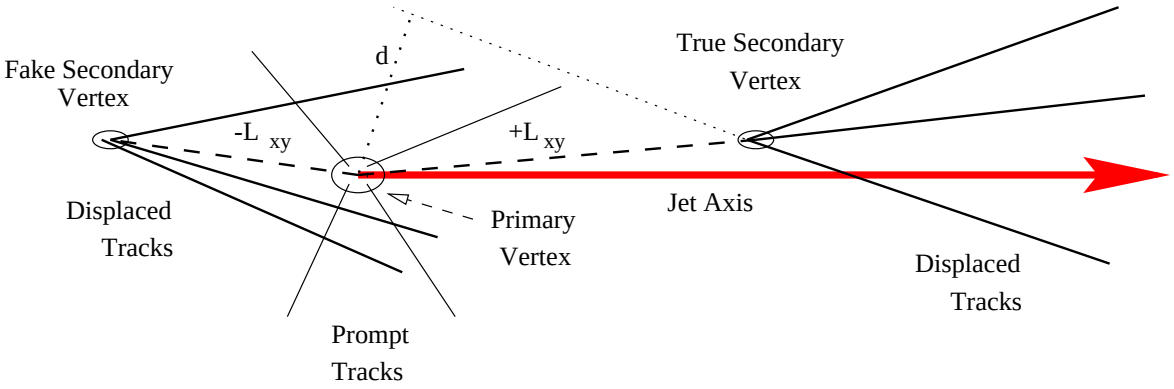

At the typical instantaneous luminosities delivered to CDF, especially during the course of Run IB, multiple $p\bar{p}$ interactions were common. Indeed, the average number of interactions per bunch crossing was 1.8. In order to deal with this potential problem, charged tracks used in the reconstruction of either the primary or secondary vertices in the event were required to extrapolate to within 5 cm of the associated vertices in z.

A sample secondary vertex is depicted in Fig. 3.3. The tracks originating at the secondary vertex are used as an input to a b-tagging algorithm. The aim of this algorithm is to associate displaced vertices formed by two or three charged tracks with jets in the event. The algorithm performs two passes, the first searching for secondary vertices composed of three high-impact parameter tracks, employing loose track quality requirements. If this pass fails to find an acceptable secondary vertex, a second pass, using more stringent track

quality requirements, performs a search for acceptable two-track secondary vertices. The SVX tagging algorithm then attempts to associate these tracks with a jet in the event. A "jet", in this context, is required to have uncorrected $E_T > 15$ GeV and $|\eta| < 2.0$. Large impact-parameter tracks are associated with such a jet if the opening angle between the track direction and the jet direction is less than 35°. The algorithm then computes a quantity known as L_{xy}, defined as the distance between the primary and secondary vertices in the transverse plane. A jet with associated high impact parameter tracks is deemed "SVX tagged" if

$$L_{xy}/\sigma(L_{xy}) > 3.0 \ . \tag{3.5}$$

The sign of L_{xy} is chosen to be positive if the vertex is in the same hemisphere as the jet in question, negative otherwise. The SVX tagging algorithm is describe in more detail in references [16, 44].

The SVX algorithm is CDF's most powerful technique for identifying b-jets in $t\bar{t}$ events. The efficiency for tagging at least one jet in a $t\bar{t}$ event has been measured to be approximately 48%[37]. For background sources possessing real b-quarks in the final state, this efficiency is approximately 25%. For those background sources not possessing b-quarks, the efficiency falls to about 5%. This efficiency depends on the kinematic selection criteria used to define the data sample.

The largest source of background to SVX-tagged $t\bar{t}$ candidate is inclusive W production in association with jets containing b and c quarks. These heavy quarks can arise from gluon splitting ($g \to b\bar{b}$). Charm quarks can also be produced from s quarks in the initial stage, a process that will be referred to as Wc production. Feynman diagrams for the production processes are given in Fig. 3.4.

Fake tags, i.e. secondary vertex candidates associated with jets that contain no real secondary vertices do occur. In order to calculate the rate at which we expect fake tags to occur, we first assume that the distribution of L_{xy} for jets containing no heavy flavor is symmetric about $L_{xy} = 0$. We measure the negative L_{xy} distribution in jets, and parameterize it as a function of jet E_T, η, and the number of reconstructed fiducial SVX tracks in the event, and we use this to calculate a so-called "fake matrix", which describe the probability

Figure 3.4: Sample Feynman diagrams for Wc and $Wb\bar{b}$ production. These are both important sources of background to b-tagged $t\bar{t}$ candidate events.

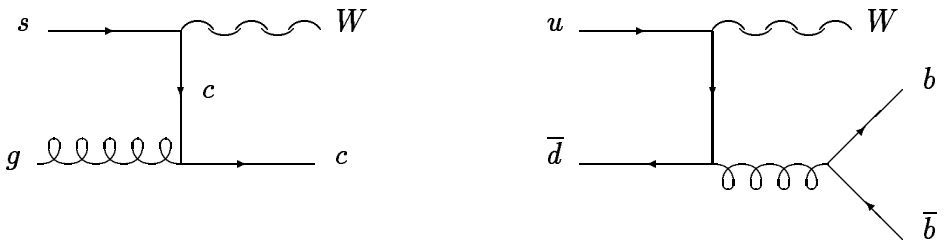

for a jet not containing heavy flavor to be tagged by the SVX algorithm[2]. This fake matrix can then be applied to the $W + jet$ data samples in order to determine the number of fake tags expected in our data samples.

3.3.2 The SLT Algorithm

Since the branching fraction for the inclusive decay $b \to \ell\nu X$ is approximately ??%, an alternative mechanism for identifying heavy flavor decays is to search for the leptons arising from these decays. Since these leptons typically have momentum on the order of a few GeV/c, and are thus much less energetic than the primary leptons in $t\bar{t}$ events, such a procedure is referred to as "soft lepton tagging", or SLT. Soft leptons such as the ones described above can also arise from cascade decays such as $b \to cX \to \ell\nu Y$. Due to the fact that these leptons arise from heavy flavor decays as opposed to leptonic W decay, they also have a higher probability of being non-isolated. The SLT algorithm at CDF searches for soft electron or muon candidates in a manner optimized to identify them in such a complex environment.

These leptons candidates are defined by associating CTC tracks with muon stubs or electromagnetic clusters. In particular, due to the fact that we wish to maintain efficiency

[2]A similar matrix is also calculated for the SLT tags described in section 3.3.2

for the leptons arising from the cascade decays mentioned above, we consider leptons with p_T as low as 2 GeV/c. The lepton trajectory is required to be within $\Delta R < 0.4$ of a jet possessing calorimeter $E_T > 8$ GeV. If the lepton turns out to satisfy the selection criteria described below, this jet is said to be "SLT tagged". For electron candidates, we impose several selection requirements in order to ensure that the electromagnetic cluster in question matches the profile expected from such a lepton. In particular, the transverse profile of the energy deposition in the cluster in both the CEM and the CES are required to match the expected profiles from testbeam electrons. A somewhat different clustering algorithm is used for primary lepton candidates, in order to deal with the fact that these leptons tend to be non-isolated. For muon candidates, tracks in the CTC are matched to corresponding tracks in the muon chambers. A more complete description of the SLT tagging algorithm can be found in [16].

We measure the efficiency of the SLT tagging algorithms using well-understood sources of leptons. For electrons, photon conversions are used, whereas for muons, the decay $J/\psi \to \mu\mu$ is used. Applying this efficiency (which is a function of the transverse momentum of the lepton in question) to Monte Carlo $t\bar{t}$ events allows us to measure the tagging efficiency in $t\bar{t}$ events to be approximately 15%[37].

The SLT algorithm is less efficient than the SVX tagging algorithm, and it also has a higher rate of fake tags. The principle background source to SLT tags is fake tags, that is, particles that are identified as leptons by the algorithm but are not actually leptons associated with the semi-leptonic decay of a heavy quark. Conversion electrons and muons originating from Kaon decay are possible sources of these fake tags as are hadrons that are misidentified as leptons. As was done for the SVX algorithm, a fake matrix can be calculated by measuring the fraction of events in generic (mostly light-quark) jets that possess SLT tags. Applying this matrix to the $W+$ jet data sample results in an estimate of the number of fake tags.

Despite the larger background rates, since the SLT algorithm tags b-quarks in a fashion almost completely uncorrelated with the SVX, it provides additional information as well as serving as a cross check.

Chapter 4

Reconstruction of $t\bar{t}$ candidates

In the preceding chapters, we have described our methodology for selecting $t\bar{t}$ candidate events at CDF. We now proceed to describe our methodology for reconstructing the $t\bar{t}$ kinematic variables that describe the production and decay of the $t\bar{t}$ system. In order to do this we must first make unbiased measurements of the "physics objects" in the event and then proceed to correctly assign these physics objects to the initial state partons.

Although the energy depositions recorded in CDF's calorimeter subsystems are correlated with the energies of the partons from which they evolve, a set of corrections to the reconstructed jet energies must be applied in order to obtain make unbiased measurements of the jet energies. These corrections account for such effects as the absolute energy scale of the calorimeter, the energy deposited in the hadronic cluster by particles arising from the underlying event, multiple interactions and the relative response of the various calorimeter subsystems. An additional set of flavor-specific corrections are also applied.

Following a description of these "jet energy corrections", we proceed to describe the kinematic fit we use in order to reconstruct our $t\bar{t}$ candidate events. Due to imperfect measurement of the relevant physics quantities in the event, and the resultant ambiguity in assigning the physics objects in the event to initial-state partons, our kinematic fit introduces significant biases in event reconstruction. These biases are a function of top quark p_T.

4.1 Jet Energy Corrections

The raw jet momentum is calculated by a vectorial summation of the calorimeter towers contained in the jet cluster. This raw jet measurement is performed employing the assumption that each tower in the cluster represents a particle of zero mass[58].

In this section we describe two sets of corrections:

- those corrections applied to all jets in the event, and
- those corrections designed for Standard Model $t\bar{t}$ events that are applied to the four jets in the event that are assumed to arise from the decay of the $t\bar{t}$ system. These correction themselves are flavor-specific, with an additional correction factor applied to those jets that are associated with b quarks.

4.1.1 Flavor Independent Jet Corrections

To account for systematic differences between the parton momentum and the raw calorimeter energy of the resulting jet, we employ a set of flavor-independent jet energy corrections. These corrections are almost exclusively derived from CDF inclusive jet data, in a fashion that will be described below.

The jet energy corrections are incorporated into CDF's offline reconstruction code using an expression of the form

$$p_T(R) = (p_T^{raw}(R) f_{rel} - UEM(R)) f_{abs}(R) - UE(R) + OC(R). \tag{4.1}$$

In this equation

- $p_t^{\mathrm{raw}}(R)$ is the transverse momentum of the jet, as measured by the calorimeter,
- $R = \sqrt{(\Delta\eta)^2 + (\Delta\phi)^2} = 0.4$ is the cone radius for our clustering algorithm,
- f_{rel} is the relative energy scale, used to correct for non-uniformities in the calorimeter response as a function of η,
- $UEM(R)$ takes into account energy from multiple interactions in the event,

- f_{abs} sets the absolute energy scale,
- $UE(R)$ accounts for the energy deposition due to to the underlying event, the extra energy due to the $p\bar{p}$ interaction that is not associated with the hard scattering in the event, and
- $OC(R)$ is the correction term for energy not contained in the cone of radius $R = 0.4$, and is the so-called "out of cone" correction.

The relative energy correction is derived from a dijet balancing analysis, and accounts for differences in the detector response in the different calorimeter subsystems[58]. The plug and forward regions can thus be calibrated relative to the central calorimeter. The uncertainty in the relative corrections ranges from 0.2-4.0%, with the higher values occurring near the cracks between detector components.

Due to the fact that the mean number of interactions per bunch crossing increased from 0.6 in Run IA to 1.8 in Run IB, different values for the $UEM(R)$ and $UE(R)$ terms are used for data collected during these two time periods. For Run IA, the sum of these two terms was set to 0.72 GeV/c. This correction was applied after the absolute correction described below. For Run IB, these two effects were separated, with $UEM(0.4) = n_v 0.197$ GeV/c, where n_v is the number of additional reconstructed vertices in the event. For the underlying event, we subtract $UE(0.4) = 0.65$ GeV/c after the absolute corrections have been applied. The uncertainty in these corrections is very small, as shown in Fig. 4.1.

The absolute corrections are derived by requiring correspondence between the simulation of the CDF calorimeter and the data. The absolute calorimeter energy scale is studied using testbeam data, minimum bias events, and actual physics data. This correction accounts for, among other effects, calorimeter non-linearity, cracks between detector components, and variation of calorimeter response between and along the different wedges that compose it. The absolute correction, $f_{abs}(0.4)$ varies from approximately 1.3 for raw jet $p_T = 15$ GeV/c to about 1.12 for raw jet $p_T > 100$ GeV/c. The uncertainty in these corrections in plotted in Fig. 4.1.

Soft gluon radiation from final-state partons results in observed energy depositions that

Figure 4.1: Uncertainty in the different terms contributing to CDF's jet corrections. The cone size used is $R = 0.4$.

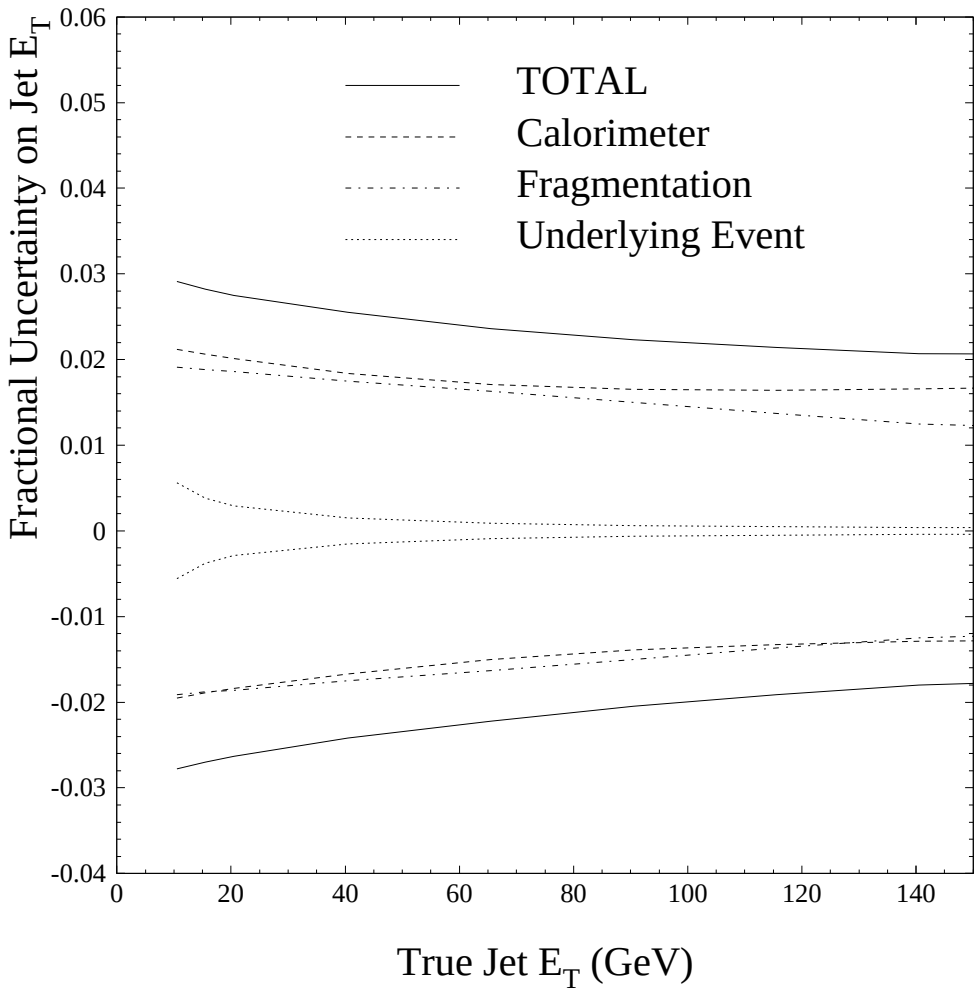

lie outside the clustering region. This is accounted for by applying an out-of-cone correction that varies with p_T in almost exactly the same fashion as the absolute corrections described above. In order to compute the systematic uncertainty in this correction, $W + 1$ jet data was compared to HERWIG simulations of the same process. In both cases, the distribution of energy contained in an annulus with inner and outer radii of $R = 0.4$ and $R = 1.0$ is computed. The mean of the ratio of these two distributions is taken to be the systematic uncertainty in the out of cone correction. This systematic uncertainty varies from approximately 5% for raw jet $p_T = 15$ GeV/c to about 1% for raw jet $p_T > 100$ GeV/c. In addition to this, we assign an additional "splash-out" uncertainty of 1 GeV/jet to account for the energy deposited in the regime $R > 1$. This uncertainty has been shown to be quite conservative[37].

In summary, the total correction factor varies from about 1.65 at corrected jet $p_T = 15$ GeV/c to 1.35 for jet $p_T > 120$. The total systematic uncertainty in the corrected jet energies varies from about 10% at corrected jet $p_T = 15$ GeV/c to 3.5% for jet $p_T > 120$.

4.1.2 Flavor-Specific Corrections

The four leading jets in the event are assigned by our reconstruction algorithm to the jets arising from the decay of the $t\bar{t}$ system (see section 4.2). These corrections account for three separate effects, and their magnitude has been estimated using calculations that employ the HERWIG Monte Carlo program. The effects are:

- the difference in p_T spectrum between a jet originating from top quark decay and the flat p_T spectrum used to derive the absolute corrections,
- the energy lost through semileptonic heavy flavor decays, in particular from the undetected neutrino, and
- the differences in energy deposition in the calorimeter between dijet final states and the multijet final states associated with $t\bar{t}$ candidate events.

In Fig. 4.2, we compare the p_T distributions for b quarks in HERWIG $t\bar{t}$ decays with the p_T distribution of light quarks arising from the hadronic top quark decay.

Figure 4.2: The HERWIG predictions for the shape of the p_T distributions for quarks arising from top quark decay. The dashed distribution corresponds to the b-quarks, the solid distribution to the light quarks.

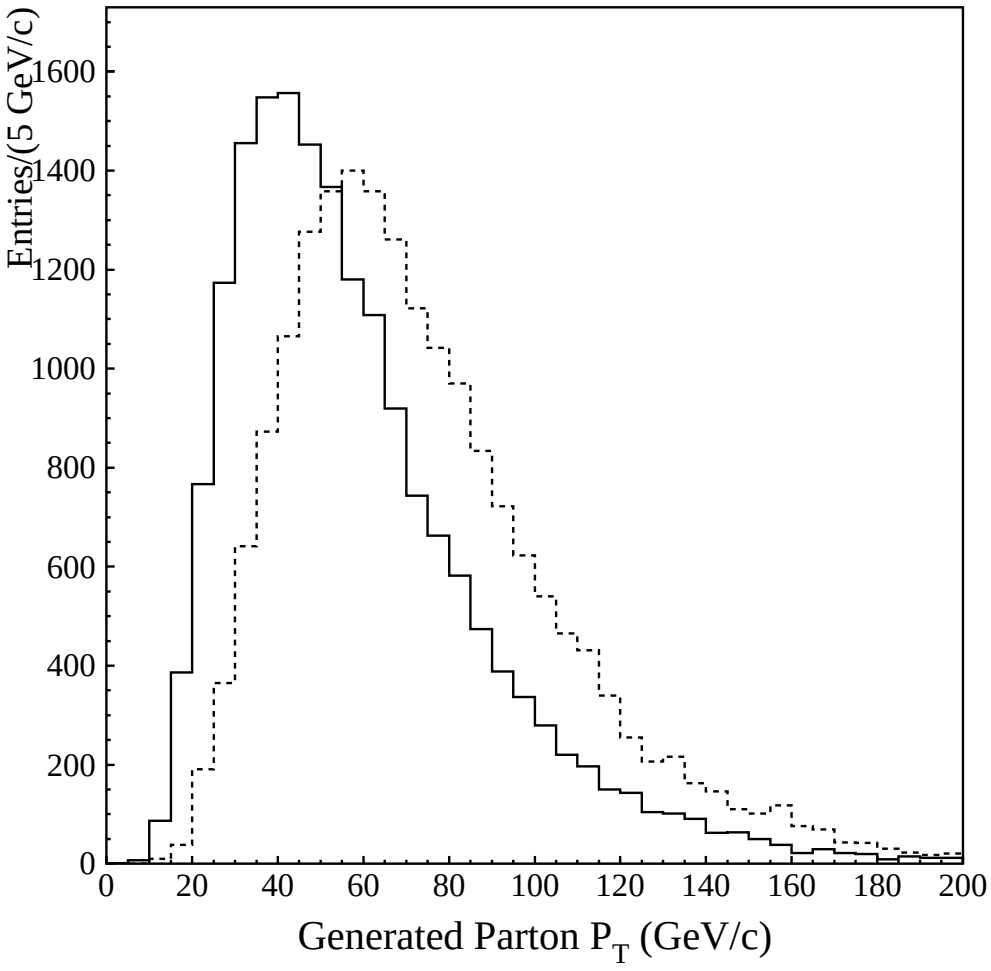

The flavor-specific corrections are different in the case where the jet in question is associated with an SLT tag. There are separate correction factors for soft electron and soft muon tags. The magnitude of the flavor-specific correction for each of the four possible cases is plotted in Fig. 4.3 as a function of corrected jet p_T. The uncertainty in these corrections is estimated by computing the RMS difference between the corrected jet energies and the parton energies in HERWIG Monte Carlo samples. These uncertainties are used in the kinematic fit described below in order to define the range over which the jet energies are allowed to vary.

A separate systematic uncertainty is not required for the parton-specific corrections. Uncertainties can that could arise from calorimeter response or the modeling of soft gluon radiation have already been taken into account. We investigate separately the effect of varying the momentum distribution of the top quarks (and hence the momentum distributions of their associated daughters).

4.2 The Kinematic Fit

The process of reconstructing the kinematics of $t\bar{t}$ events involves finding measurable quantities in the event that are correlated to the kinematic quantities of interest. Thus, in principle, it is possible to make a measurement of the top quark p_T distribution by employing such quantities as the total transverse energy in the event (often referred to as H_T) or by using the measured p_T distribution of b-tagged jets in the event. Employing a technique such as this one does present its difficulties, however, in that many possible systematic effects are folded into the measured distribution. Ideally, we would like to reconstruct the actual variable of interest (in this case p_T) on an event-by-event basis. This is the approach that the CDF collaboration has traditionally chosen for it's top quark mass and kinematics measurements[57, 59], and is the approach that we adopt here.

Figure 4.3: The $t\bar{t}$-specific jet energy corrections that are applied to jets based on the available information from the kinematic fit and the b-taggers. The four separate curves apply to A) jets arising from decays of the W boson, B) jets assigned to b-quarks by the kinematic fit, but possessing no SLT tag, C) jets with a soft electron tag, and D) jets with a soft muon tag.

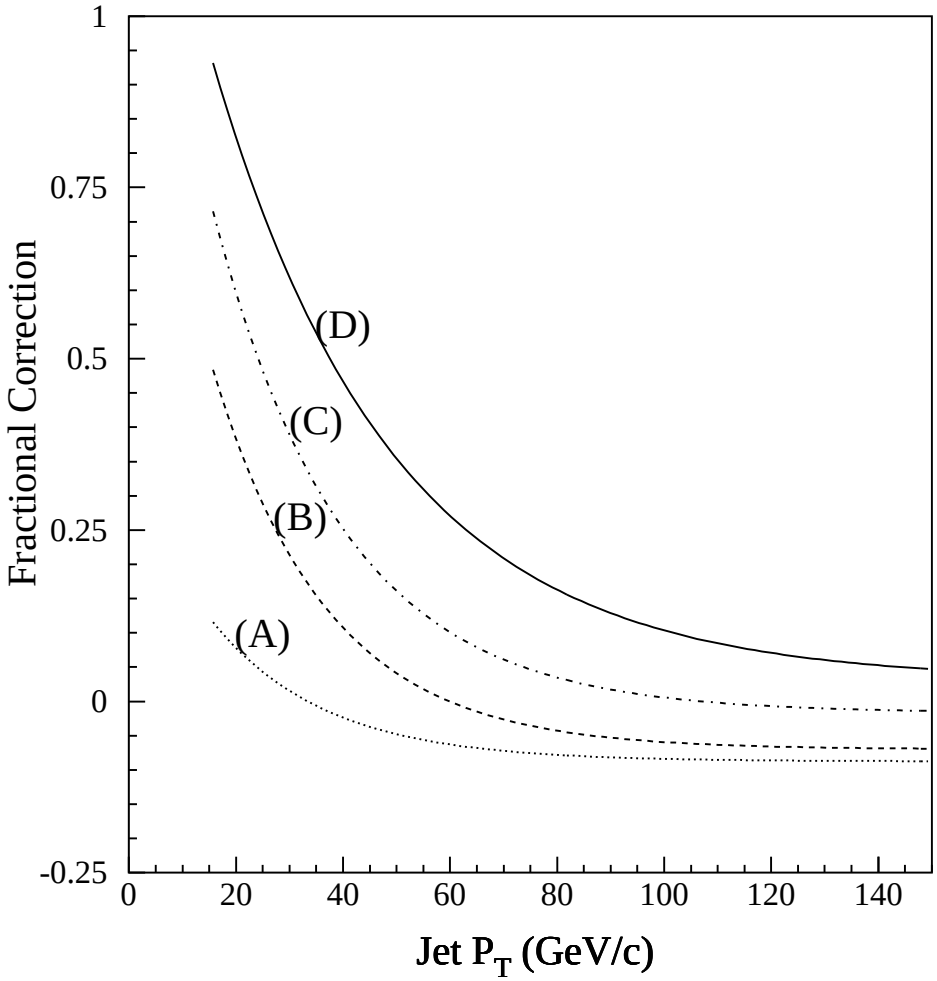

Let us focus, for the moment, on the lepton + jets final state, arising from

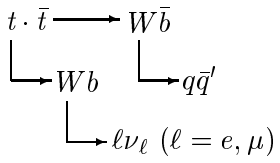

(4.2)

In the absence of initial and final state radiation, we expect four jets, a lepton, and a neutrino in the final state. We use the variable X to signify any additional particles against which the $t\bar{t}$ system is recoiling.

After applying the selection criteria described in Section 3.1.3, we associate the highest-$p_T(E_T)$ isolated muon(electron) candidate in the event with the lepton originating from the semi-leptonic decay of one top quark(the "primary" lepton). The missing transverse energy in the event is taken as an estimate of the transverse energy of the neutrino associated with this same decay. We are now faced with the problem of associating the measured jet energies in the event with the hadronic decay products of the $t\bar{t}$ pair.

We begin by examining the assumption that the four highest E_T jets in each event are associated with the decay products of the top quark. In the absence of initial and final state radiation, this would be the correct assumption to make. However, in HERWIG Monte Carlo samples, the fraction of $t\bar{t}$ events in which one of the leading four jets arises from either initial or final state radiation[1] is approximately 45%. Thus, employing this assumption will lead to a scenario where we can make the correct jet-parton assignments at most 55% of the time. Thus, we could consider adding information from additional jets into the event. In Fig. 4.4, we plot the number of jets in HERWIG Monte Carlo events (in addition to the four jets required to pass our standard selection criteria) that satisfy the selection cuts $|\eta| < 2.4$, $E_T > 8$ GeV/c. In approximately 50% of the the events, there exists at least one additional jet.

Figure 4.4 certainly demonstrates that the fifth jet information is there, if we choose to use it. However, considering a fifth jet increases the number of jet-parton assignments that we must attempt by a factor of five. In all algorithms that we have considered, this added

[1]This fraction is usually referred to as the "hard gluon fraction".

Figure 4.4: The number of additional jets (beyond the first four) in HERWIG Monte Carlo events that pass our selection criteria. In this plot, we define a 'jet' to have $|\eta| < 2.4$, $E_T > 8$ GeV/c.

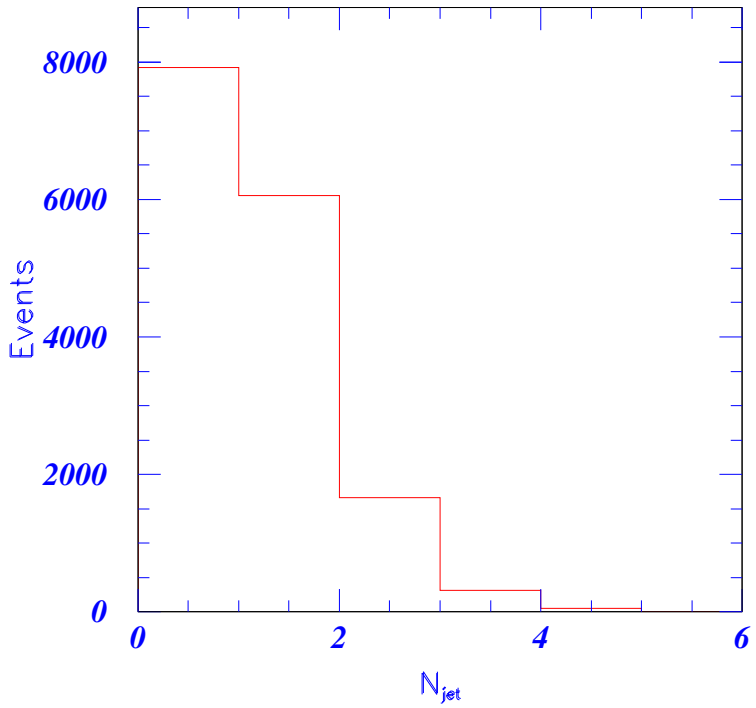

complication has reduced, rather than increased the fraction of events for which the correct jet-parton assignment is obtained.

Thus, our algorithm will assign the four leading jets to the $t\bar{t}$ decay daughters. We proceed as follows. Firstly, we apply the jet energy corrections described in section 4.1 to all of the jets in the event. We then obtain several constraints based on conservation of energy and momentum. We obtain six constraints, listed below.

- The transverse components of the momentum of the $t\bar{t}$ system must be zero (2 constraints).
- The invariant mass of the two top quarks must be $m_t = 175$ GeV/c^2 (2 constraints).

- The invariant mass of the $\ell\nu$ system must be $M_W = 80.4$ GeV/c^2.
- The invariant mass of the two jets originating from the hadronic W decay must be equal to M_W.

The relevant unmeasured quantities are the three components of the neutrino momentum.

We choose to solve the resulting over-constrained system of equations by minimizing the χ^2

$$\begin{aligned}\chi^2 &= \frac{(m_{\ell\nu} - M_W)^2}{\Gamma_W^2} + \frac{(m_{jj} - M_W)^2}{\Gamma_W^2} \\ &+ \frac{(m_{\ell\nu j} - M_t)^2}{\Gamma_t^2} + \frac{(m_{jjj} - M_t)^2}{\Gamma_t^2} \\ &+ \sum_i^{N_{l,jets}} \frac{(\hat{E}_T - E_T)^2}{\sigma^2(E_T)} + \sum_{i=x,y} \frac{(\hat{U}_i - U_i)^2}{\sigma^2(U_i)} \ . \end{aligned} \tag{4.3}$$

Since there are six constraints and three unknowns, we are left with a three constraint (3C) fit.

The first sum in Equation 4.3 runs over the primary lepton and all the jets in the event satisfying the selection criteria $|\eta| < 2.4$ and $E_T > 8$ GeV, whereas the second sum runs over the transverse components of the calorimeter energy depositions not associated with any jets, the "unclustered energy". The variables $\hat{E}_T$ and $\hat{U}_i$ refer to the values output by the fit whereas the variables E_T and U_i refer to the measured (input) values. The symbol ℓ refers to the primary lepton in the event whereas ν stands for the inferred neutrino. The mass of the W boson is set to 80.4 GeV/c^2, and its width (Γ_W) is set to 2.1 GeV. The mass of the top quark is set to 175 GeV/c^2, and its width (Γ_W) is set to 2.5 GeV. The kinematic resolution has been found to be virtually independent of the values of the widths used. The uncertainties in the measured jet and lepton energies are discussed in Sections 4.1 and 2.3, respectively. The χ^2 is minimized employing the MINUIT algorithm[60].

In the absence of b-tagging information, there are 12 different ways to assign the four leading jets in the event to either the hadronically-decaying W-boson or one of the two b quarks that would be expected in $t\bar{t}$ events. The two jets assigned to the hadron-side W

boson can be interchanged without creating a new permutation. Furthermore, the solution for the z component of the neutrino's momentum has a quadratic ambiguity typically resulting in two solutions for every possible jet-parton assignment, or 24 permutations in total. If there are jets in the event possessing an SLT or SVX tag, these jets are required to be associated with b quarks in the fit. This reduces the number of possible configurations to 4(12) in the case of 2(1) b-tagged jets. We perform the fit for all permitted configurations and choose the solution with the best χ^2.

Events for which the lowest permitted χ^2 is greater than 10 are rejected. This cut removes 22 events from our dataset, leaving us with 61 events in our data sample. This fit provides, on an event by event basis, a measurement of the top quark transverse momentum. We define the top quark p_T in an event to be the the vector sum of the transverse components of the jet momenta associated with the hadronically-decaying top quark candidate.

4.3 Kinematic Resolution and Parton Assignments

When the fitter is run on the standard HERWIG Monte Carlo samples and the output is compared to the true values for a given kinematic variable, it is found that the p_T resolution functions are broad, asymmetric, and non-Gaussian. For example, in Fig. 4.5 the distribution of residuals (defined as p_T(fitted) $-$ p_T(true)) on reconstructed p_T for events passing our selection selection criteria is depicted.

Furthermore, in Fig. 4.6, we compare the expected distribution at the generator level (the "true" values) and for full detector simulation and event reconstruction. It is evident that the p_T distribution could be significantly modified by reconstruction using the MINUIT mass fitter alone.

In Fig. 4.5, the non-Gaussian nature of the p_T resolution function becomes evident. In order to determine how the resolution varies as a function of true p_T, in Fig. 4.7 we plot the distribution of measured p_T for four different bins of true p_T. The distribution of reconstructed momenta for true pt in the range $150 < p_T < 225$ GeV shows a very broad distribution, with a significant fraction of the events falling in the region of low

Figure 4.5: The p_T resolution functions for Monte Carlo events passing the selection criteria of the mass analysis. The kinematic fit is constrained to return a top mass of 175 GeV. This plot includes both the semileptonically-decaying and hadronically-decaying top quarks in the standard HERWIG sample. To aid in making the comparison, the distributions are normalized to the number of events in the untagged sample.

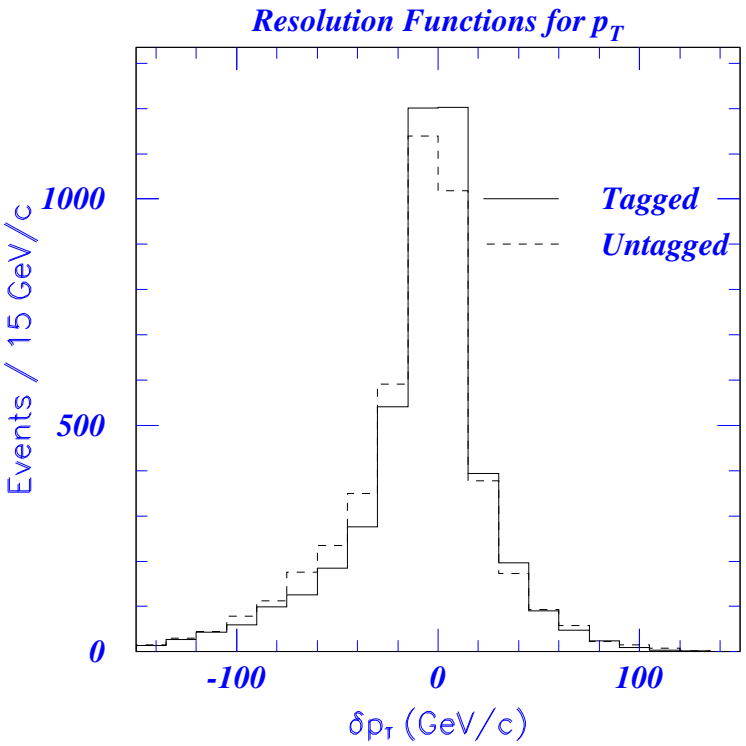

measured p_T. This indicates that the MINUIT kinematic fitter introduces significant bias during reconstruction.

Taking into consideration the fact that events with true p_T above 150 GeV have a significant probability of being reconstructed with low p_T, an interesting question to ask is what limits can be placed on the true momentum distribution of top quarks produced at CDF. In Section 5, we describe a likelihood methodology that provides these limits.

Figure 4.6: A comparison of the smeared and true distributions for two different models of top quark production. The smeared distribution is plotted with error bars. Although the plots are made for a high statistics Monte Carlo sample, the sizes of the error bars on the smeared distribution are determined by what is expected for the 61 Event sample that passes our final selection criteria. The left plot is for the Standard Model and the right is distribution with enhanced hard top quark production.

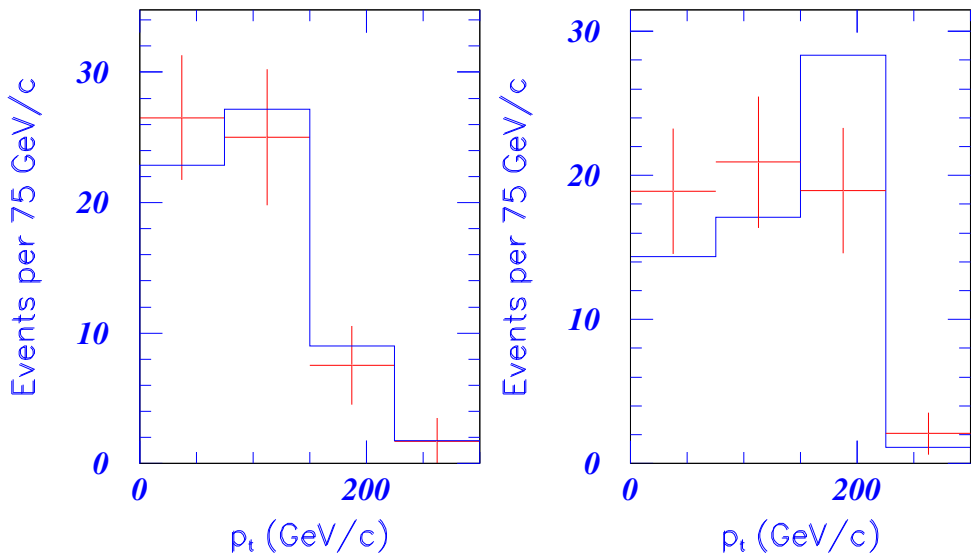

4.4 Parameterizing the resolution

In Fig. 4.7, a parameterization employing two Gaussian functions of the distribution of measured p_T's in each of four 75 GeV/c bins of true p_T are plotted. We shall refer to these four curves as our "response functions". In reality, the response function appropriate for a given top quark is a function of a number of variables. In particular, events where one of the b quarks is tagged by either the SLT or SVX algorithms will show somewhat superior p_T resolution to untagged events. The shape of the observed momentum distribution in both

Figure 4.7: Fits to the reconstructed p_T distribution in each of four true p_T bins. This plot includes only the hadronically-decaying top quarks, and assumes a Standard Model top quark p_T distribution within each bin. The Monte Carlo statistics of the standard HERWIG sample have been supplemented at high p_T by additional Monte Carlo production.

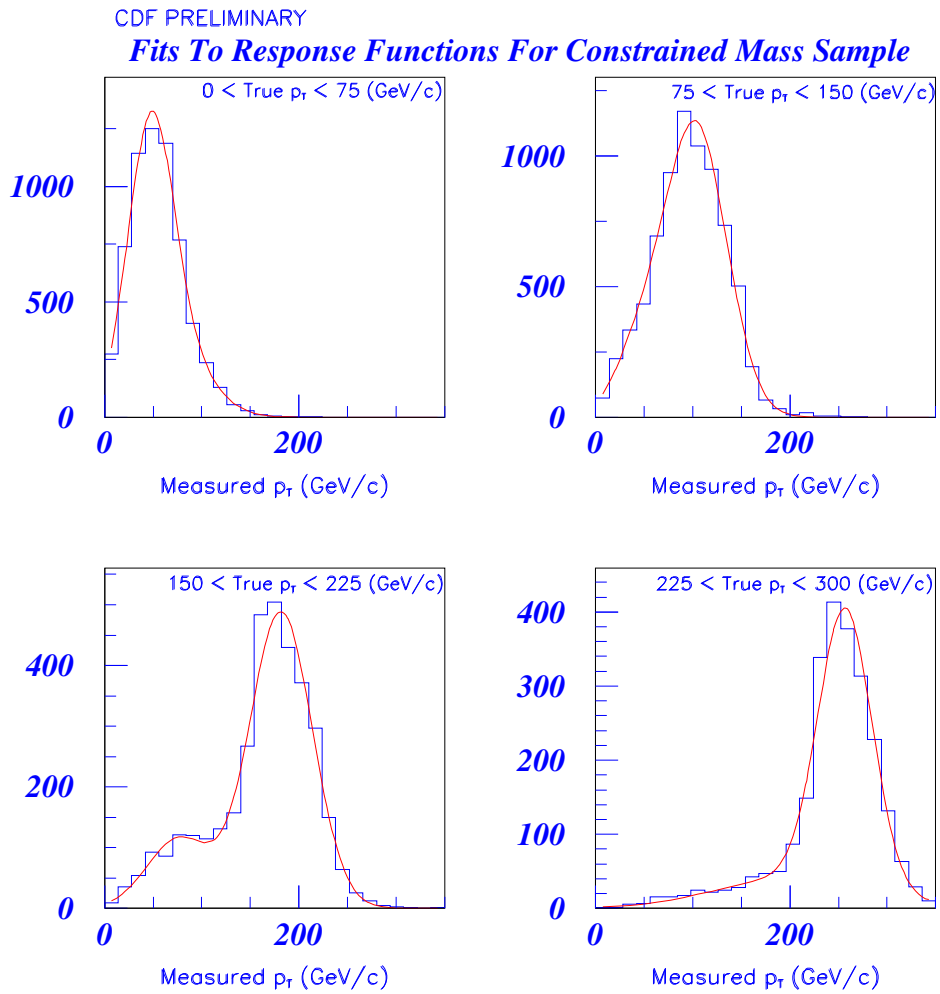

Figure 4.8: Comparison of the measured p_T distribution for the single tag and no tag case in the second true p_T bin (75 GeV/c< p_T <150 GeV/c). There are approximately 1000 events in each distribution. Similar effects exist for the other three bins of true p_T, but are most pronounced in this bin. Only the p_T reconstructed using the hadronically-decaying top quark candidate is used.

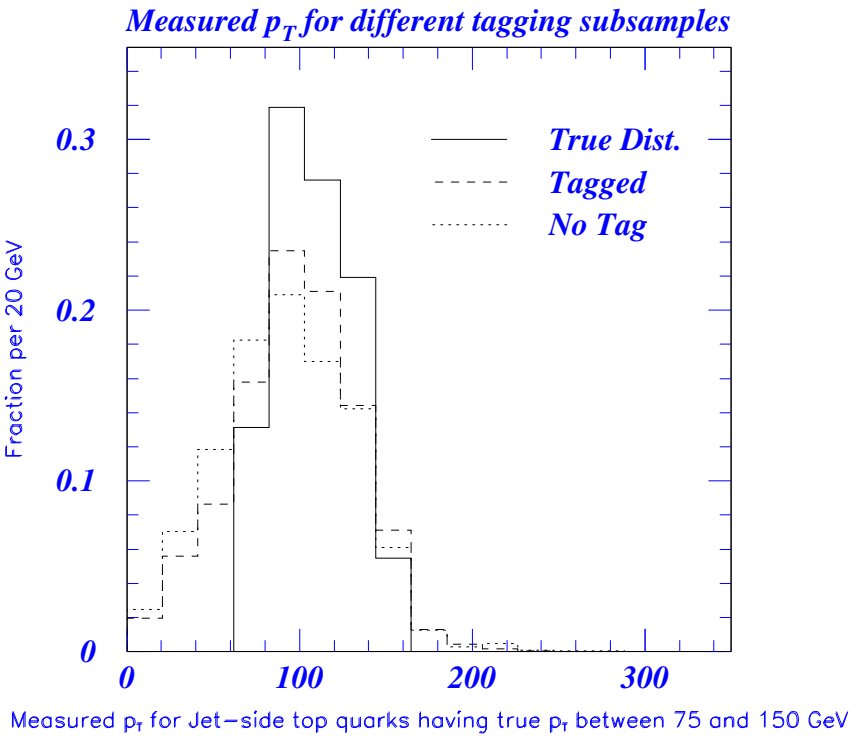

tagged and untagged events is illustrated in Fig. 4.8 for the case[2]. where true top quark p_T is in the range 150 GeV/c < p_T < 225 GeV/c The improvement in resolution is not large, as evidenced by this plot.

One also expects some differences in p_T resolution for top quarks decaying into jets when compared to those decaying semileptonically. For true p_T in the range 75 GeV/c < p_T < 150 GeV/c, the lepton and jet side top quark p_T distributions are compared in Fig. 4.9.

[2]This is a somewhat arbitrary example, chosen because it is in this bin that the corrections to the MINUIT output are largest

Figure 4.9: Comparison of the measured p_T distribution for the lepton-side and jet-side case in one true p_T bin. This bin is where effects due the top quark decay mode are most evident.

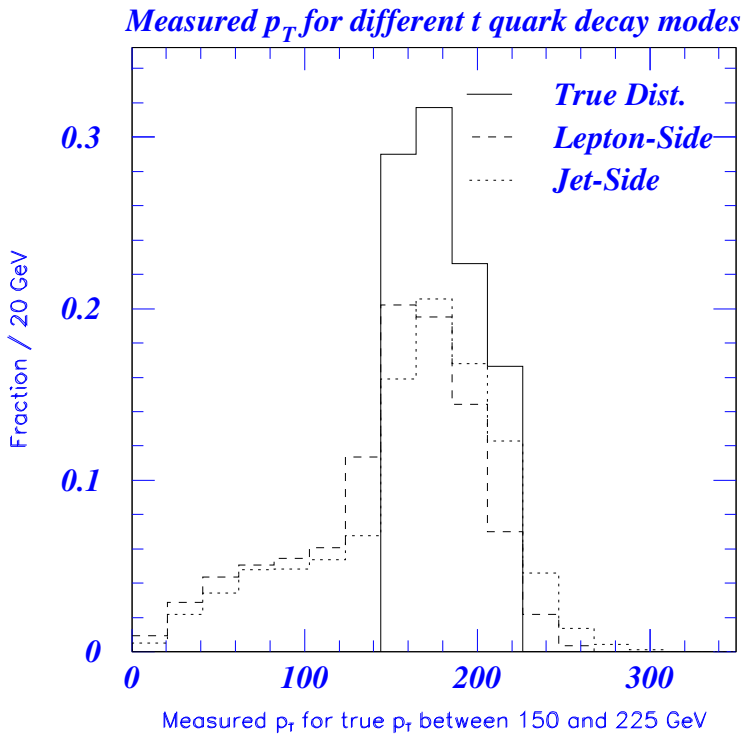

The plot in Figs. 4.8 and 4.9 show that the gross features of the measured p_T distributions are the same in each of the tagging/decay mode subsamples. However, there are some significant differences in the distributions as well. One such difference is apparent in Fig. 4.9, where the probability to measure $p_T > 200$ GeV/c is twice as large for a hadronic top quark decay as it is for semileptonic decay. Thus, an event with measured $p_T > 200$ GeV/c has a rather different interpretation in each case.

More significant differences exist for the cases of the constrained MINUIT fit and the unconstrained fit, for both lepton-side and jet-side top quarks. The constrained fit, whose χ^2 is denoted by χ^2_c, is the version of the kinematic fit described in section 4.2 where we

constrain the reconstructed top quark mass to be 175 GeV/c^2. In the unconstrained fit, whose χ^2 is denoted by χ^2_{nc}, no such constraint is made. The RMS error decreases from 44 to 36 GeV, while the acceptance decreases (for both signal and background) by about 15% when one removes events having $\chi^2_c < 10$, rather than making the same cut on χ^2_{nc}. Response functions for the two cases are compared in Fig. 4.10. They are once again similar in form, with the mass-constrained distribution being somewhat less biased toward lower p_T.

It is clear from these distributions, that the reconstructed momenta returned by the MINUIT mass fitter are not an unbiased estimator of the true top p_T distribution. The magnitude of this bias depends, to a certain extent, on the tagging characteristics of the top quark sample under consideration. On the basis of the studies presented in this section, we see that different response functions are necessary for tagged and untagged events, as well as top quarks decaying hadronically and leptonically.

Figure 4.10: Comparison of the measured p_T distribution for the mass-constrained and unconstrained fits in the true p_T bin $150 < p_T < 225$ GeV. The standard mass selection criteria as well as the $\chi^2 < 10$ cut are applied in each case.

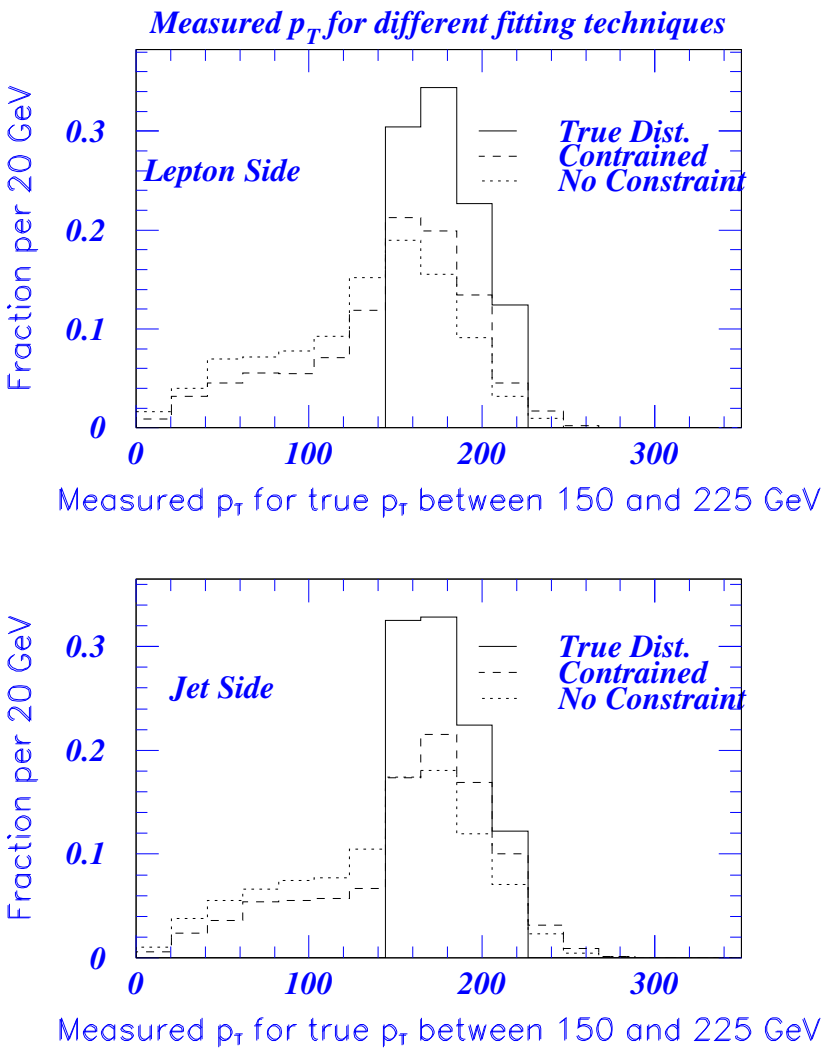

Chapter 5

Measuring the Top Quark p_T Distribution

As discussed in section 4.2, we reconstruct $t\bar{t}$ events on an event-by-event basis by employing a kinematic fitting routine that constrains the reconstructed top quark mass to be 175 GeV/c^2. Due to biases that appear in the reconstructed p_T distributions, we employ a procedure for correcting for these effects, thus producing a set of confidence levels that have been corrected for all detector and reconstruction effects. This methodology is based on the use of so-called "response functions," distributions of reconstructed transverse momenta in each of a number of true p_T bins. These response functions depend, at some level, on the shape of the true p_T distribution that is being reconstructed, and we account for this systematic uncertainty in our confidence intervals.

Before describing the unsmearing methodology used in this analysis, however, we engage in a brief discussion of correlations between the reconstructed and true transverse momenta of the top and anti-top quarks in a given event. Evidence of a strong correlation between these two quantities forces us to use the information from only one top quark per event. We also describe the calculation of the expected backgrounds in the data sample used to measure the top quark p_T distribution. This calculation uses the output of the b-tagging algorithms described in Sections 3.3.2 and 3.3.1.

5.1 Backgrounds to $t\bar{t}$ Production

In order to extract the true top quark p_T distribution, we must understand both the shape and normalization of the background contributions to our data sample. In this section, we describe the background calculation that fixes the normalization of the estimated background distributions. Although the majority of the background contribution is expected to arise from QCD production of W + jets, a number of other background sources also contribute. We base our calculation on the background calculation performed in the measurement of the top quark mass. This calculation is summarized below, and a more complete description can be found in [37].

The primary source of background in our data sample is expected to be "W + jets" production. A sample Feynman diagram for this process is depicted in Fig. 3.1. Two important differences between $t\bar{t}$ production and this process allow for their separation. Firstly, the jet energy spectrum in $t\bar{t}$ decays is significantly more energetic than for events produced through this background process. Secondly, the vast majority of W + jets events do not contain jets originating from b-quarks. These are the rationale behind the kinematic selection criteria espoused in section 3.1.3 and the tagging algorithms described in sections 3.3.2 and 2.4.1.

The bulk of the background calculation is performed in the so-called "mass sample", a subset of the 164 events selected in section 3.1.3 that, in addition, possess event kinematics that are well-described by the $t\bar{t}$ hypothesis. A kinematic fit almost identical to the one described in section 4.2 is used in order to make this selection cut, with the sole difference between the two fits arising from the fact that this fit is used to measure the top quark mass on an event-by-event basis, and thus the top quark mass is not constrained in the fit. Imposing the requirement that the χ^2 of this two-constraint fit be less than 10 removes 13 events from the data sample. Thus, the calculations and tagging efficiencies that are described below refer to those calculated for this 151 event sample. At the end of this section, we apply a small correction factor to these background estimates in order to account for the somewhat-more-stringent selection criteria that will be used in the measurement of the

top quark p_T distribution.

The calculation is based on the probabilities of observing either an SVX or an SLT b-tag in signal and background events. We first subdivide our data sample into several subsamples, based on kinematic criteria and what b-tags, if any, are present in the event. Knowing the tagging probabilities then allows for a calculation of the expected background contribution to each of these subsamples. Some of these contributions are estimated as a function of the number of background W-candidates in the data sample, whereas others are absolute predictions. The top mass sample background fraction can then be calculated by a fit to the observed number of events in each of these subsamples.

The events are first subdivided into "Class I" events and "Class II" events. Class II events have four or more jets satisfying the selection criteria $|\eta| < 2.0$, $E_T > 20$ GeV, whereas Class I events have exactly three jets satisfying this criteria. The tagging probabilities for these two event classes will be different due to the differences in the kinematics of the jets in the event. Furthermore, Class II events have a higher signal to background ratio than class I events. We then proceed to further subdivide these events into four "tagging subsamples"[1], which are

1. **SVX Tags** - events possessing only SVX tags,

2. **SLT Tags** - events possessing only SLT tags,

3. **SVX and SLT Tags** - events possessing both SVX and SLT tags,

4. **No Tag** - events with no b tags.

The expected number of events in each of these 8 subsamples can be calculated as a function of the $t\bar{t}$ fraction of the dataset and the number of background $W+$ jets events in the sample. The latter arises due to the fact that some of the background sources are calculated relative to this number. The expression used to perform this calculation is of the

[1]Note that these subsamples are different than those used in the measurement of the top quark mass, and are chosen to optimize the precision on the estimate of the $t\bar{t}$ fraction in the top mass candidate event sample.

form

$$N^j_{exp} = a_j N_{t\bar{t}} + \sum_k c^k_j N^k_{abs,j} + \sum_i d^i_j b^i_j N_W. \quad (5.1)$$

An equation of this form applies to both the class I and class II events. The parameter a_j is the tagging probability in the j^{th} tagging subsample, while c^k_j and b^i_j are the tagging probabilities for background processes k and i. These tagging efficiencies are computed by simulation of the detector response to each of these final states. A list of the background processes that we consider is given in table 5.3. The first six background sources listed in this table are absolute predictions, so that their contributions are taken into account by the first sum in equation 5.1, where $N^k_{abs,j}$ is the number of background events expected from the k^{th} background source. The final four background sources given in this table are calculated relative to the number of real W events not arising from $t\bar{t}$ production, N_W. Their contributions are taken into account by the second sum, where d^i_j is the constant of proportionality between the expected number of background events from source i and N_W.

Equation 5.1 amounts to a prediction for the expected number of events in each of our 8 tagging subsamples as a function of $N_{t\bar{t}}$ and N_W. We eliminate one of these unknown parameters by demanding that the expected number of events in each event class be equal to the observed number of events. At this point, we are left with one parameter for each class of events, the fraction of $t\bar{t}$ events in the dataset. A maximum likelihood fit to the number of observed events in each of the tagging subsamples is then performed in each event class, resulting in an estimate of the $t\bar{t}$ fraction in each of these subsets of the $W + 3.5$ jet data sample. The results of the fit are shown in Table 5.1, and a comparison of the observed and expected numbers of events in each of the 8 subsamples is given in Table 5.2.

The background estimates that were used to derive the results presented in table 5.3 are determined from a combination of data and Monte Carlo studies. Here we briefly expand on how this was done for each of the background sources. The non-W fraction is calculated directly from the data[54]. This is performed by measuring the number of b-tags as a function of lepton isolation and $\not\!\!E_T$. Due to the fact that we expect the sample with low isolation and low $\not\!\!E_T$ to be essentially devoid of real W events, we can use the number of tags in this sample to predict the number of fake tags in events in the signal region. Diboson

Table 5.1: The resulting estimate for the composition of the 151 event Top Mass Candidate sample. These estimates are obtained using the likelihood fit described in the text. From [37].

Process	Class I	Class II
$t\bar{t}$	$11.5^{+6.4}_{-5.2}$	$28.5^{+8.2}_{-7.6}$
$W/Z+$ jets	$67.6^{+5.2}_{-6.4}$	$28.1^{+7.6}_{-8.2}$
Other Bgds	7.9 ± 0.9	7.4 ± 1.8

Table 5.2: A comparison of the predictions of the likelihood fit described in the text to the observed number of events in each of the 8 tagging subsamples. The sum of the expected number of events is constrained to the observed values in the fit. From [37].

	Observed	Observed	Expected	Expected
Only SVX tags	3	10	5.6	12.4
Only SLT tags	6	8	4.2	4.8
SVX and SLT tags	3	4	1.1	3.0
No Tags	75	42	76.0	43.8
Total	87	64	87	64

production is studied using the PYTHIA Monte Carlo program with the production cross section scaled to the theoretical value[55]. Similarly, the $Z \to \tau\tau$ rate is also studied using the PYTHIA Monte Carlo program, and the normalization is obtained by studying $Z+$ jet production in the Run I data sample. Both the PYTHIA and HERWIG Monte Carlo programs are used to study single top production[56], with the theoretical cross section again being used (both the W^* and Wg fusion processes are taken into account).

The calculation of the remaining contributions listed in table 5.3, relative to the number of background W candidate events in our data sample, is performed using a combination of the PYTHIA, HERWIG, and VECBOS event generators. The Monte Carlo generators predict

the relative production rates of each of these final states. Combining this with the tagging efficiency appropriate for a given final state results in a prediction of the relative magnitude of each of these contributions.

One conclusion that arises from the results of this calculation is that there is little to be gained from including Class I events with no b-tag. Out of 75 observed events, only 5.2 are expected to arise from $t\bar{t}$ production. In order to improve the signal to noise ratio, we remove these events from our data sample, leaving us with the 76 event sample that was used to make CDF's measurement of the top quark mass[57]. The expected background contribution in each of four tagging subsamples (different from those described above) is presented in Table 5.3.

In section 4.2 we describe the kinematic fit that we employ in order to reconstruct top quark kinematics on an event-by-event basis. The fit is similar, but not identical, to the fit used to measure the top quark mass in the lepton + jets final state. The difference arises from the fact that we do not allow the top mass to float in the kinematic fit, instead constraining it to a value of 175 GeV/c^2. In order to take this into account, a correction factor to the above results must be applied. We employ VECBOS Monte Carlo event samples generated at two different renormalization scales in order to estimate this fraction. The results are consistent and are presented in Table 5.4. The results of this Monte Carlo Study indicate that we should scale the estimated top mass background by a factor of 0.79 ± 0.08 in order to predict the background contribution to the mass-constrained sample. This number is obtained by taking the $Q^2 = \langle p_T \rangle^2$ VECBOS as our central value and estimating the uncertainty by comparing to the result for the $Q^2 = M_W^2$ VECBOS sample[2]. These results are presented in Table 5.5.

After summing the contributions presented in table 5.3 and applying the correction factor discussed above, we arrive at our final background estimate, presented in table 5.5.

[2]This is exactly what we would have expected from naive scaling based on the sizes of our data samples.

Table 5.3: The expected contribution arising from the various background sources to $t\bar{t}$ production. This chart lists the number of expected background events in various tagging subsamples of the top mass sample[37]. Class I events with no b-tags are not included in this table. We apply a correction factor to generate the estimate of the background normalization in the data sample used to measure the top p_T distribution. The SVX tagging subsample consists of events possessing one SVX tag, events in the 2SVX tagging subsample possess two of these tags, and events in the SLT subsample possess only SLT tags.

Source	SVX	2SVX	SLT	No Tag	Total
non-W/Z	0.5	0.0	1.0	4.6	6.1
WW	0.1	0.0	0.1	0.6	.08
WZ	0.0	0.0	0.0	0.0	0.1
ZZ	0.0	0.0	0.0	0.1	0.1
$Z \to \tau\tau$	0.1	0.0	0.2	0.5	0.8
Single Top	0.0	0.0	0.1	0.2	0.4
$Wc + Zc$	0.2	0.0	0.8	1.7	2.7
$Wb\bar{b} + Zb\bar{b}$	0.8	0.2	0.4	1.1	2.5
$Wc\bar{c} + Zc\bar{c}$	0.4	0.0	0.8	2.0	3.2
$W/Z + u, d, s$	0.2	0.0	4.1	19.6	23.9
Total Bgd.	2.4 ± 0.8	0.2 ± 0.1	7.6 ± 1.3	30.4 ± 4.5	40.7
Obs. Events	15	5	14	42	76

Table 5.4: Number of events passing the mass selection criteria in two different VECBOS samples with and without the mass constraint.

Sample	No Constraint	Constraint	Fraction
2.2 fb^{-1} of e^-/μ^- with $Q^2 = \langle p_T \rangle^2$	413	324	0.785 ± 0.044
6.19 fb^{-1} of e^- with $Q^2 = M_W^2$	1002	802	0.800 ± 0.028

Table 5.5: Estimated background content of our data sample. We divide the data into tagged and untagged events.

Tagging Subsample	Background Estimate
b-tagged sample (29 Events)	8.0 ± 1.5
Untagged sample (32 Events)	23.9 ± 4.3

5.2 Correlations

The first question that we must consider is the statistical power of our data sample. Due to the fact that the momentum of the top quark and the anti-top quark are strongly correlated in any given event, we cannot make two independent measurements of the top quark p_T spectrum in each event that passes our selection criteria. This is demonstrated in Fig. 5.1, where a scatter plot is made of the p_T of the semileptonic decay against the p_T of the hadronically-decaying top quark candidate. A strong correlation is evident.

One can imagine several ways of dealing with this effect. One possibility would be to combine two correlated measurements of the p_T spectrum. This approach, if adopted would greatly complicate the estimation of the statistical uncertainties associated with the measurement. The correlations between the different subsamples used in the measurement would have to be understood. Although this could presumably be done by using Monte Carlo experiments, we have chosen to adopt a simpler approach.

The approach that we have chosen involves making a measurement using only the reconstructed p_T of the top quarks that decay hadronically. This choice is made due to the fact that the predicted p_T resolution for hadronic decays is less biased than that for the semileptonic top quark decays. By considering only one top quark in each event, we also arrive at a set of statistically independent measurements of top quark p_T. This methodology greatly simplifies the uncertainty analysis.

In effect, we discard any information on $p_T(t\bar{t})$. The loss of information with the limited statics of this sample is modest.

Figure 5.1: A scatter plot of the reconstructed p_T for the semileptonic and hadronic decay of the top quark in each event for the data (stars) and HERWIG (dots) Monte Carlo samples.

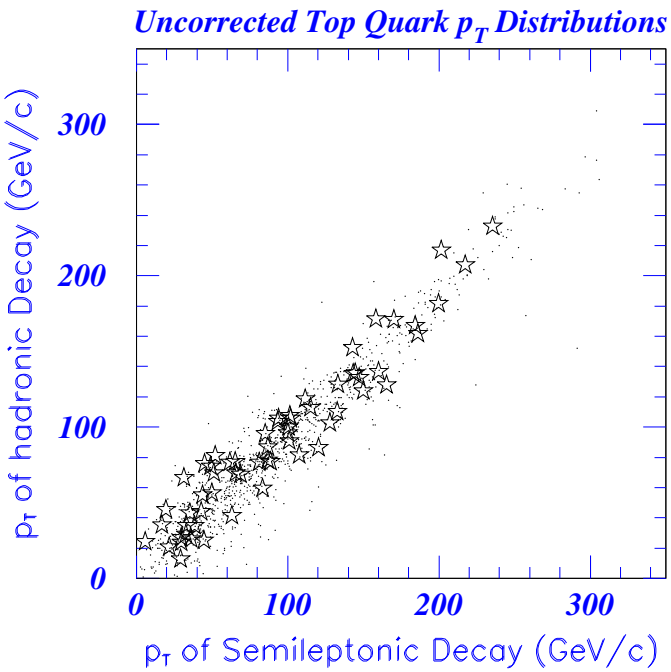

5.3 The Likelihood Fit

In Fig. 4.7, we depict the response functions for each true p_T bin. These functions, estimated from HERWIG Monte Carlo samples that have been processed with a simulation of the CDF detector, are taken to be estimates of the contribution made by each true p_T bin towards the measured p_T distribution. Simply put, the response function for a given true p_T bin is what we would expect the measured distribution to look like if all top quarks were produced with p_T within a given true bin with the Standard Model distribution. These response functions do depend on the distribution of true p_T within each bin. For example, in Fig. 5.2, we compared the expected p_T response functions for the cases where the p_T distribution is as predicted by HERWIG to the case where there is a flat p_T distribution within each bin.

In order to derive the shape of a given response function, we therefore need to make an

Figure 5.2: The response functions for the case where we assume a flat true p_T distribution within each bin compared to the results obtained assuming a Standard Model distribution within each bin. The response functions for events having one or more b tags are plotted.

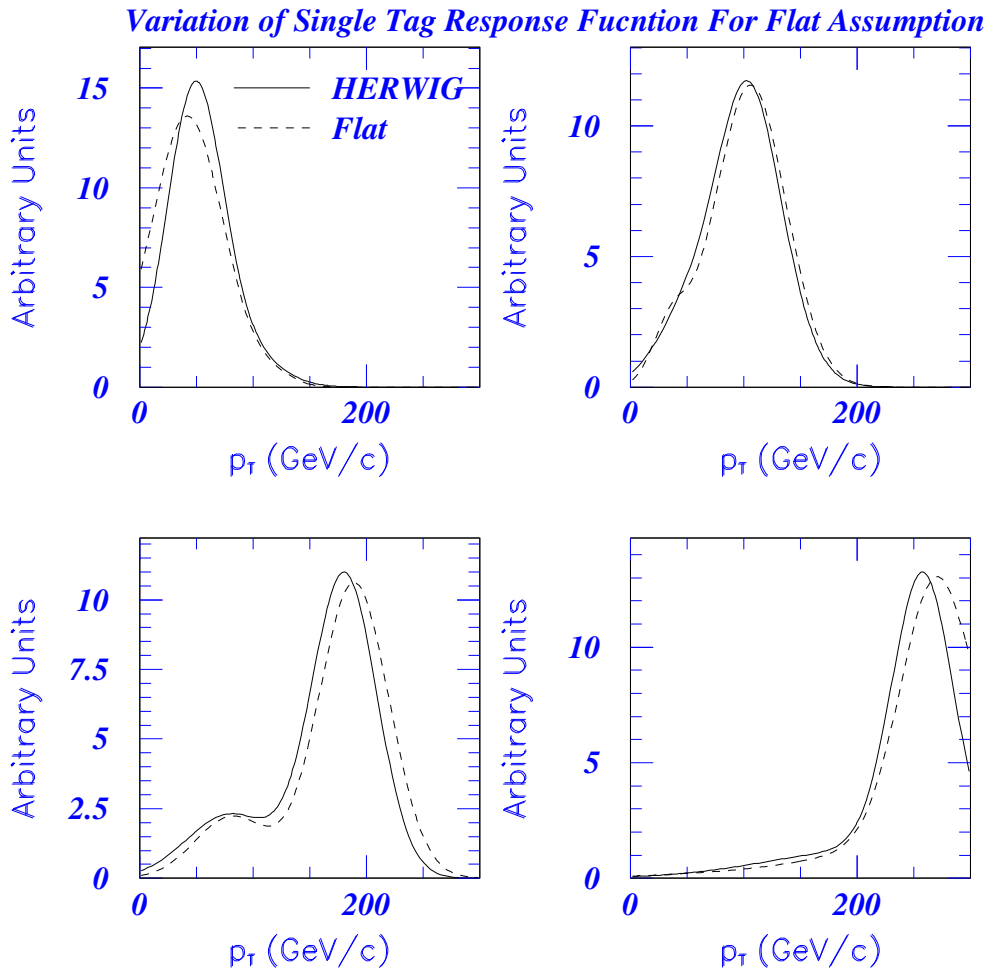

assumption about how the p_T distribution varies *across* the bin in question. For example, the response functions depicted in Fig. 4.7 are, in principle, only valid for the case where the p_T distribution is identical to the HERWIG predictions. Two questions then arise.

- Which assumption should we take to calculate the "central value"?
- How sensitive are our results to reasonable variations of this assumption?

The approach that we have decided upon relies on the data in order to estimate the shape of the true p_T distribution within each true p_T bin. We employ an iterative "bootstrap" procedure. First, using the measured distribution, we formulate an initial estimate for the the fraction of top quarks produced in each p_T bin. Using this, we form an estimate for the shape of the true p_T distribution across each bin by linearly interpolating between the smeared data points, as depicted in Fig. 5.3.

Using this estimate for the shape of the true p_T distribution, we draw 5000 Monte Carlo events in each bin of true p_T. A rejection algorithm ensures that the true p_T is distributed as shown in Fig. 5.3. The response functions for the untagged and tagged samples are calculated separately. The data distribution in each tagging subsample is then used to construct the log likelihood function:

$$-\ln[\mathcal{L}] = \sum_{i=1}^{n_{data}} \left(-\ln \left[(1-B) \sum_{j=1}^{n_{bin}} R_j T_j(p_T^i) + BV(p_T^i) \right] \right) + \frac{(B-\mu_b)^2}{2\sigma^2(\mu_b)}, \qquad (5.2)$$

where

- R_i is the fraction of top quarks produced in true bin i,
- B is the background fraction in the tagging subsample under consideration,
- the T_k, V are the response functions for the signal and background respectively, and
- $\mu_b \pm \sigma(\mu_b)$ is the estimated background fraction within a given tagging subsample.

The signal ($T(p_T)$) and background ($V(p_T)$) response functions are normalized to unity.

Figure 5.3: The linear approximation used in order to estimate the true p_T distribution from the data. The data points shown here are the raw values returned from the MINUIT mass fitter.

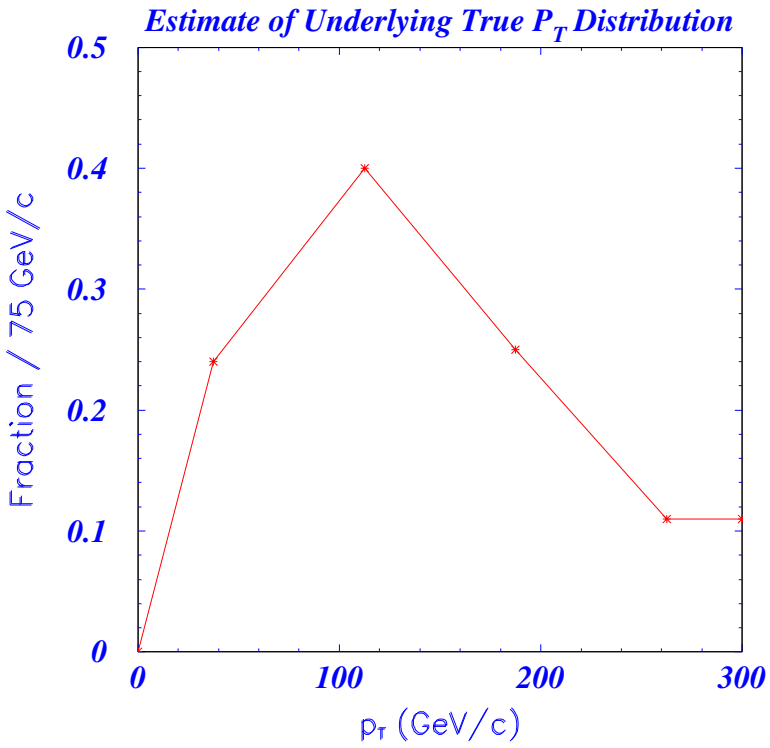

The alert reader will note that the R_i's cannot all be free parameters since they must sum to unity. The maximization procedure must proceed subject to the following two constraints:

$$R_i \in [0,1] \text{ and } \sum_{i=1}^{4} R_i = 1 \ . \tag{5.3}$$

The first constraint can be readily incorporated into a minimization procedure. However, the second is more problematic. If we replace, for example, R_1 by $1 - R_2 - R_3 - R_4$ in the minimization procedure, then we are left with the problem of imposing the linear constraint $1 - R_2 - R_3 - R_4 \geq 0$. It is this consideration that leads us to an alternate parameterization

Table 5.6: The parameterization used in the fit. This provides a natural way to fit to the fractions in each true p_T bin subject to the physical constraints.

True Bin	Fraction
$0 < p_T < 75$	$R_1 = \xi_1$
$75 < p_T < 150$	$R_2 = (1-\xi_1)\xi_2$
$150 < p_T < 225$	$R_3 = (1-\xi_1)(1-\xi_2)\xi_3$
$225 < p_T < 300$	$R_4 = (1-\xi_1)(1-\xi_2)(1-\xi_3)$

shown in Table 5.6, where we introduce three new parameters $\xi_i,\ i = 1,2,3$ that are constrained to lie between 0 and 1.

We then maximize $\ln(\mathcal{L})$ using the MINUIT library by varying the ξ_i. This gives us an estimate of the R_i's and hence the true p_T distribution. We then use the results of our fit as our initial guess for subsequent iterations of the bootstrap procedure. We define the termination point of the algorithm as the point at which the condition

$$\frac{\xi_i^{\text{new}} - \xi_i^{\text{old}}}{\delta_{\xi_i}} \leq 0.1, \tag{5.4}$$

is satisfied for each ξ_i, where $\xi_i^{\text{new}}(\xi_i^{\text{old}})$ is the value of ξ_i in the current(previous) iteration of the procedure, and δ_{ξ_i} is the statistical uncertainty (provided by MIGRAD). Asymmetric MINOS errors are used for the final uncertainty calculations. MINOS[60], operates after a minimum has been found, and calculates parameter uncertainties taking into account both parameter correlations and non-linearities. The algorithm proceeds by varying one parameter away from the minimum, and re-maximizing the likelihood with respect to the other two ξ_i's. By shuffling the rows in Table 5.6 so that a different R_i corresponds to ξ_1, we compute these uncertainty estimates for each of the four R_i's.

5.4 Checks of Methodology

We have performed Monte Carlo experiments in order to verify our methodology. These involve selecting random samples of 61 events from our standard HERWIG Monte Carlo

samples. Each of these samples contains 29 events with b-tags and 32 events with no tags. The background fraction in each of the two tagging subsamples is allowed to fluctuate around our the background estimates presented in Table 5.4 in a manner consistent with the uncertainties in these fractions. We draw the number of a background events from a Gaussian probability distribution with a width equal to the uncertainty in the estimate.

Due to the fact that our bootstrap algorithm is rather CPU-intensive, we have decided to use a simplified version of our unsmearing procedure in performing some of the checks on the likelihood fit's inherent robustness. We choose to not vary the shape of the underlying p_T distribution, which allows us to employ double-Gaussian fits of the type shown in Fig. 4.7 in our likelihood fit. These response functions are calculated under the assumption that the variation of the p_T distribution within each bin is as predicted by the Standard Model. This requires orders of magnitude less CPU than does the process of constructing our response functions via rejection against an arbitrary p_T distribution. Here we check only the basic principles of our methodology; later we shall assign a systematic error to take into account the fact that our bootstrap technique may not get the underlying assumption correct.

For R_1, R_2, and R_3, it makes sense to fit the error distributions to single Gaussian functions. These plots are shown in Figs. 5.4-5.6. Only the resolution function for R_3 shows any significant deviation from the expected Gaussian distribution with unit width. About 4% of the Monte Carlo experiments contribute to the long negative tail in the distribution. In order to understand why the algorithm fails to make a reasonable error estimate in these cases, we make a plot of the resolution function for the subset of Monte Carlo experiments with $R_3 > 10^{-8}$ in Fig. 5.7. In this plot we see acceptable agreement with the unit Gaussian hypothesis. This indicates that in the small subset of the Monte Carlo experiments where the fit converges to $R_3 = 0$, the fit's statistical uncertainty estimate fails to produce accurate estimates of the uncertainty on R_3. In the fit to the data, however, we are operating in a region where R_3 is far from zero. In this region, Fig. 5.7 indicates that the fit is indeed operating properly.

For R_4, we are basically limited to placing an upper limit on the distribution. It is the

Figure 5.4: The resolution function for R_1 in the Monte Carlo experiments described in Section 5.4. Superimposed is a fit to a Gaussian distribution.

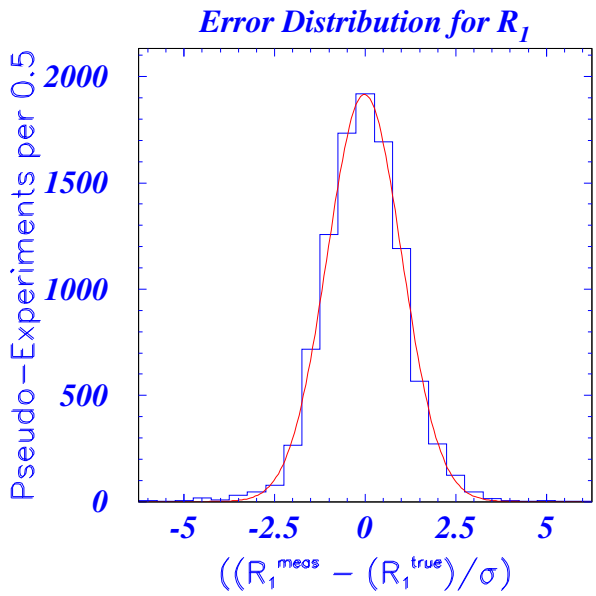

validity of this upper limit in which we are interested. We examined the one sided resolution function,

$$\frac{R_4^{\rm meas} - R_4^{\rm true}}{\sigma^+}, \tag{5.5}$$

and proceeded to count the number of events that fall above 1 standard deviation in the positive direction. We expect roughly $50 \times 0.32 = 16\%$ of the events to be above the 1σ upper limit. We observe 17.9%. Thus, we conclude that our upper uncertainty provides a reliable 82% confidence level upper limit. The distribution of R_4 for our pseudo-experiments in plotted in Fig. 5.8. The structure in this distribution arises from the effect of small statistics in this sample. Three peaks are evident in the distribution, the first corresponding to that subset of pseudo-experiments where no events lie under the bulk of the R_4 response function, the second corresponding to one event, and the third corresponding to the rare case of three events.

Figure 5.5: The resolution function for R_2 in the Monte Carlo experiments described in Section 5.4. Superimposed is a fit to a Gaussian distribution.

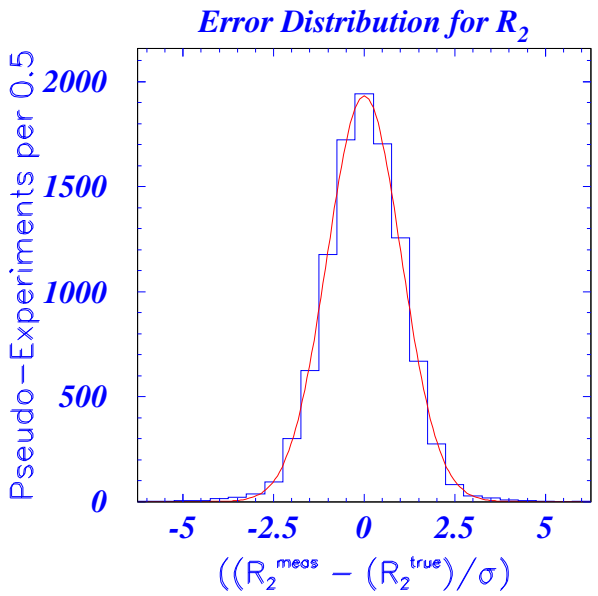

We conclude that our likelihood fit provides reliable confidence intervals.

5.5 Results

The smeared hadronically-decaying top quark p_T distribution for the events in our constrained-fit mass sample is shown in Fig. 5.9.

The bootstrap procedure described in Section 5.3 was applied to the data. The procedure converges on the third iteration over the data. We state the results, and their associated MINOS uncertainty estimates below:

$$B_0 = 0.64^{+0.11}_{-0.11} \tag{5.6}$$

$$B_1 = 0.29^{+0.05}_{-0.05} \tag{5.7}$$

$$R_1 = 0.18^{+0.19}_{-0.18} \tag{5.8}$$

Figure 5.6: The resolution function for R_3 in the Monte Carlo experiments described in Section 5.4. Superimposed is a fit to a Gaussian distribution.

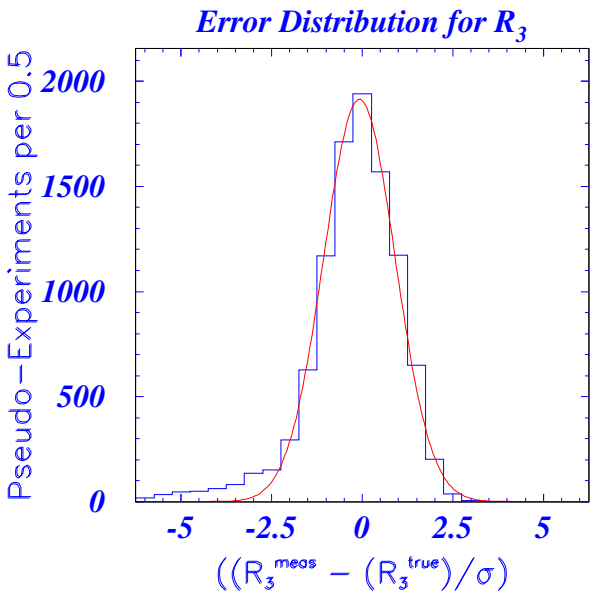

$$R_2 = 0.44^{+0.23}_{-0.22} \tag{5.9}$$

$$R_3 = 0.38^{+0.16}_{-0.13} \tag{5.10}$$

$$R_4 = 0.000^{+0.033}_{-0.000} \tag{5.11}$$

The R_i's are the true top quark fractions in each of the four 75 GeV/c p_T bins, B_0 is the fitted background fraction in the no-tag sample, and B_1 is the fitted background fraction in the subsample of our $t\bar{t}$ candidates that possess b-tags. The errors are statistical only.

5.6 Combining The first Two Bins

Due to the strong overlap in the response functions for the first two bins, it is reasonable to expect that the fit results will be strongly *anti*-correlated. Thus, we might expect to see a significant decrease in the fractional uncertainty in the cross sections for $p_t < 150$ GeV when these two bins are combined. The MINOS uncertainties are very close to the parabolic

Figure 5.7: The resolution function for R_3 in the Monte Carlo Experiments described in section 5.4. Only those events satisfying the cut $R_3 > 10^{-8}$ are plotted here. Superimposed is a fit to a Gaussian distribution.

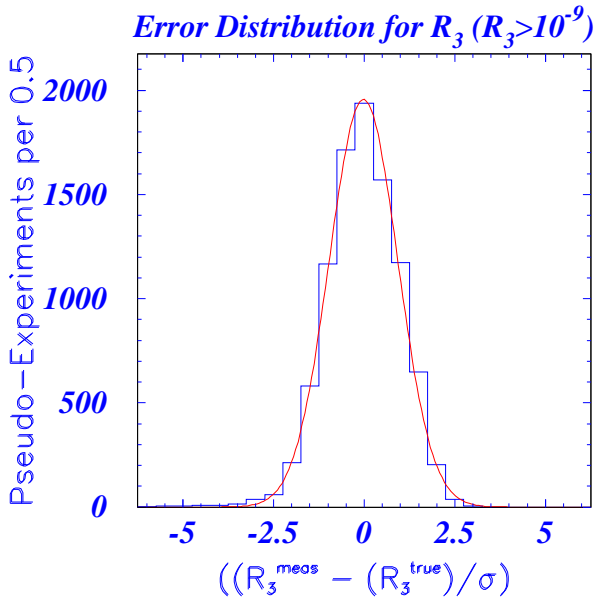

uncertainties for these two variables, indicating that the MIGRAD covariance matrix is a reliable representation of the correlations. This being the case, we can combine the first two bins by using the covariance matrix and standard error propagation[61].

The covariance matrix for ξ_1 and ξ_2 is

$$\mathrm{cov}(\xi_1, \xi_2) = \begin{pmatrix} 0.037 & -0.019 \\ -0.019 & 0.042 \end{pmatrix}. \tag{5.12}$$

We expect the error on $F = R_1 + R_2 = \xi_1 + (1 - \xi_1)\xi_2$ to be given by:

$$\sigma^2(F) = \left(\frac{\partial F}{\partial \xi_1}\right)^2 \mathrm{cov}_{1,1} + \left(\frac{\partial F}{\partial \xi_2}\right)^2 \mathrm{cov}_{2,2} + 2\left(\frac{\partial F}{\partial \xi_1}\frac{\partial F}{\partial \xi_2}\right)\mathrm{cov}_{1,2} \tag{5.13}$$

$$= (1-\xi_2)^2\mathrm{cov}_{1,1} + (1-\xi_1)^2\mathrm{cov}_{2,2} + 2(1-\xi_1)(1-\xi_2)\mathrm{cov}_{1,2}. \tag{5.14}$$

Performing the calculation, we obtain

$$R_1 + R_2 = 0.62 \pm 0.15. \tag{5.15}$$

Figure 5.8: The distribution of outcomes for R_4 in the Monte Carlo Experiments described in section 5.4.

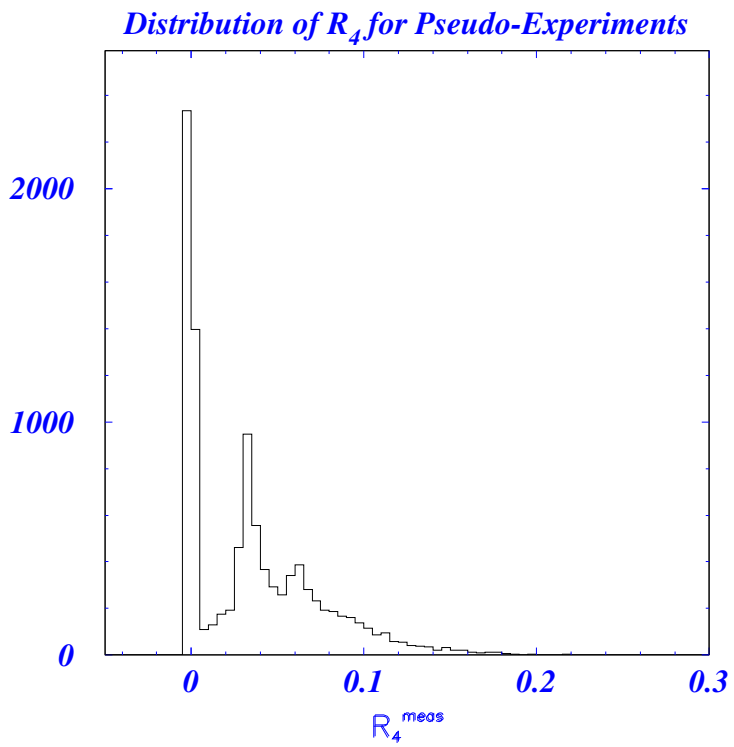

As expected, the fractional uncertainty on the sum $R_1 + R_2$ is much less than the fractional uncertainty on the individual estimates.

5.7 Acceptance Corrections

The result presented in the previous section is the p_T distribution corrected for the smearing effects introduced by our reconstruction technique. However, we need to understand what biases are introduced during event selection. That is, we need to examine the question of how the acceptance varies for each of our true p_T bins, and we must correct for this effect. We have measured the acceptance for $t\bar{t}$ production as a function of top quark p_T in HERWIG Monte Carlo samples by generating approximately 20000 events in each p_T bin and then

Figure 5.9: The p_T distribution for the hadronically-decaying top quarks in the constrained mass sample. The shaded distribution is the estimated background distribution, with the shape as predicted by VECBOS.

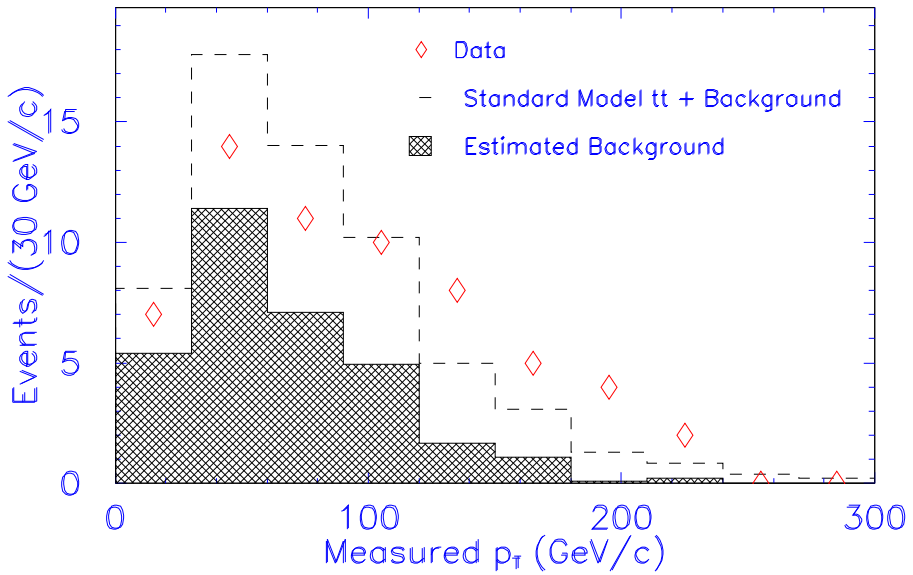

Table 5.7: Relative Acceptance results for the constrained mass sample in each true p_T bin. We include only statistical errors on the acceptance. The results are normalized to ϵ_1, the absolute acceptance in the first true p_T bin.

True Bin	Acceptance
$0 < p_T < 75$	1.00
$75 < p_T < 150$	1.16 ± 0.02
$150 < p_T < 225$	1.34 ± 0.02
$225 < p_T < 300$	1.24 ± 0.02

processing them with the CDF detector simulation. In Table 5.7, we show the results for the acceptance in each bin of true p_T. We use these results to re-scale the corrected results in the previous section, resulting in the corrected results, shown below.

$$R_1 = 0.21^{+0.22}_{-0.21} \quad (5.16)$$

$$R_2 = 0.45^{+0.23}_{-0.23} \quad (5.17)$$

$$R_3 = 0.34^{+0.14}_{-0.12} \quad (5.18)$$

$$R_4 = 0.000^{+0.031}_{-0.000} \quad (5.19)$$

$$R_1 + R_2 = 0.66^{+0.16}_{-0.16} \quad (5.20)$$

In the above, the uncertainties are statistical only.

5.8 Systematic Uncertainties

In the measurement of the top quark p_T distribution, systematic uncertainties can contribute in two different places. By modifying the response functions used to perform the unsmearing analysis described in the last chapter, they can introduce biases into the fit. Furthermore, they can change how the relative acceptance varies as a function of p_T.

We measure the systematic uncertainties in the fit by performing Monte Carlo pseudo-experiments of the type described in section 5.4, and computing the means of the outcomes of these pseudo-experiments after modifying one of the systematic effects in our Monte Carlo model. By comparing the means of the outcomes of these pseudo-experiments to the means of the outcomes of our default pseudo-experiments, we can estimate the bias introduced by various systematic effects. These effects include variation of the top quark mass, uncertainty in the jet energy scale, initial and final state radiation, and the shape of the true p_T distribution within each bin. Other sources of systematic uncertainty are negligible.

We also compute systematic uncertainties in the relative acceptance corrections described in Section 5.7, by recomputing the acceptance in each bin of true p_T after varying our Monte Carlo model to take into account a possible systematic variation. Due to the small size of the relative acceptance corrections, these effects are relatively minor.

We describe in the following Sections the measurement of the systematic uncertainties in

Table 5.8: The true values of the R_i's for the distributions depicted in Fig. 5.10.

Parameter	a)	b)	c)	d)
R_1^{true}	0.376	0.327	0.048	0.052
R_2^{true}	0.447	0.364	0.419	0.267
R_3^{true}	0.148	0.229	0.437	0.439
R_4^{true}	0.028	0.087	0.096	0.242

our unsmearing procedure. They include the variation of the shape of the true p_T spectrum within each bin, the modeling of the background p_T distribution, the jet energy scale, initial and final state radiation, and variation of the top quark mass.

5.8.1 Variation of the Shape of the p_T Spectrum

As we have noted in section 5.3, a potential bias in our technique results from the fact that our bootstrap technique does not perfectly extract the shape of the p_T distribution within each bin. Any discrepancy between the estimate of the shape of the p_T distribution within each bin given by the bootstrap technique and the actual p_T distribution will result in a bias. This bias results due to the fact that the response functions that we employ in order to perform the unsmearing are, at some level, a function of the true p_T distribution within each bin.

We use the true p_T distributions depicted in Fig. 5.10 in order to evaluate the magnitude of the resulting systematic uncertainty. The true values of the R_i's for each of these distributions are given in Table 5.8. We evaluate a systematic uncertainty by comparing the mean outcome of the pseudo-experiments to the true value of the R_i's in the distributions. This comparison is given in Table 5.9. Distribution a) is the Standard Model expectation and suffers little average bias. Distribution c), in particular, consistently causes significant bias for all all of the considered interpolation hypotheses. This is due to the depletion of events with low p_T and the strongly-peaked nature of the distribution.

Figure 5.10: The true p_T distributions that enter into our calculation of the systematic uncertainties on the residual bias in the methodology.

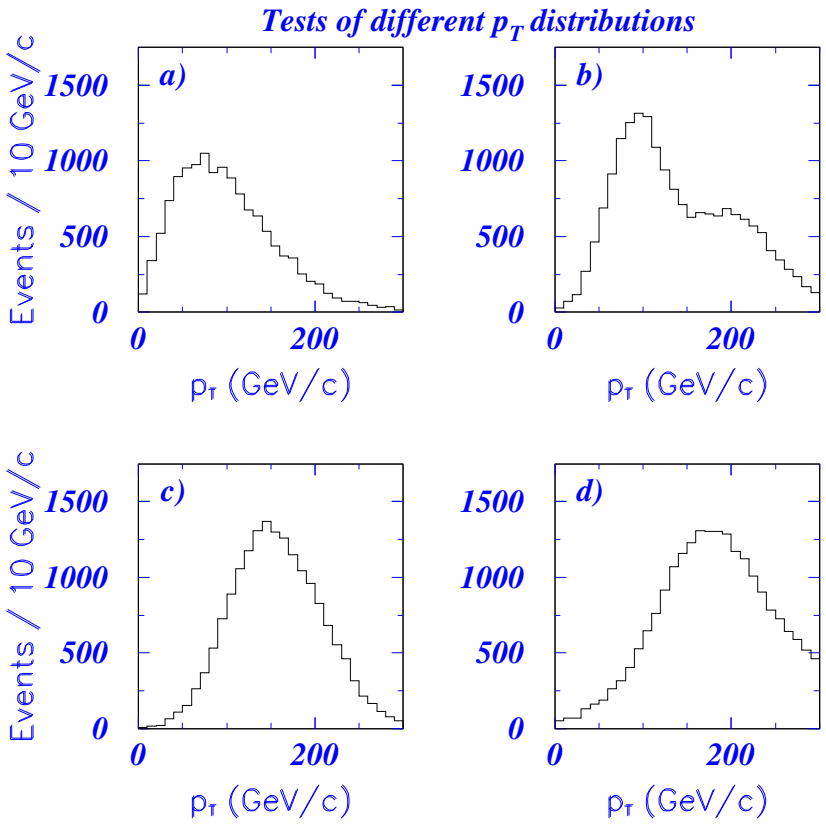

5.8.2 Variation of the Top Quark Mass

The Run I Tevatron top mass measurement for Run I is $m_t = 174.3 \pm 5.1$ GeV/c^2[40]. A systematic uncertainty stems from the fact that the kinematic fit constrains the decay products to come from a top quark mass of 175 GeV/c^2. In order to investigate biases that might be introduced by constraining the top mass to an incorrect value, we have run our analysis procedure on Monte Carlo datasets where $m_t = 170$ GeV/c^2 and $m_t = 180$ GeV/c^2. A small bias appears in the fit, causing the technique to underestimate R_1 and overestimate R_2 in both cases. The systematic error introduced by the variation of the top mass is both small and completely asymmetric.

Table 5.9: The residual bias for the distributions depicted in Fig. 5.10. This bias is evaluated by comparing the true values to the means of the outcomes in Monte Carlo pseudo experiments. The largest observed bias in each variable is taken as a symmetric systematic uncertainty in the measurement.

Parameter	a)	b)	c)	d)
$R_1^{\rm fit} - R_1^{\rm true}$	-0.011 ± 0.009	-0.037 ± 0.007	-0.026 ± 0.003	-0.018 ± 0.004
$R_2^{\rm fit} - R_2^{\rm true}$	$+0.011 \pm 0.010$	$+0.015 \pm 0.009$	$+0.003 \pm 0.008$	-0.027 ± 0.007
$R_3^{\rm fit} - R_3^{\rm true}$	-0.003 ± 0.005	$+0.018 \pm 0.008$	$+0.051 \pm 0.008$	$+0.040 \pm 0.008$
$R_4^{\rm fit} - R_4^{\rm true}$	$+0.002 \pm 0.002$	-0.006 ± 0.004	-0.021 ± 0.004	$+0.005 \pm 0.006$

Table 5.10: Residuals for our fitting technique as a function of m_t.

	$m_t = 175$ GeV/c^2	$m_t = 170$ GeV/c^2	$m_t = 180$ GeV/c^2
δR_1	-0.007	-0.026	-0.021
δR_2	+0.002	+0.015	+0.027
δR_3	-0.001	-0.005	-0.023
δR_4	+0.008	+0.018	+0.013
$\delta(R_1 + R_2)$	-0.005	-0.012	+0.006

We estimate our systematic uncertainties by comparing the means of the outcomes of our Monte Carlo pseudo-experiments to the true values for these three different top quark masses. In Table 5.10 are the residuals on the R_i's before they are corrected for acceptance effects. We take the largest observed deviation in each bin to be our estimate of the systematic uncertainty due to the uncertainty on the top quark mass.

5.8.3 Variation of the Background Shape

In order to estimate the uncertainty introduced in our calculation by our choice of models for the background shape, we have redone our likelihood fit using background events computed

using a QCD renormalization scale of $Q^2 = M_W^2$ instead of $Q^2 = \langle p_T \rangle^2$. The plots for the background shapes in the two cases are compared in Fig. 5.11. The deviations introduced by this modification are small. This was predictable, due to the obvious similarity between the background predictions at the two different renormalization scales. The variations in the R_i are

$$|\delta R_1| = 0.025, \tag{5.21}$$

$$|\delta R_2| = 0.008, \tag{5.22}$$

$$|\delta R_3| = 0.008, \tag{5.23}$$

$$|\delta R_4| = 0.010, \tag{5.24}$$

$$|\delta(R_1 + R_2)| = 0.016\ . \tag{5.25}$$

We take this uncertainty to be symmetric.

Furthermore, as was noted in Section 5.1, we have explored the shape of the non-W background in our data sample. This was done by selecting a sample of events that pass all of our selection criteria except for the fact that they fail the lepton isolation criteria. This so-called "non-isolated W sample" is expected to be enriched in the non-W background that are expected to make up approximately 30% of our final data sample. In Fig. 3.2, we compare the reconstructed p_T distributions for the two different VECBOS Q^2 scales with a third distribution composed of 30% non-isolated $W + 3.5$ jet data and 70% VECBOS Monte Carlo.

Since the magnitude of the variation in the shape of the background p_T spectrum upon addition of the expected amount of non-W background is similar to the variation obtained by varying the VECBOS Q^2 scale, we deem it superfluous to take an additional systematic uncertainty for this effect.

5.8.4 Jet Energy Scale

A systematic uncertainty arises due to the jet energy corrections. This uncertainty is the largest systematic uncertainty in the measurement of the top quark mass. Although the

Figure 5.11: Comparison of the background p_T distribution predicted by VECBOS for two different renormalization scales.

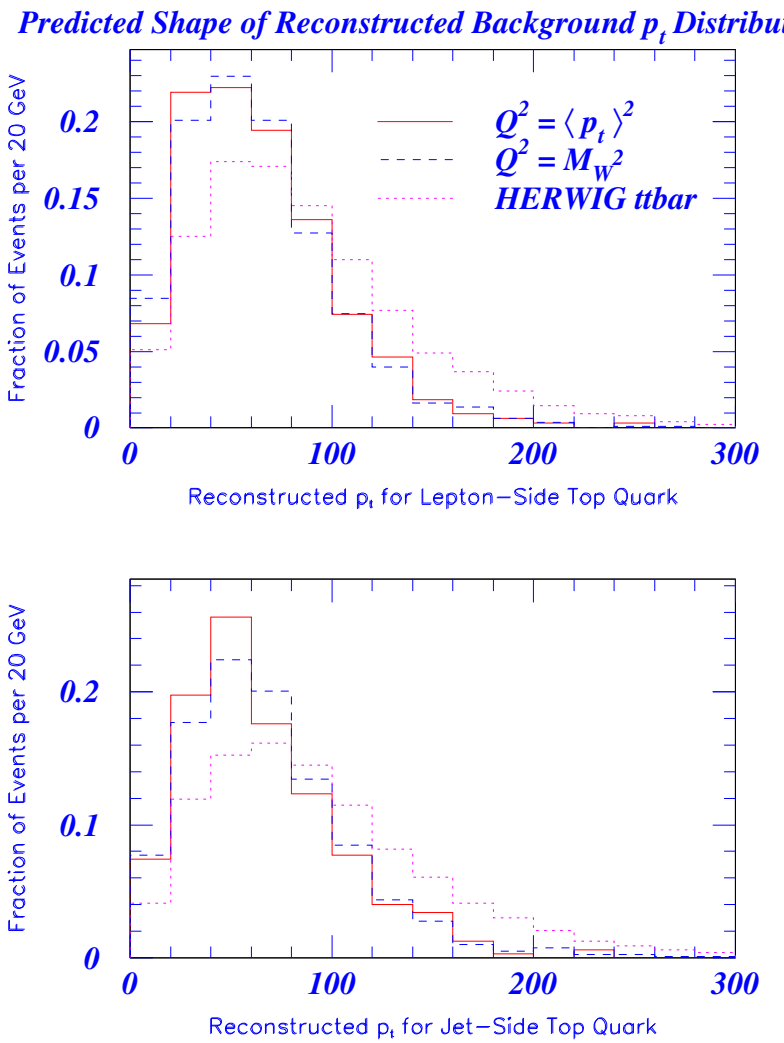

mass-constrained kinematic fit used in the current analysis lowers our sensitivity to the initial jet energies, this uncertainty still produces a measurable effect. There are four principle contributions to this uncertainty:

- the stability of the calorimeter response over the course of Run I,
- the uncertainty in the absolute jet energy correction,
- soft gluon radiation, that covers uncertainties on the out of cone corrections, from $R = 0.4$ to $R = 1.0$, and
- an uncertainty on the out-of-cone corrections for $R > 1$.

In order to determine the potential bias due to a shift in the jet energy scale we perform pseudo-experiments on samples where the jet energy scale has been changed within its uncertainties. The shifts due to calorimeter stability and the absolute jet energy correction are combined. The means of the outcomes of the shifted pseudo-experiments are compared to the means in the case of the default energy scale. These shifts are presented in Table 5.11.

In the cases where the different shifts introduce a bias in the same direction, we add the various systematic uncertainties in quadrature in order to obtain a combined shift. One can see that the uncertainty is almost completely asymmetric. This is due to the fact that the primary effect of the shift in the absolute jet energy scale is to increase the fraction of parton assignments that are missed.

The largest deviation in a particular direction is taken as a systematic uncertainty.

We neglect any correlations between the uncertainties in the top quark mass and the jet energy scale. This is due to the fact that the shift in the world-average top quark mass due to the variation in the CDF calorimeter energy scale is small. Monte Carlo studies where both the absolute energy scale and the top quark mass are shifted demonstrate that this assumption is reasonable.

Table 5.11: The mean measured values of the $R_i's$ as a function of the jet energy scale. The three different effects are evaluated separately and the resulting shifts are added in quadrature.

	R_1	R_2	R_3	R_4
Default	0.371	0.450	0.146	0.0323
Absolute Energy Scale(+)	0.344	0.466	0.146	0.0432
Absolute Energy Scale(−)	0.374	0.464	0.121	0.0382
Soft Gluon Radiation(+)	0.342	0.479	0.138	0.0407
Soft Gluon Radiation(−)	0.386	0.446	0.128	0.0369
$R > 1$ Corrections(+)	0.345	0.478	0.137	0.0399
$R > 1$ Corrections(−)	0.385	0.447	0.131	0.0377

Table 5.12: The systematic uncertainties due to variations in the jet energy scale. We compute the effect of both the bias introduced into the unsmearing procedure and the effects due to the change in relative acceptance between different p_T bins.

	δR_1	δR_2	δR_3	δR_4	$\delta(R_1 + R_2)$
Jet Energy Scale Increased (Bias)	0.047	-0.043	0.012	-0.016	$^{+0.011}_{-0.002}$
Jet Energy Scale Decreased (Bias)	-0.020	$^{+0.005}_{-0.016}$	0.032	-0.009	-0.023
Jet Energy Scale Uncertainty	$^{+0.047}_{-0.020}$	$^{+0.005}_{-0.043}$	$^{+0.032}_{-0.000}$	$^{+0.000}_{-0.016}$	$^{+0.011}_{-0.023}$

5.8.5 Initial State Radiation

We face the possibility that there could be an anomalous increase or reduction in the amount of actual initial state radiation, compared with our Monte Carlo calculations. This could be due to theoretical uncertainties in our Monte Carlo calculation or due to new physics. We can estimate a systematic uncertainty for the case where there is an anomalous reduction in the amount of ISR by performing Monte Carlo experiments on PYTHIA events without

Table 5.13: Mean variation in R_i as a function of the amount of initial state radiation. See text for an explanation of how the Monte Carlo models are varied.

	No ISR	Increased ISR
δR_1	-0.005	-0.016
δR_2	-0.002	+0.011
δR_3	+0.002	-0.005
δR_4	+0.005	+0.009
$\delta(R_1 + R_2)$	-0.007	+0.005

initial state radiation. We estimate the systematic uncertainty exactly as was done in the top mass analysis (ie: by multiplying the residual by 0.5). The results are presented in Table 5.13. The effect is seen to be negligible.

Another possible uncertainty is created if we assume that $t\bar{t}$ pairs are produced in association with another particle, i.e.

$$q\bar{q} \rightarrow t\bar{t}X \ . \tag{5.26}$$

This scenario would, in principle, result in an excess of events possessing large values of $p_T(t\bar{t})$. As one can see from Fig. 5.12, this could degrade the p_T resolution in the MINUIT mass fitter. This effect originates primarily from the presence of extra jets in the event, which in turn increases the likelihood that incorrect parton assignments can be made. This broadens the resolution function significantly.

In order to place limits on the number of extra jets in an event originating from anomalous amounts of initial state radiation, we consider the distribution of the number of jets for the events passing our selection criteria. The observed distribution can then be compared to the expected template for events having the Standard Model $p_T(t\bar{t})$ distribution as well as those having high $p_T(t\bar{t})$. We choose to define our "high" $p_T(t\bar{t})$ template by selecting events with $p_T(t\bar{t}) > 30$ GeV/c. These distributions are depicted in Fig. 5.13.

The agreement between the Standard Model prediction and the data is excellent. For a

Figure 5.12: A comparison of the p_T error distributions for events with a Standard Model $p_T(t\bar{t})$ distribution and the subset of events having $p_T(t\bar{t}) > 30$ GeV.

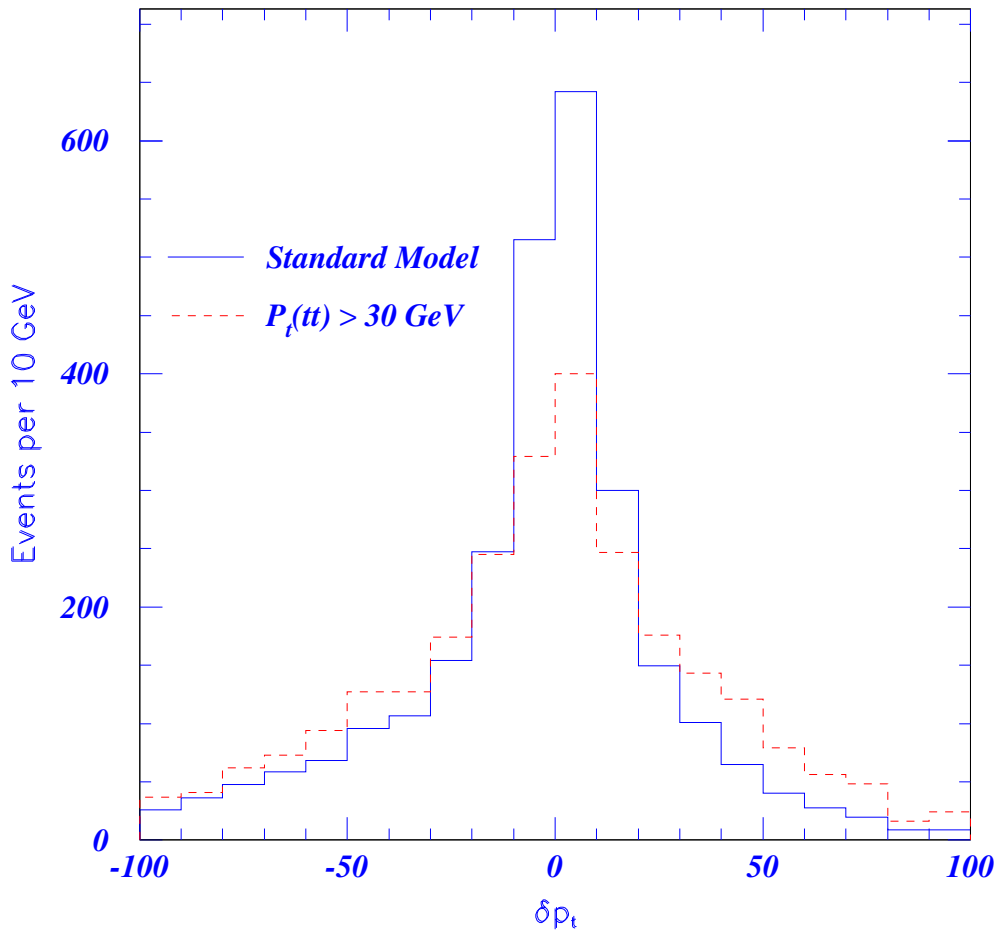

large increase in initial state radiation, we would expect an increase in the number of events in the 5-jet bin. We use this property of events with high $p_T(t\bar{t})$ in order to place limits on possible anomalous contributions to initial state radiation. We perform an unbinned likelihood fit to the data, using the two Monte Carlo distributions depicted in Fig. 5.13 as templates. We also use a VECBOS template, whose normalization is allowed to float in accordance with our background estimates. The fit prefers no anomalous contribution to the extent that the coefficient on the $p_T(t\bar{t}) > 30$ GeV template converges to $0.00^{+0.15}_{-0.00}$.

Figure 5.13: A comparison of the N_{jet} distributions for events with a Standard Model $p_T(t\bar{t})$ distribution and the subset of events having $p_T(t\bar{t}) > 30$ GeV. VECBOS Monte Carlo, normalized to the expected background contribution, is added to take into account the W + jets background. We define a "jet" as having $E_T > 15$ GeV and $|\eta| < 2$.

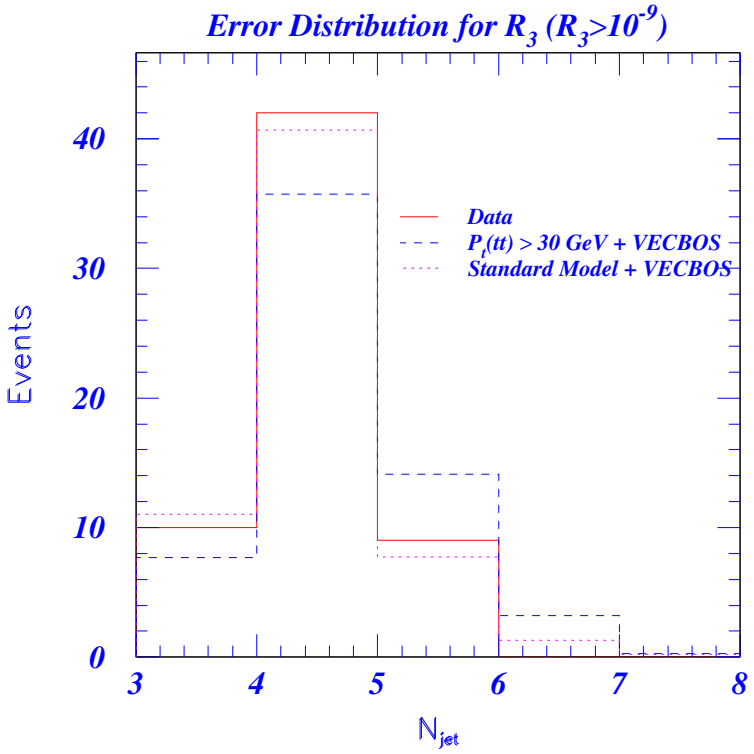

Allowing ourselves to be guided by this result, we consider Monte Carlo pseudo-experiments where a 15% contribution of events possessing $p_T(t\bar{t}) > 30$ GeV has been added to our standard Monte Carlo Samples. A small bias, presented in Table 5.13, becomes apparent. To be conservative, we assume a symmetric systematic uncertainty of this magnitude.

5.8.6 Final State Radiation

When evaluating the systematic uncertainty due to final state radiation, we continue to follow the procedures adopted in the measurement of the top quark mass[37]. In particular it

Table 5.14: Means of the Monte Carlo pseudo-experiments for the evaluation of the final state radiation systematic error. Half of the difference between the two cases is taken to be the symmetric systematic error.

	No ISR	No ISR, 4 Jets Match
$\langle R_1 \rangle$	0.367	0.292
$\langle R_2 \rangle$	0.451	0.496
$\langle R_3 \rangle$	0.146	0.165
$\langle R_4 \rangle$	0.038	0.049
$\langle R_1 + R_2 \rangle$	0.818	0.788

has been argued that a reasonable estimate of the uncertainty in the top mass measurement can be be calculated by considering the PYTHIA events with no initial state radiation. Although it is possible to generate PYTHIA events with no final state radiation, we have chosen not to follow this procedure. This is due to the fact that, in the absence of soft gluon radiation, events generated without any final state radiation will have significantly different shapes than those generated with final state radiation. This renders the jet energy corrections discussed in Section 4.1 invalid.

The reasoning that we employ is that if we compare PYTHIA events with no ISR for which the correct jet-parton assignments are made to the entire sample of no-ISR PYTHIA events, we can measure the magnitude of the bias introduce by a variation in final state radiation. Thus, we define our systematic error to be:

$$\delta R_i = 0.5(\text{PYTHIA(No ISR, 4 jets match)} - \text{PYTHIA(No ISR)}), \tag{5.27}$$

where PYTHIA(No ISR, 4 jets match) is the subset of PYTHIA events having exactly four jets, all of which are within $\Delta R < 0.4$ of a parton in (η, ϕ) space. We do not demand that the correct parton be matched. The means of the outcomes of the pseudo-experiments are presented in table 5.14.

Table 5.15: The computed relative acceptances for the different Monte Carlo samples. The parameter ϵ_1, the relative acceptance of the first bin, is defined to be 1. The central values of the R_i's have no sensitivity to the value of ϵ_4, due to the fact that the fit converges to zero in that bin.

	ϵ_1	ϵ_2	ϵ_3	ϵ_4
Central Values	1.00 ± 0.00	1.16 ± 0.01	1.34 ± 0.02	1.24 ± 0.04
Flat p_T Spectrum	1.00 ± 0.00	1.19 ± 0.05	1.33 ± 0.05	1.26 ± 0.05
$m_t = 170$ GeV	1.00 ± 0.00	1.16 ± 0.02	1.36 ± 0.03	1.23 ± 0.05
$m_t = 180$ GeV	1.00 ± 0.00	1.14 ± 0.02	1.23 ± 0.03	1.32 ± 0.05
Jet Energy(+)	1.00 ± 0.00	1.16 ± 0.01	1.38 ± 0.02	1.34 ± 0.05
Jet Energy (-)	1.00 ± 0.00	1.18 ± 0.02	1.36 ± 0.03	1.20 ± 0.05
No Initial State Radiation	1.00 ± 0.00	1.20 ± 0.02	1.45 ± 0.04	1.41 ± 0.08

5.9 Systematic Uncertainties due to the Relative Acceptance

In Table 5.15, we present the relative acceptances measured in the Monte Carlo samples used to study our systematic uncertainties, including the PYTHIA samples with no initial state radiation. In addition to this, we have increased the Monte Carlo statistics available for measuring each of these effects. Since the fit to the data converges to $R_4 = 0$, the relative acceptance of the fourth p_T bin, ϵ_4, only affects the scaling of the uncertainties on R_4.

In Table 5.15, the "Central Values" are the default values used to correct our measured results. They are computed using standard HERWIG Monte Carlo samples. The "flat p_T spectrum" result is the relative acceptance calculated for a sample of HERWIG Monte Carlo events having a flat true p_T distribution. We also compute the relative acceptance using Monte Carlo events having top quarks masses of $m_t = 170$ GeV and $m_t = 180$ GeV. The entries labelled "jet energy ($\pm$)" are the relative acceptance calculated using Monte Carlo samples where the energy scale has been shifted either up or down by the total uncertainty

Table 5.16: The systematic uncertainties due to the variation of the top quark mass. We compute the effect of both the bias introduced into the unsmearing procedure and the effects due to the change in relative acceptance between different p_T bins. There is no significant acceptance uncertainty in the case of a 170 GeV top quark mass.

	δR_1	δR_2	δR_3	δR_4	$\delta(R_1 + R_2)$
170 GeV Top Quark Mass (Bias)	0.026	-0.016	0.005	-0.018	0.010
180 GeV Top Quark Mass (Bias)	0.021	-0.027	0.023	-0.013	-0.06
180 GeV Top Quark Mass (Acceptance)	-0.009	-0.006	0.014	0.000	-0.14
Top Mass Uncertainty	$^{+0.026}_{-0.009}$	$^{+0.000}_{-0.033}$	$^{+0.037}_{-0.013}$	$^{+0.000}_{-0.018}$	$^{+0.010}_{-0.020}$

in the jet energy scale. Finally, the relative acceptance is also computed for PYTHIA events having no initial state radiation.

One can see that the only significant shift occurs for the cases where $m_t = 180$ GeV and where ISR is turned off. We assign a systematic uncertainty in these two cases, as well as the systematic uncertainty associated with the model of final state radiation.

The uncertainties on the acceptance and those due to any bias introduced into the fit are correlated. Indeed, if a particular systematic effect is present, then both of these shifts will occur simultaneously. In order to take this into account we add the uncertainties due to these two effects linearly and then add the net uncertainties due to the different systematic effects in quadrature. In the case of asymmetric shifts, such as the jet energy scale uncertainty, we add the uncertainties linearly to arrive at conservative estimates. For example, we take the combined uncertainty of $^{+0.050}_{-0.000}$ and $^{+0.000}_{-0.010}$ to be $^{+0.050}_{-0.010}$, not $^{+0.040}_{-0.000}$. Similarly, we take the combined uncertainty of $^{+0.030}_{-0.000}$ and $^{+0.030}_{-0.000}$ to be $^{+0.060}_{-0.000}$.

We have also computed the acceptance effects due to variations in the amount of QCD radiation. We have estimated the magnitude of this effect by computing the relative acceptance corrections for PYTHIA Monte Carlo samples with no initial state radiation. For the initial state radiation uncertainty we multiply the magnitude of the shift by 0.5, as was

Table 5.17: The systematic uncertainties due to the uncertainty in the model of initial and final state radiation. All uncertainties are taken to be symmetric. Within the statistical power of our Monte Carlo samples, final state radiation has no significant effect on the relative acceptance.

	δR_1	δR_2	δR_3	δR_4	$\delta(R_1 + R_2)$
Initial State Radiation (Bias)	0.016	0.011	0.005	0.009	0.005
Initial State Radiation (Acceptance)	0.006	0.000	0.006	0.000	0.006
Final State Radiation (Bias)	0.037	0.022	0.009	0.005	0.015
Net ISR Uncertainty	$\pm$0.022	$\pm$0.011	$\pm$0.011	$\pm$0.009	$\pm$0.011
Net FSR Uncertainty	$\pm$0.037	$\pm$0.022	$\pm$0.009	$\pm$0.005	$\pm$0.015

done when computing the uncertainty due to bias in the fit. For the final state radiation uncertainty, we compute the difference in in our results using the acceptance values calculated for events having no ISR to that calculated using events having no ISR, exactly four jets and all parton assignments made correctly. The effect is found to be negligible. The results are presented in Table 5.17.

We present a summary of the systematic uncertainties in Table 5.18.

5.10 Setting a 95% C.L. Upper Limit

As was mentioned in the introduction, there are several models of anomalous top quark production that could result in an enhancement in high-p_T top quark production. Thus, we find it desirable to place a 95% confidence level upper limit on R_4, our measurement of the fraction of top quarks produced with $p_T > 225$ GeV/c.

We have calculated our 95% confidence level upper limit on R_4 by employing a Bayesian statistical technique. In order to take into account our systematic uncertainties, we first convolve our likelihood with a Gaussian distribution, G, whose width is the total systematic

Table 5.18: Summary of Systematic Uncertainties.

Systematic Effect	δR_1	δR_2	δR_3	δR_4	$\delta(R_1+R_2)$
m_t	$^{+0.026}_{-0.009}$	$^{+0.000}_{-0.033}$	$^{+0.037}_{-0.013}$	$^{+0.000}_{-0.018}$	$^{+0.010}_{-0.020}$
Initial State Radiation	± 0.022	± 0.011	± 0.011	± 0.009	± 0.011
Final State Radiation	± 0.037	± 0.022	± 0.009	± 0.005	± 0.015
Jet Energy Scale	$^{+0.047}_{-0.020}$	$^{+0.005}_{-0.043}$	$^{+0.032}_{-0.000}$	$^{+0.000}_{-0.016}$	$^{+0.011}_{-0.023}$
Background Model	± 0.025	± 0.008	± 0.008	± 0.010	± 0.017
Shape of p_T Spectrum	± 0.037	± 0.027	± 0.051	± 0.021	± 0.045

uncertainty in R_4. In order to take into account the variation of the systematic uncertainty as a function of R_4, we have re-measured these biases at a nominal value close to the resulting upper limit, namely $R_4 = 0.15$. The total systematic uncertainty in R_4 is measured to be $^{+0.038}_{-0.024}$ at $R_4 = 0.15$. This is to be compared to the systematic uncertainty of $^{+0.029}_{-0.029}$ at $R_4 = 0.10$.

Our smeared likelihood function is:

$$\mathcal{L}'(R_4^{\rm true}) = \int_0^1 \mathcal{L}(x) G(x, R_4^{\rm true}) dx \ . \tag{5.28}$$

Thus, the 95% C.L. upper limit on $R_4^{\rm true}$, R_4^{95}, is defined by

$$\int_0^{R_4^{95}} \mathcal{L}'(x) dx = 0.95 \int_0^1 \mathcal{L}'(x) dx \ . \tag{5.29}$$

The resulting upper limit on R_4 is

$$R_4 < 0.16 \text{ at } 95\% \text{ C.L.} \tag{5.30}$$

Extreme p_T distributions and the Upper Limit on R_4

In the previous discussions, our iterative unsmearing methodology has been shown to be valid for a large variety of true p_T distributions. It has been argued that for certain carefully chosen (and unphysical) p_T distributions, our methodology would not be completely robust.

In order to provide a limit that is completely independent of the shape of the p_T distribution in the fourth p_T bin, we have evaluated our upper limit using a response function in the fourth p_T bin whose true p_T distribution consists of a delta function of events having true hadronically-decaying top quark p_T at 225 GeV/c[3]. This results in a very conservative limit due to the fact that this particular choice of response function maximizes the overlap of the fourth response function with the data.

The upper limit, when calculated with this technique, rises to:

$$R_4 < 0.19 \text{ (at 95\% C.L.)} \tag{5.31}$$

However, we feel that the limit of 0.16 is applicable in all cases that have been considered in the existing theoretical literature on anomalous top quark production and is the appropriate results to quote from our analysis.

5.11 High p_T Acceptance

We have investigated the validity of extending our upper limit on R_4 beyond 300 GeV/c. In order to place limits on production in this regime, it is necessary to understand how our p_T resolution and acceptance vary as a function of p_T.

In Fig. 5.14, we plot the response functions for top quarks produced in the high-p_T region. It can be seen from this figure that the probability of observing top quark events possessing measured $p_T < 225$ GeV/c steadily decreases as the true p_T of the top quark increases. The highest reconstructed p_T in the data is 225 GeV/c.

This allows us to extend our limit to the region $p_T > 300$ GeV/c by using the following argument. The bootstrap technique prefers no top quark production with true $p_T > 260$ GeV/c. Nevertheless, suppose that we forced our likelihood fit to take into account such a high-p_T component. The effect of forcing the R_4 response function to have some contribution from this region of true p_T will be to shift some of the area under this response function to higher measured p_T (ie: away from the data). Thus, we can estimate the

[3]In practice, this is a rectangle between 225 and 235 GeV/c

Figure 5.14: Plots of the reconstructed p_T distribution in each of four true p_T bins. This plot includes only the hadronically-decaying top quarks. The Monte Carlo statistics of the standard HERWIG sample have been supplemented at high p_T by additional PYTHIA Monte Carlo production in the high p_T regime.

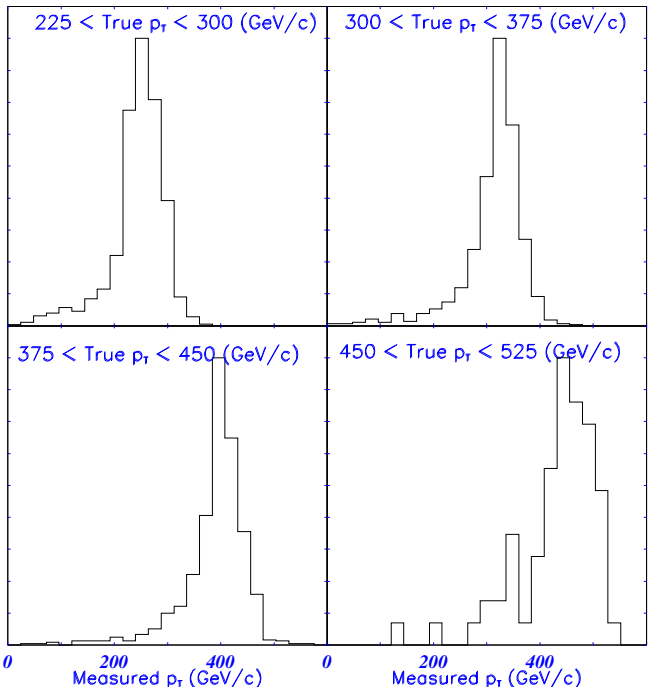

effect of a bootstrap technique that incorporates a contribution from true $p_T > 300$ GeV/c by simply reducing the area of the R_4 response function in the fit. This will result in a smaller upper limit on R_4, and we have verified that this is indeed the case. Thus, we conclude that our upper limit on R_4, which is formally an upper limit on top quark production with $p_T \in [225, 300]$ is indeed an upper limit on top quark production above 225 GeV/c.

The argument presented above has been verified by explicitly adding a high-p_T component of various magnitudes to the R_4 response function, and calculating the upper limit using this response function in the fit to the data. No indication of a possible high-p_T component has been observed.

The question of how high this upper limit may be extended has also been investigated. The PYTHIA Monte Carlo generator has been employed to generate high-p_T samples. To

within the statistical power of our Monte Carlo samples, the acceptance for the region between 300 GeV/c and 330 GeV/c is the same as the acceptance between 225 GeV/c and 300 GeV/c. The acceptance falls, primarily due to jet merging, as the p_T increases to even higher values. To investigate this effect, in Fig. 5.15 we plot the ratio of the generated p_T distribution to the p_T distribution of those events that pass our selection criteria. From this figure, we conclude that the acceptance falls off only slightly between 300 and 425 GeV/c. In terms of our upper limit, this falloff in acceptance is more than compensated for by the reduction in the magnitude of the response functions underneath the data as one moves into the region above 300 GeV/c. We conclude that our upper limit is valid out to at least 425 GeV/c, and state it as a limit on top quark production between 225 and 425 GeV/c.

Figure 5.15: A study of the acceptance above 300 GeV/c. We present here the ration between the GENP p_T distribution of events passing our selection criteria to the GENP p_T distribution of all events. The relative acceptance between 300 and 330 GeV/c is approximately the same as in the region between 225 and 300 GeV/c.

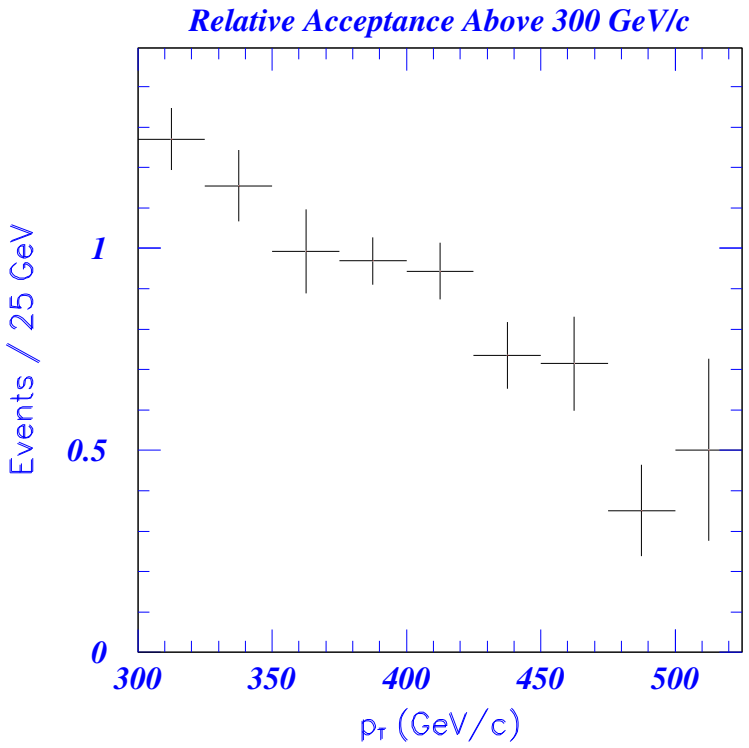

Chapter 6

Conclusions

In summary, we have made the first measurement of the top quark p_T distribution. This measurement was performed at a multi-purpose collider detector using $t\bar{t}$ pairs produced in $p\bar{p}$ collisions at $\sqrt{s} = 1.8$ TeV. The results are presented in Table 6.1, where they are compared to the Standard Model predictions[1]. We have used a likelihood technique to correct for biases introduced due to reconstruction and resolution effects. We have also computed a 95% confidence level upper limit on the fraction of top quarks that are produced with $225 < p_T < 425$ GeV/c, and find this fraction (referred to as "R_4"), to be less than 0.16 at 95% C.L.

[1] These predictions are generated using the HERWIG Monte Carlo generator.

Table 6.1: The results of our measurement of the top quark p_T distribution. The Standard Model expectation is generated using the HERWIG Monte Carlo program.

p_T Bin	Parameter	Measurement	Standard Model Expectation
$0 \leq p_T < 75$ GeV/c	R_1	$0.21^{+0.22}_{-0.21}(\text{stat})^{+0.10}_{-0.08}(\text{syst})$	0.41
$75 \leq p_T < 150$ GeV/c	R_2	$0.45^{+0.23}_{-0.23}(\text{stat})^{+0.04}_{-0.07}(\text{syst})$	0.43
$150 \leq p_T < 225$ GeV/c	R_3	$0.34^{+0.14}_{-0.12}(\text{stat})^{+0.07}_{-0.05}(\text{syst})$	0.13
$225 \leq p_T < 300$ GeV/c	R_4	$0.000^{+0.031}_{-0.000}(\text{stat})^{+0.024}_{-0.000}(\text{syst})$	0.025
$0 \leq p_T < 150$ GeV/c	$R_1 + R_2$	$0.66^{+0.17}_{-0.17}(\text{stat})^{+0.07}_{-0.07}(\text{syst})$	0.84

Appendix A

The CDF Collaboration

T. Affolder,[21] H. Akimoto,[43] A. Akopian,[36] M. G. Albrow,[10] P. Amaral,[7] S. R. Amendolia,[32] D. Amidei,[24] K. Anikeev,[22] J. Antos,[1] G. Apollinari,[10] T. Arisawa,[43] T. Asakawa,[41] W. Ashmanskas,[7] M. Atac,[10] F. Azfar,[29] P. Azzi-Bacchetta,[30] N. Bacchetta,[30] M. W. Bailey,[26] S. Bailey,[14] P. de Barbaro,[35] A. Barbaro-Galtieri,[21] V. E. Barnes,[34] B. A. Barnett,[17] M. Barone,[12] G. Bauer,[22] F. Bedeschi,[32] S. Belforte,[40] G. Bellettini,[32] J. Bellinger,[44] D. Benjamin,[9] J. Bensinger,[4] A. Beretvas,[10] J. P. Berge,[10] J. Berryhill,[7] B. Bevensee,[31] A. Bhatti,[36] M. Binkley,[10] D. Bisello,[30] R. E. Blair,[2] C. Blocker,[4] K. Bloom,[24] B. Blumenfeld,[17] S. R. Blusk,[35] A. Bocci,[32] A. Bodek,[35] W. Bokhari,[31] G. Bolla,[34] Y. Bonushkin,[5] D. Bortoletto,[34] J. Boudreau,[33] A. Brandl,[26] S. van den Brink,[17] C. Bromberg,[25] M. Brozovic,[9] N. Bruner,[26] E. Buckley-Geer,[10] J. Budagov,[8] H. S. Budd,[35] K. Burkett,[14] G. Busetto,[30] A. Byon-Wagner,[10] K. L. Byrum,[2] P. Calafiura,[21] M. Campbell,[24] W. Carithers,[21] J. Carlson,[24] D. Carlsmith,[44] J. Cassada,[35] A. Castro,[30] D. Cauz,[40] A. Cerri,[32] A. W. Chan,[1] P. S. Chang,[1] P. T. Chang,[1] J. Chapman,[24] C. Chen,[31] Y. C. Chen,[1] M. -T. Cheng,[1] M. Chertok,[38] G. Chiarelli,[32] I. Chirikov-Zorin,[8] G. Chlachidze,[8] F. Chlebana,[10] L. Christofek,[16] M. L. Chu,[1] C. I. Ciobanu,[27] A. G. Clark,[13] A. Connolly,[21] J. Conway,[37] J. Cooper,[10] M. Cordelli,[12] J. Cranshaw,[39] D. Cronin-Hennessy,[9] R. Cropp,[23] R. Culbertson,[7] D. Dagenhart,[42] F. DeJongh,[10] S. Dell'Agnello,[12] M. Dell'Orso,[32] R. Demina,[10] L. Demortier,[36] M. Deninno,[3] P. F. Derwent,[10] T. Devlin,[37]

J. R. Dittmann,[10] S. Donati,[32] J. Done,[38] T. Dorigo,[14] N. Eddy,[16] K. Einsweiler,[21] J. E. Elias,[10] E. Engels, Jr.,[33] W. Erdmann,[10] D. Errede,[16] S. Errede,[16] Q. Fan,[35] R. G. Feild,[45] C. Ferretti,[32] R. D. Field,[11] I. Fiori,[3] B. Flaugher,[10] G. W. Foster,[10] M. Franklin,[14] J. Freeman,[10] J. Friedman,[22] Y. Fukui,[20] I. Furic,[22] S. Galeotti,[32] M. Gallinaro,[36] T. Gao,[31] M. Garcia-Sciveres,[21] A. F. Garfinkel,[34] P. Gatti,[30] C. Gay,[45] S. Geer,[10] D. W. Gerdes,[24] P. Giannetti,[32] P. Giromini,[12] V. Glagolev,[8] M. Gold,[26] J. Goldstein,[10] A. Gordon,[14] A. T. Goshaw,[9] Y. Gotra,[33] K. Goulianos,[36] C. Green,[34] L. Groer,[37] C. Grosso-Pilcher,[7] M. Guenther,[34] G. Guillian,[24] J. Guimaraes da Costa,[14] R. S. Guo,[1] R. M. Haas,[11] C. Haber,[21] E. Hafen,[22] S. R. Hahn,[10] C. Hall,[14] T. Handa,[15] R. Handler,[44] W. Hao,[39] F. Happacher,[12] K. Hara,[41] A. D. Hardman,[34] R. M. Harris,[10] F. Hartmann,[18] K. Hatakeyama,[36] J. Hauser,[5] J. Heinrich,[31] A. Heiss,[18] M. Herndon,[17] B. Hinrichsen,[23] K. D. Hoffman,[34] C. Holck,[31] R. Hollebeek,[31] L. Holloway,[16] R. Hughes,[27] J. Huston,[25] J. Huth,[14] H. Ikeda,[41] J. Incandela,[10] G. Introzzi,[32] J. Iwai,[43] Y. Iwata,[15] E. James,[24] H. Jensen,[10] M. Jones,[31] U. Joshi,[10] H. Kambara,[13] T. Kamon,[38] T. Kaneko,[41] K. Karr,[42] H. Kasha,[45] Y. Kato,[28] T. A. Keaffaber,[34] K. Kelley,[22] M. Kelly,[24] R. D. Kennedy,[10] R. Kephart,[10] D. Khazins,[9] T. Kikuchi,[41] B. Kilminster,[35] M. Kirby,[9] M. Kirk,[4] B. J. Kim,[19] D. H. Kim,[19] H. S. Kim,[16] M. J. Kim,[19] S. H. Kim,[41] Y. K. Kim,[21] L. Kirsch,[4] S. Klimenko,[11] P. Koehn,[27] A. Köngeter,[18] K. Kondo,[43] J. Konigsberg,[11] K. Kordas,[23] A. Korn,[22] A. Korytov,[11] E. Kovacs,[2] J. Kroll,[31] M. Kruse,[35] S. E. Kuhlmann,[2] K. Kurino,[15] T. Kuwabara,[41] A. T. Laasanen,[34] N. Lai,[7] S. Lami,[36] S. Lammel,[10] J. I. Lamoureux,[4] M. Lancaster,[21] G. Latino,[32] T. LeCompte,[2] A. M. Lee IV,[9] K. Lee,[39] S. Leone,[32] J. D. Lewis,[10] M. Lindgren,[5] T. M. Liss,[16] J. B. Liu,[35] Y. C. Liu,[1] N. Lockyer,[31] J. Loken,[29] M. Loreti,[30] D. Lucchesi,[30] P. Lukens,[10] S. Lusin,[44] L. Lyons,[29] J. Lys,[21] R. Madrak,[14] K. Maeshima,[10] P. Maksimovic,[14] L. Malferrari,[3] M. Mangano,[32] M. Mariotti,[30] G. Martignon,[30] A. Martin,[45] J. A. J. Matthews,[26] J. Mayer,[23] P. Mazzanti,[3] K. S. McFarland,[35] P. McIntyre,[38] E. McKigney,[31] M. Menguzzato,[30] A. Menzione,[32] C. Mesropian,[36] A. Meyer,[7] T. Miao,[10] R. Miller,[25] J. S. Miller,[24] H. Minato,[41] S. Miscetti,[12] M. Mishina,[20] G. Mitselmakher,[11] N. Moggi,[3] E. Moore,[26] R. Moore,[24] Y. Morita,[20] M. Mulhearn,[22] A. Mukherjee,[10] T. Muller,[18] A. Munar,[32]

P. Murat,[10] S. Murgia,[25] M. Musy,[40] J. Nachtman,[5] S. Nahn,[45] H. Nakada,[41] T. Nakaya,[7] I. Nakano,[15] C. Nelson,[10] D. Neuberger,[18] C. Newman-Holmes,[10] C.-Y. P. Ngan,[22] P. Nicolaidi,[40] H. Niu,[4] L. Nodulman,[2] A. Nomerotski,[11] S. H. Oh,[9] T. Ohmoto,[15] T. Ohsugi,[15] R. Oishi,[41] T. Okusawa,[28] J. Olsen,[44] W. Orejudos,[21] C. Pagliarone,[32] F. Palmonari,[32] R. Paoletti,[32] V. Papadimitriou,[39] S. P. Pappas,[45] D. Partos,[4] J. Patrick,[10] G. Pauletta,[40] M. Paulini,[21] C. Paus,[22] L. Pescara,[30] T. J. Phillips,[9] G. Piacentino,[32] K. T. Pitts,[16] R. Plunkett,[10] A. Pompos,[34] L. Pondrom,[44] G. Pope,[33] M. Popovic,[23] F. Prokoshin,[8] J. Proudfoot,[2] F. Ptohos,[12] O. Pukhov,[8] G. Punzi,[32] K. Ragan,[23] A. Rakitine,[22] D. Reher,[21] A. Reichold,[29] W. Riegler,[14] A. Ribon,[30] F. Rimondi,[3] L. Ristori,[32] W. J. Robertson,[9] A. Robinson,[23] T. Rodrigo,[6] S. Rolli,[42] L. Rosenson,[22] R. Roser,[10] R. Rossin,[30] A. Safonov,[36] W. K. Sakumoto,[35] D. Saltzberg,[5] A. Sansoni,[12] L. Santi,[40] H. Sato,[41] P. Savard,[23] P. Schlabach,[10] E. E. Schmidt,[10] M. P. Schmidt,[45] M. Schmitt,[14] L. Scodellaro,[30] A. Scott,[5] A. Scribano,[32] S. Segler,[10] S. Seidel,[26] Y. Seiya,[41] A. Semenov,[8] F. Semeria,[3] T. Shah,[22] M. D. Shapiro,[21] P. F. Shepard,[33] T. Shibayama,[41] M. Shimojima,[41] M. Shochet,[7] J. Siegrist,[21] G. Signorelli,[32] A. Sill,[39] P. Sinervo,[23] P. Singh,[16] A. J. Slaughter,[45] K. Sliwa,[42] C. Smith,[17] F. D. Snider,[10] A. Solodsky,[36] J. Spalding,[10] T. Speer,[13] P. Sphicas,[22] F. Spinella,[32] M. Spiropulu,[14] L. Spiegel,[10] J. Steele,[44] A. Stefanini,[32] J. Strologas,[16] F. Strumia, [13] D. Stuart,[10] K. Sumorok,[22] T. Suzuki,[41] T. Takano,[28] R. Takashima,[15] K. Takikawa,[41] P. Tamburello,[9] M. Tanaka,[41] B. Tannenbaum,[5] W. Taylor,[23] M. Tecchio,[24] P. K. Teng,[1] K. Terashi,[36] S. Tether,[22] D. Theriot,[10] R. Thurman-Keup,[2] P. Tipton,[35] S. Tkaczyk,[10] K. Tollefson,[35] A. Tollestrup,[10] H. Toyoda,[28] W. Trischuk,[23] J. F. de Troconiz,[14] J. Tseng,[22] N. Turini,[32] F. Ukegawa,[41] T. Vaiciulis,[35] J. Valls,[37] S. Vejcik III,[10] G. Velev,[10] R. Vidal,[10] R. Vilar,[6] I. Volobouev,[21] D. Vucinic,[22] R. G. Wagner,[2] R. L. Wagner,[10] J. Wahl,[7] N. B. Wallace,[37] A. M. Walsh,[37] C. Wang,[9] C. H. Wang,[1] M. J. Wang,[1] T. Watanabe,[41] D. Waters,[29] T. Watts,[37] R. Webb,[38] H. Wenzel,[18] W. C. Wester III,[10] A. B. Wicklund,[2] E. Wicklund,[10] H. H. Williams,[31] P. Wilson,[10] B. L. Winer,[27] D. Winn,[24] S. Wolbers,[10] D. Wolinski,[24] J. Wolinski,[25] S. Wolinski,[24] S. Worm,[26] X. Wu,[13] J. Wyss,[32] A. Yagil,[10] W. Yao,[21] G. P. Yeh,[10] P. Yeh,[1] J. Yoh,[10] C. Yosef,[25] T. Yoshida,[28] I. Yu,[19] S. Yu,[31] Z. Yu,[45] A. Zanetti,[40] F. Zetti,[21] and

S. Zucchelli[3]

(CDF Collaboration)

[1] *Institute of Physics, Academia Sinica, Taipei, Taiwan 11529, Republic of China*

[2] *Argonne National Laboratory, Argonne, Illinois 60439*

[3] *Istituto Nazionale di Fisica Nucleare, University of Bologna, I-40127 Bologna, Italy*

[4] *Brandeis University, Waltham, Massachusetts 02254*

[5] *University of California at Los Angeles, Los Angeles, California 90024*

[6] *Instituto de Fisica de Cantabria, CSIC-University of Cantabria, 39005 Santander, Spain*

[7] *Enrico Fermi Institute, University of Chicago, Chicago, Illinois 60637*

[8] *Joint Institute for Nuclear Research, RU-141980 Dubna, Russia*

[9] *Duke University, Durham, North Carolina 27708*

[10] *Fermi National Accelerator Laboratory, Batavia, Illinois 60510*

[11] *University of Florida, Gainesville, Florida 32611*

[12] *Laboratori Nazionali di Frascati, Istituto Nazionale di Fisica Nucleare, I-00044 Frascati, Italy*

[13] *University of Geneva, CH-1211 Geneva 4, Switzerland*

[14] *Harvard University, Cambridge, Massachusetts 02138*

[15] *Hiroshima University, Higashi-Hiroshima 724, Japan*

[16] *University of Illinois, Urbana, Illinois 61801*

[17] *The Johns Hopkins University, Baltimore, Maryland 21218*

[18] *Institut für Experimentelle Kernphysik, Universität Karlsruhe, 76128 Karlsruhe, Germany*

[19] *Korean Hadron Collider Laboratory: Kyungpook National University, Taegu 702-701; Seoul National University, Seoul 151-742; and SungKyunKwan University, Suwon 440-746; Korea*

[20] *High Energy Accelerator Research Organization (KEK), Tsukuba, Ibaraki 305, Japan*

[21] *Ernest Orlando Lawrence Berkeley National Laboratory, Berkeley, California 94720*

[22] *Massachusetts Institute of Technology, Cambridge, Massachusetts 02139*

[23] *Institute of Particle Physics: McGill University, Montreal H3A 2T8; and University of Toronto, Toronto M5S 1A7; Canada*

[24] *University of Michigan, Ann Arbor, Michigan 48109*

[25] *Michigan State University, East Lansing, Michigan 48824*

[26] *University of New Mexico, Albuquerque, New Mexico 87131*

[27] *The Ohio State University, Columbus, Ohio 43210*

[28] *Osaka City University, Osaka 588, Japan*

[29] *University of Oxford, Oxford OX1 3RH, United Kingdom*

[30] *Universita di Padova, Istituto Nazionale di Fisica Nucleare, Sezione di Padova, I-35131 Padova, Italy*

[31] *University of Pennsylvania, Philadelphia, Pennsylvania 19104*

[32] *Istituto Nazionale di Fisica Nucleare, University and Scuola Normale Superiore of Pisa, I-56100 Pisa, Italy*

[33] *University of Pittsburgh, Pittsburgh, Pennsylvania 15260*

[34] *Purdue University, West Lafayette, Indiana 47907*

[35] *University of Rochester, Rochester, New York 14627*

[36] *Rockefeller University, New York, New York 10021*

[37] *Rutgers University, Piscataway, New Jersey 08855*

[38] *Texas A&M University, College Station, Texas 77843*

[39] *Texas Tech University, Lubbock, Texas 79409*

[40] *Istituto Nazionale di Fisica Nucleare, University of Trieste/ Udine, Italy*

[41] *University of Tsukuba, Tsukuba, Ibaraki 305, Japan*

[42] *Tufts University, Medford, Massachusetts 02155*

[43] *Waseda University, Tokyo 169, Japan*

[44] *University of Wisconsin, Madison, Wisconsin 53706*

[45] *Yale University, New Haven, Connecticut 06520*

Appendix B

The KS Test

In order to quantify the level of agreement observed between the Standard Model prediction and our smeared p_T distribution we have performed a KS test for compatibility between these two distributions. For our default background fraction, the measured KS probability is 0.050. In order to take into account the variation in this probability with the systematic uncertainties in the analysis, we have computed the KS probability for the observed distribution using predictions for the cases where one of our systematic effects has been shifted. The results are presented in Table B.1.

In order to quantify the sensitivity of our result to the systematic effects, we choose to compute the KS probability after varying each of the relevant systematic effects by one standard deviation. The results are presented in Table B.1. We interpret the result as follows: "Assuming our default Monte Carlo model to be correct, the probability to observe a difference between the two distributions as large as the one that is measured is calculated to be 5.0%. This probability varies between 1.0% and 9.4% when the background level and each of the systematic effects are varied by one standard deviation in our model."

Table B.1: The KS probability for the cases where one of our systematic effects has been shifted by one standard deviation in the Monte Carlo prediction. We take the range of variation as a measure of the sensitivity of this probability to systematic effects.

Systematic Effect	KS Probability
None	5.0%
Increase Background Normalization	2.4%
Decrease Background Normalization	9.4%
Increase Jet Energy Scale	7.3%
Decrease Jet Energy Scale	1.0%
No Initial State Radiation in $t\bar{t}$ Model	3.5%
$m_t = 170$ GeV/c^2	3.8%
$m_t = 180$ GeV/c^2	6.3%
$Q^2 = M_W^2$ in VECBOS	3.7%

Bibliography

[1] W.C. Röntgen, Sitzber. Physik. Med. Ges. **137** 1 (1895).

[2] E. Rutherford, Phil. Mag. **21** 669 (1911).

[3] J. Chadwick, Nature **129** 312 (1932).

[4] S.H. Neddermeyer, C.D. Anderson, Phys. Rev. **51** 884 (1937).

[5] H. Yukawa, Proc. Phys.-Math. Soc. Jap. **17** 48 (1935).

[6] D.H. Perkins , Nature **159** 126(1947).

[7] M. Gell-Mann, Phys. Lett. **8** 214(1964); G. Zweig, CERN-8182-TH-401 (1964).

[8] V.E. Barnes *et al.*, Phys. Rev. Lett. **12** 204 (1964).

[9] R.W. McAllister, R. Hofstadter, Phys. Rev. **102** 851 (1956).

[10] M. Breidenbach *et al.*, Phys. Rev. Lett. **23** 935 (1969).

[11] M. L. Perl *et al.*, Phys. Rev. Lett. **35**, 1489 (1975).

[12] J. E. Augustin *et al.*, Phys. Rev. Lett. **33**, 1406 (1974); J. J. Aubert *et al.*, Phys. Rev. Lett. **33**, 1404 (1974).

[13] S. L. Glashow, J. Iliopoulos and L. Maiani, Phys. Rev. **D2**, 1285 (1970).

[14] G. Hanson *et al.*, Phys. Rev. Lett. **35**, 1609 (1975).

[15] S. W. Herb *et al.*, Phys. Rev. Lett. **39**, 252 (1977).

[16] F. Abe *et al.*, Phys. Rev. D**50**, 2966 (1994).

[17] F. Abe *et al.*, Phys. Rev. Lett. **74**, 2626 (1995); S. Abachi *et al.*, Phys. Rev. Lett **74**, 2632 (1995).

[18] S.L. Glashow, Nucl. Phys. **22**, 579 (1961); S. Weinberg, Phys. Rev. Lett. **19**, 1264 (1967); A. Salam, in *Elementary Particle Physics*, ed. N. Svartholm, p. 367 1968.

[19] P. W. Higgs, Phys. Rev. **145**, 1156 (1966); P. W. Higgs, Phys. Rev. Lett. **13**, 508 (1964).

[20] R.S. Chivukula, *Dynamical Electroweak Symmetry Breaking and the Top Quark*, talk presented at SLAC Topical Workshop, Stanford, 19-21 July 1995.

[21] G. Abbiendi *et al.*, Eur. Phys. J. **C12**, 567 (2000).

[22] H. Georgi and S.L. Glashow, Phys. Rev. Lett. **32**, 438 (1974).

[23] L. Susskind, Phys. Rev. D **20**, 2619 (1979).

[24] S. Weinberg, Phys. Rev. D **13**, 974 (1976); S. Weinberg, Phys. Rev. D **19**, 1277 (1979).

[25] B. Holdom, *Raising the Sideways Scale*, Phys. Rev. D **24**, 1441 (1981); B. Holdom, *Techniodor*, Phys. Lett. **B150**, 301 (1985).

[26] J.D. Bjorken, Proc. Summer Institute on Particle Physics, SLAC Report 198 (1976); J. Ellis, M.K. Gaillard and D.V. Nanopoulos, Nucl. Phys. **B106** 292 (1976).

[27] R.K. Ellis, W.J. Stirling and B.R. Webber, *QCD and Collider Physics*, Cambridge University Press, Cambridge: 1996.

[28] N. Kidonakis and J. Smith, Phys. Rev. **D51**, 6092 (1995).

[29] C.T. Hill, Phys. Lett. **B345**, 483 (1995).

[30] K. Lane, Phys. Rev. D **52**, 1546 (1995).

[31] C.T. Hill and S. Parke, Phys. Rev. D **49**, 4454 (1994).

[32] T.G. Rizzo, hep-ph/9902273; E. Simmons hep-ph/hep-ph/9908511.

[33] K. Lane, *Introduction to Technicolor*, in The Building Blocks of Creation (TASI-93), S. Raby and T. Walker. eds. (World Scientific, Singapore, 1994).

[34] K. Cheung and R.M. Harris, *Discovering New Interactions at Colliders*, in the proceedings of 1996 DPF DPB Summer Study on New Directions for High-energy Physics (Snowmass 96), Snowmass, CO, 25 Jun - 12 Jul 1996.

[35] B. Holdom, Phys. Lett. **B353**, 295 (1995).

[36] B. Abbott *et al.*, Phys. Rev. **D58**, 052001 (1998).

[37] T. Affolder *et al.*, hep-ex/0006028.

[38] G. Carron *et al.*, Phys. Lett **77B**, 353 (1978).

[39] A.G. Ruggiero, IEEE Trans. Nucl. Sci. **30**, 2478 (1983).

[40] Particle Data Group, Eur. Phys. J. C **3**, 1 (1998).

[41] F. Abe *et al.*, Nucl. Instrum. Methods Phys. Res., Sect. A **271**, 387 (1988); D. Amidei *et al.*, Nucl. Instrum. Methods Phys. Res., Sect A**350**,73 (1994).

[42] F. Abe *et al.*, Phys. Rev. Lett. **80**, 2063 (1998).

[43] K.A. Tollefson, Ph.D. Thesis, University of Rochester (1997).

[44] F. Abe *et al.*, Phys. Rev. Lett. **80**, 2779 (1998).

[45] A.D. Martin, R.G. Roberts, and W.J. Stirling, Phys. Lett. B **308**, 145 (1993).

[46] F. Abe *et al.*, Phys. Rev. Lett. **74**, 850 (1995).

[47] G. Marchesini and B.R. Webber, Nucl. Phys. B **310**, 461 (1998); G. Marchesini *et al.*, Comput. Phys. Commun. **67**, 465 (1992). We use HERWIG version 5.6.

[48] T. Sjöstrand, Comput. Phys. Commun. **82**, 74 (1994).

[49] F. Abe *et al.*, Phys. Rev. Lett., **75**, 608(1995).

[50] P. Avery, K. Read, G. Trahern, Cornell Internal Note CSN-212 (1985).

[51] F.A. Berends, W.T. Giele, H. Kujif and B. Tausk, Nucl. Phys. B **357**, 32 (1991).

[52] F. Abe *et al.*, Phys. Rev. Lett., **79**, 4760 (1997).

[53] F. Abe *et al.*, Phys. Rev. D **51**, 4623 (1995).

[54] F. Abe *et al.*, Phys. Rev. Lett., **80**, 2773 (1998).

[55] J. Ohnemus and J. F. Owens, Phys. Rev. D **43**, 3626 (1991).

[56] T. Stelzer, Z. Sullivan and S. Willenbrock, Phys. Rev. D **58**, 3626 (1998); T. Stelzer, Z. Sullivan and S. Willenbrock, Phys. Rev. D **56**, 5919 (1997); T. Stelzer, S. Willenbrock, Phys. Rev. D **54**, 6696 (1996); T. Stelzer, S. Willenbrock, Phys. Rev. B **357**, 125 (1995).

[57] F. Abe *et al.*, Phys. Rev. Lett. **80**, 2767 (1998).

[58] F. Abe *et al.*, Phys. Rev. D **47**, 4857 (1993).

[59] T. Affolder et al., FERMILAB-PUB-00/051-E.

[60] F. James and M. Roos, Comput. Phys. Commun. **10**, 343 (1975).

[61] W.T. Eadie *et al.*, *Statistical Methods in Experimental Physics*, North-Hollad, Amsterdam: 1971.